TÉCNICO LISBOA

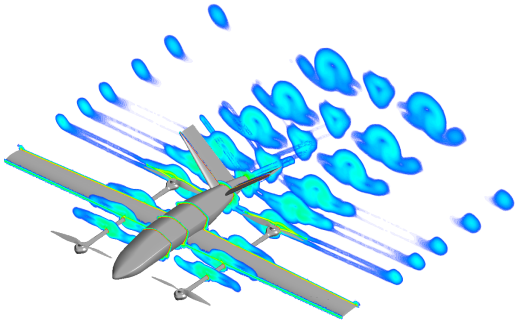

Aerodynamic interference between rotors, fuselage, wing and control surfaces of a VTOL UAV

António e Silva Figueiredo dos Reis

Thesis to obtain the Master of Science Degree in

Aerospace Engineering

Supervisors: Prof. Filipe Szolnoky Ramos Pinto Cunha
Dr. Dário Filipe Romana Pedro

Examination Committee

Chairperson: Prof. Paulo Jorge Coelho Ramalho Oliveira
Supervisor: Prof. Filipe Szolnoky Ramos Pinto Cunha
Member of the Committee: Prof. José Maria Campos da Silva André

July 2022

I declare that this document is an original work of my own authorship and that it fulfills all the requirements of the Code of Conduct and Good Practices of the Universidade de Lisboa.

Acknowledgments

First, I would like to express my gratitude to Professor Filipe Cunha for the patience, guidance and support shown on such a regular basis throughout this whole process.

I would also like to thank Dr. Dário Pedro and Beyond Vision for allowing me to conduct my Master's Thesis in an industrial environment, in such an interesting project, and for providing me with all the means and support needed to conclude this milestone.

To my family, no appreciation can be enough, as you have provided me with the example and all the tools required for me to achieve where I am.

To my friends, with whom I have grown with, thank you for all the good times together, for the stories, and for all the knowledge I have gotten from you. For those which I have made throughout the last five years, and shared multiple endeavours with, but shared even more accomplishments, in the end the memories remain and the friendship lives on.

Finally, I would like to give a special thanks to Marta for all the help during the stressful moments that always emerge in endeavours like this.

Resumo

Esta tese pretende estudar a interferência aerodinâmica entre componentes de um Veículo Aéreo Não Tripulado (VANT) capaz de descolar e aterrar verticalmente (VTOL), desenvolvido pela Beyond Vision, aferindo os modelos adequados para simular o comportamento, nas diferentes fases de voo, utilizando CFD. Efetuaram-se simulações recorrendo a análise de Reynolds Averaged Navier-Stokes, utilizando o modelo de turbulência $k-\omega$ SST, a Mach cruzeiro de $M = 0.088$, e de ponta dos rotores de $M_{tip} = 0.32$, a Reynolds de cruzeiro $Re \approx 3 \times 10^5$. Para modelar os rotores consideraram-se os modelos Multiple Reference Frame, Sliding Mesh e Overset Mesh. Realizou-se um estudo de independência de malha no rotor, verificando e validando os resultados com dados de desempenho do fornecedor e dados experimentais de Miluzzo (2020). Concluiu-se que o MRF seria o método apropriado devido ao custo computacional e exatidão dos. Em cruzeiro verificou-se que as estruturas VTOL, tendo os rotores alinhados com o escoamento, aumentam significativamente a resistência aerodinâmica do VANT, reduzinddo C_L/C_D de 10.45 para 7.28, e diminuindo os coeficientes aerodinâmicos da asa. Observou-se que a posição dos rotores na asa não tem um efeito palpável no desempenho, mas a orientação do rotor relativamente ao escoamento sim, tendo o rotor perpendicular reduzido C_L/C_D para 6.82. Em voo vertical verificou-se que os rotores e a estrutura do VANT se afetam mutuamente, e que ter os rotores afastados da fuselagem reduz a interação do rotor traseiro com a cauda. Em voo de transição concluiu-se que o MRF não se adequa para este tipo de escoamento, fazendo-se apenas uma análise qualitativa.

Palavras-chave: Veículo Aéreo Não Tripulado (VANT), Mecânica dos Fluidos Computacional (MFC), Vertical Take-Off and Landing (VTOL), Interferência Aerodinâmica

Abstract

This thesis aims at studying aerodynamic interference between the components of a Vertical Take-Off and Landing (VTOL) Unmanned Aerial Vehicle, developed by Beyond Vision, while assessing the adequate models to simulate flow behaviour during different flight stages, using CFD. Simulations were performed resorting to Reynolds Averaged Navier-Stokes analyses, employing $K-\omega$ SST turbulence model, at a cruise Mach $M = 0.088$, and rotor tip Mach $M_{tip} = 0.32$, and cruise Reynolds of $Re \approx 3\times10^5$. To model rotors, the Multiple Reference Frame (MRF), Sliding Mesh and Overset Mesh models were considered. A Mesh independence study was performed on the rotor, verifying and validating the results with data provided by the manufacturer and experimental data from Miluzzo (2020). MRF was deemed the most suitable model according to computational cost and accuracy of results. During cruise, it was verified that the VTOL structures, with blades parallel with the flow, significantly increases drag, decreasing C_L/C_D from 10.45 to 7.28, while worsening the wing's aerodynamic coefficients. It was observed that the rotor position across the wing had negligible impact on performance, but its orientation relative to the flow does, having C_L/C_D reduced to 6.82 when rotors are perpendicular to the flow. In vertical flight it was observed that the rotors and airframe interacted mutually, losing performance, and that having the rotors far from the fuselage reduces rear rotor interference with the tail. In transition flight it was concluded that the MRF method was not suitable for that application, performing only a qualitative analysis of the flow.

Keywords: Unmanned Aerial Vehicle (UAV), Computational Fluid Dynamics (CFD), Vertical Take-Off and Landing (VTOL), Aerodynamic Interference

Contents

List of Tables

List of Figures

Nomenclature

Greek symbols

β,$*\beta$,γ,ν,ω_k,ω_w,ω_{w2} $k-\omega$ Shear Stress Transport model constants.

$\boldsymbol{\omega}$ Angular velocity vector, $rad\ s^{-1}$.

$\overline{\boldsymbol{\tau}}$ Stress tensor, $N\ m^{-2}$.

χ Spalart-Allmaras's intermediate variable.

Δt Temporal discretization, s.

Δx Spatial discretization, m.

η, η_1, η_2 $K-\omega$-SST generic constant.

Γ Diffusion coefficient.

κ Von Kárman constant.

μ Dynamic viscosity, $N\ m^{-1}\ s^{-1}$.

μ_t Dynamic turbulent viscosity, $N\ m^{-1}\ s^{-1}$.

ν_t Kinematic turbulent viscosity, $m^2\ s^{-1}$.

Ω Spalart-Allmaras Turbulence model mean vorticity, $rad\ s^{-1}$.

ω Turbulence frequency, s^{-1}.

Ω_R Rotor angular velocity, $rad\ s^{-1}$.

ω_x,ω_y,ω_z Angular velocity components in cartesian coordinates, $rad\ s^{-1}$.

$\overline{\nu}$ Kinematic eddy-viscosity, $m^2\ s^{-1}$.

∂V Control volume boundary, m^{-2}.

ϕ Generic variable.

Ψ Azimutal angle, $^\circ$.

ρ Density, $Kg\ m^{-3}$.

σ_ν Turbulent Prandtl number.

τ^R Reynolds stress tensor, $N\ m^{-2}$.

τ_w Wall shear stress, $N\ m^{-2}$.

ε Turbulent kinetic energy dissipation rate per mass unit, $m^2\ s^{-3}$.

Roman symbols

$\mathbf{A}$ Infinitesimal area vector, m^2.

A Area of the rotor disk, m^2.

a Speed of sound, $m\ s^{-1}$.

b Wingspan, m.

$\frac{C_L}{C_D}$ Lift-to-drag ratio.

$\overline{c}$ Mean aerodynamic chord, m.

C Courant number.

C_b1,C_b2,C_w1,$C_{\nu 1}$ Spalart-Almaras Turbulence model constants.

C_D Three dimensional drag coefficient.

C_d Two dimensional drag coefficient.

C_f Friction coefficient.

C_L Three dimensional lift coefficient.

C_l Two dimensional lift coefficient.

C_p Pressure coefficient.

C_T Thrust coefficient.

C_{PW} Power coefficient.

D Characteristic length, m.

e Total energy per unit mass, J/kg.

$\mathbf{F}$ External body forces, N.

F Download Force.

F_1 $k-\omega$ Shear Stress Transport model blending function.

$f_{\nu 1}$,$f_{\nu 2}$,f_w Spalart-Almaras Turbulence model functions.

g Gravitational acceleration, $m\ s^{-2}$.

h_0 First layer thickness, m.

I Identity matrix.

k Turbulent kinetic energy per unit mass, $m^2\ s^{-2}$.

L Approximate lenght of the computational domain, m.

M Mach number.

n Prism layer number.

P Power, W.

p Static pressure, $N\ m^{-2}$.

$\dot{q_s}$ Rate of heat transfer per unit area, $J\ m^{-2}\ s^{-1}$.

$\mathbf{r}$ Position vector.

R Rotor radius, m.

r Distance to rotor axis, m.

r_0 Position vector of the moving reference frame origin.

r_g Prism layer growth rate.

Re Reynolds number.

S Wing planform area, m^2.

S_h Energy source term in energy conservation equation, $J\ Kg\ m^{-3}\ s^{-1}$.

S_m Mass source term in mass conservation equation, $Kg\ m^{-3}\ s^{-1}$.

S_ϕ Generic quantity source term.

$\frac{T}{W}$ Thrust factor.

T Thrust, N.

t Time, s.

$\mathbf{U}$ Velocity vector, $m\ s^{-1}$.

$\mathbf{U_g}$ Velocity of the moving mesh element, $m\ s^{-1}$.

$\mathbf{U_r}$ Fluid velocity relative to moving reference frame, $m\ s^{-1}$.

u, v, w Velocity components in cartesian coordinates, $m\ s^{-1}$.

u_t Friction velocity, $m\ s^{-1}$.

$\mathbf{V_r}$ Reference frame velocity vector, $m\ s^{-1}$.

$\mathbf{V_t}$ Linear velocity vector of the moving reference frame, $m\ s^{-1}$.

V Volume. m^3.

W Weight, Kg.

y Wall distance, m.

y^+ Dimensionless wall distance.

Subscripts

∞ Relative to the free-stream condition.

c Relative to cruise conditions.

f, w, t Relative to the fuselage, wing and tail, respectively.

i, j Computational indexes.

L Relative to a characteristic length.

tip Relative to the rotor blade or wing tip.

x, y, z Relative to the cartesian components.

Superscripts

' Fluctuating component.

$\bar{}$ Mean value component.

T Transpose.

Glossary

BEMT	Blade Element Momentum Theory
CAD	Computer-Aided Design
CAE	Computer Aided Engineering
CFD	Computational Fluid Dynamics
CFL	Courant-Friedrichs-Lewy
DNS	Direct Numerical Simulation
FEA	Finite Element Analysis
FEA	Out of Ground Effect
FVM	Finite Volume Method
IGE	In Ground Effect
LES	Large Eddy Simulation
LE	Leading Edge
MRF	Multiple Reference Frame
MTOW	Maximum Take-Off Weight
RANS	Reynolds-Averaged Navier-Stokes
SLT	Separate Lift and Thrust
TE	Trailing Edge
UAV	Unmanned Aerial Vehicle
VTOL	Vertical Take-Off Landing

Chapter 1

Introduction

1.1 Motivation

The use of Unmanned Aerial Vehicles (UAV) has been increasing, ranging all the way from military applications, such as surveillance and reconnaissance, to commercial uses, like agricultural monitoring, air cargo transportation, or cinematography. Recently, different UAV's capable of Vertical Take-Off and Landing (VTOL), while keeping the conventional fixed-wing, horizontal, flight have been sprouting in the market, as they combine the VTOL and manoeuvrability capabilities of rotorcraft, with the long range and efficiency of conventional fixed-wing aircraft.

Although the aerodynamics of conventional aircraft and rotorcraft have been separately studied, no analytic methods exist to evaluate the interaction between the structures correspondent to the different flight types, thus this area must be studied through wind tunnel test data or computer simulations, known as Computational Fluid Dynamics (CFD), for each specific aircraft configuration.

Wind tunnel testing is an expensive, time consuming, process, since new prototypes need to be built or modified whenever a new change is made to the design. Fortunately, the increase in computational power over the last decades and the availability of powerful, off-the-shelf, commercial CFD software, have rendered computer simulations as a fast and cheap way for companies to employ in the iterative design process of VTOL UAV's, specifically at understanding the aerodynamic interactions between the different aircraft components at vertical and horizontal flight, and while transitioning between both.

1.2 State of the Art

As stated in section 1.1, due to their high versatility, VTOL aircraft have been studied ever since the first helicopters were developed. During the 1950's and 1960's some of the first VTOL fixed-wing aircraft prototypes were developed, namely the Lockheed XFV and the Convair XFY Pogo.

In the next decades, more, and more sophisticated tests were performed, as are the examples of Heyson in [1], Felker and J. Light in [2] and McVeigh in [3], which coincide with the time of development of the Bell Boeing V-22, considered to be the first production tilt-rotor aircraft.

In the 1990's CFD calculations started being employed to study VTOL aircraft. Examples of those studies are those of I. Fetjec and L. Roberts (1992) [4] and M. Smith et al. (1994) [5]. At this point, some commercial applications to VTOL aircraft had been studied but were dismissed as the costs proved to be too prohibitive.

Fast forward to the last decade, and the advent of UAVs, reflecting the investment on new technological solutions to everyday tasks, and the search for new electrical solutions for Urban Air Mobility (UAM) in big cities with extreme traffic problems, have re-sparked the interest in VTOL technology. To solve the problem at hand different approaches have been pursued.

Jung in [6] performed a numerical study on Smart-UAV, targeted at UAM, and developed by the Korea Aerospace Research Institute to assess the aerodynamic interference between the rotor wake and the vertical stabilizer in hover flight, and at low forward velocities, as well as its impact in directional stability. An overset mesh technique was adopted to simulate the relative motion between the rotor and the fuselage.

Zhang in [7] simulated the transition flow fields between hover to cruise flight of the V-22 Osprey tilt-rotor aircraft. The study combined the use of an overset mesh technique around the rotor nacelle, coupled with actuator disk modelling on the propellers.

Droandi in [8] ran wind tunnel experiments on a half-span scale model of a partial tilt-wing, that is, a fixed wing with a tilting section at the tip, which rotates together with the rotor nacelle. The study aimed at describing the effects of the interference between the prop-rotor and the wing at the first stages of conversion between hover and cruise flight. Tests were done for both the isolated rotor and the half-span model.

Ye in [9] performed new numerical studies in hover flight on the V-22 Osprey to obtain the aerodynamic interference between the rotor, wing, and fuselage. This time a multi-layered overset mesh and extended-hole fringe was used to tackle the difficulties in grid assembly, and to reduce interpolation errors. The wing aerodynamic loads were obtained for different rotor collective angles, with and without nacelle and a qualitative analysis was made to the flow streamlines on different planes.

D. Adair and M. Alimaganbetov in [10] presented during the 56th Israel Annual Conference on Aerospace Sciences a numerical study on a partial tilt-wing configuration where the tilting section is located outside the wing tip. The rotors were modelled using the Blade Element Momentum Theory (BEMT). A parametric study was performed in order to obtain the optimum width of the deflecting section in hover flight. Transition flight and cruise/manoeuvres were also analysed.

Chen in [11] tested a scale model of a quad tilt-rotor aircraft on a wind tunnel to evaluate the aerodynamic interference which occurs near ground-effect while hovering, as well as during transition flight at low velocities. The aerodynamic loads on the aircraft were measured and the flow field below the airframe was captured with particle image velocimetry. While hovering, near ground effect caused an upload on the airframe. In transition flight, as the velocity increased, the total upload decreased and eventually became a download.

Huang in [12] studied the transition flight on a tilt-rotor UAV composed of five tilt-rotors. A multi zone mesh was used with a Multiple Reference Frame method to establish the interaction between the rotors

and the fixed background grid.

There is currently a multitude of different well studied solutions for VTOL flight, each one with its advantages and disadvantages. Some configurations are more adequate for specific applications, like the vectored thrust made by varying the direction of the engine exhaust, which is appropriate for fighter jets but isn't applicable to smaller electrical UAV's.

The most common configurations for UAM and, specifically, for UAVs, are:

- The tilt-rotor, in which the rotors tilt in order to produce thrust in vertical or horizontal flight;
- The tilt-wing, which is similar to the the tilt-rotor, but the wing, or a section of it, tilts together with the rotor;
- The Separate Lift and Thrust (SLT) in which vertical and horizontal flight are governed by two different powertrains.

Other possible configurations are tail-sitters or multicopters. Tail-sitters, as the name indicates, land vertically on their tail, having one fixed thrust source responsible for VTOL and horizontal flight. This configuration has the disadvantage of the vertical position of the aircraft during hover and vertical climb, thus not being suitable for some missions, and the transition between the two different flight modes is more complex than in other types. Multicopters have large rotor disk areas, being highly efficient in hover and vertical flight, but lack the capability to perform long range missions.

From these configurations, tilt-rotors and tilt-wings have the best performance in long range missions, multicopters have the best performance in vertical flight, as stated, and STL UAVs prove to be a good compromise between both, according to Bacchini in [13].

1.3 Objectives and Deliverables

The final goal of this thesis is to obtain a deep understanding of the aerodynamic interaction between rotors, fuselage, wing and control surfaces of the beVTOne UAV, whilst assessing what are the best techniques to evaluate this interaction and its impact on the UAV's performance. To do so, CFD calculations are performed utilizing the Computer Aided Engineering (CAE) software package ANSYS. To achieve this goal, one can define further sub objectives:

1. Identify the currently available methods to simulate rotors in CFD and select the most suitable ones;
2. Prepare the geometries to be used in each flight phase, followed by generating appropriate meshes for them;
3. Implement the numerical models with respect to the governing constraints and boundary conditions in each specific study;
4. Verify if the solutions obtained from the implemented models are of physical significance and are independent of the spatial discretization;

5. Evaluate the different models and assess their suitability to be used during the design phase of new UAVs;

6. Process the results yielded by CFD calculations and evaluate the flow characteristics and UAV performance.

1.4 Thesis Outline

Beside the introducing chapter, this thesis is divided into six chapters, which are organized as follows:

Chapter 2: Theoretical Background

In this chapter the background knowledge necessary for the reader to follow the work done in this thesis is presented. Here, the numerical models utilized throughout the thesis are described.

Chapter 3: Application, Verification and Validation of the Chosen Methods

In the third chapter, the whole simulation process is described. The pre-processing starts with preparing the appropriate geometries for the intended study. Then the mesh generation procedure is explained and the utilized mesh parameters are showed. Following that, the numerical models described in chapter 2 are implemented, variables of interest are identified, and the appropriate simulation constraints and boundary conditions are selected.

Additionally, the methods chosen for the different simulations are verified and validated with available data.

Chapter 4: Aerodynamic Analyses

Next, the fourth chapter includes detailed description of every simulation performed in horizontal, vertical and transition flights, followed by an examination of the flow structures and the aerodynamic coefficients. The results are compared with one another and the aerodynamic interaction between the different UAV components is evaluated.

Chapter 5: Conclusions

In this last chapter, an assessment is made to the goals achieved in this thesis, in comparison with the original objectives that were set out to be accomplished. Some conclusions are drawn about the choice of numerical models to simulate rotor movement and including its advantages and disadvantages. Finally, some suggestions are left for future work, as to obtain a deeper understanding of the chosen configuration aerodynamics.

Chapter 2

Project Background

2.1 beVTOne Overview

This work focuses on the study of the beVTOne VTOL UAV developed by Beyond Vision, shown in figure 2.1. The beVTOne is an electric, multi purpose, UAV, specifically designed for commercial uses such has agriculture, powerline inspection or any other advanced monitoring application. Furthermore, it is dimensioned according to NATO requirements, meaning that it can also be employed in military applications.

Its layout consists of a traditional quad configuration for VTOL flight and a pusher at the rear for cruise flight, commonly known as a Separate Lift and Thrust configuration (SLT).

Figure 2.1: beVTOne VTOL UAV.

A typical flight mission profile is displayed in figure 2.2, being composed by vertical take-off and climb up to a height of $60m$, followed by transition to conventional flight and a further climb up to the cruise height of $120m$. Then, cruise flight follows, when the UAV is performing its assigned mission. Finally, the UAV transitions once again to vertical flight, descending axially and landing.

With a Maximum Take-Off Weight (MTOW) of $10kg$, its payload can consist of cameras and other sensors or cargo of up to $2kg$. The technical specifications are presented in table 2.1.

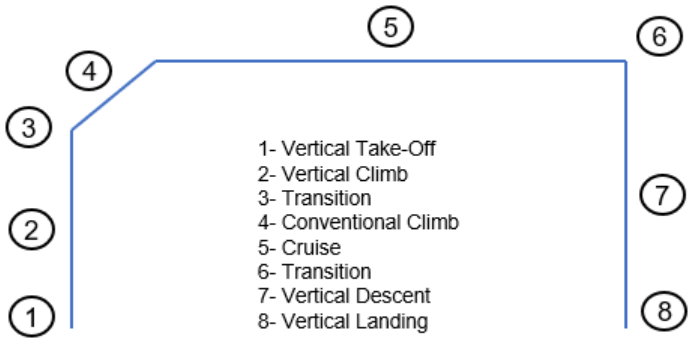

Figure 2.2: Typical mission profile.

Table 2.1: beVTOne technical specifications

Characteristics:	Value:
Height	500 mm
Length	1200 mm
Wingspan (b)	2560 mm
Mean Chord ($\bar{c}$)	150 mm
Wing Area (S)	0.384 m^2
Flight Height	120 m
Cruise Speed	30 m/s
Cruise Range	240 km

2.2 Governing Equations

In order to simulate fluid flow, ANSYS Fluent [14] utilizes the Finite Volume Method (FVM) to solve the conservation of mass (2.1), momentum (2.2) and energy (2.4) equations, this last one used when compressibility effects are not negligible. These are commonly called the Navier-Stokes equations [15]. The FVM discretizes the spatial domain into separate elements, which together constitute a mesh, and solves discretized forms of the equations presented in this chapter for each individual element. The mass conservation equation is given by

$$\frac{\partial \rho}{\partial t} + \nabla \cdot (\rho \mathbf{U}) = S_m, \tag{2.1}$$

where t is the time variable, ρ represents the fluid's density, $\mathbf{U} = (u, v, w)$ is the velocity vector and S_m is the mass source term, which in this work will be zero since no mass sources are present in the domain.

The momentum conservation equation by

$$\frac{\partial}{\partial t}(\rho \mathbf{U}) + \nabla \cdot (\rho \mathbf{U}\mathbf{U}) = -\nabla p + \nabla \cdot (\bar{\bar{\tau}}) + \rho \mathbf{g} + \mathbf{F}, \tag{2.2}$$

where p is the static pressure, $\bar{\bar{\tau}}$ is the stress tensor, given by

$$\bar{\bar{\tau}} = \mu \left[(\nabla \mathbf{U} + \nabla \mathbf{U}^T) - \frac{2}{3} \nabla \cdot \mathbf{U} I \right], \tag{2.3}$$

with μ being the dynamic viscosity and I the identity matrix, $\rho \mathbf{g}$ is the gravitational body force and

$\mathbf{F}$ represents the external body forces. This last term also includes model specific source terms and artificial, user-defined, sources.

Finally, the energy conservation equation is

$$\frac{\partial}{\partial t}(\rho e) + \nabla \cdot (\rho \mathbf{U} e) = -\nabla \cdot \dot{\mathbf{q}}_s - \nabla \cdot (p\mathbf{U}) + \nabla \cdot (\bar{\boldsymbol{\tau}} \cdot \mathbf{U}) + \mathbf{F} \cdot \mathbf{U} + S_h. \tag{2.4}$$

In this equation, e is the total energy per unit mass, $\dot{\mathbf{q}}_s$ is the rate of heat transfer per unit area across the surface area of the material element and S_h represents the rate of heat source or sink within the material volume per unit volume [16].

While enunciating the Navier-Stokes equations, no mention was made to whether the flow was laminar or turbulent. Said equations hold true for either case, but whereas laminar flow is stable, turbulent flow is chaotic, involving time-dependent, three-dimensional, vorticity fluctuations.[16] Turbulence develops from growing perturbations of the laminar flow which become unstable at a critical Reynolds[1] number (Re). Due to this, in order to accurately model turbulent flow and capture its characteristics, a very small spatial discretization, capable of capturing the smallest eddies is necessary, with a suitably small time discretization to satisfy the Courant–Friedrichs–Lewy (CFL) condition [17]. This process is called Direct Numerical Simulation (DNS) but it requires a high number of elements (proportional to Re^3), which translates to unfeasibly demanding computational power requirements, apart from a limited number of simple studies.

An alternative to DNS is Large Eddy Simulation (LES) which employs statistical averaging techniques to approximate random fluctuations. With this approach, only large scale eddies are directly simulated, whilst small scale eddies are modelled using sub-grid models and a spatial statistical filter is applied in order to determine which scales are to be kept.[16]

Despite LES presenting itself as a better alternative to DNS, it is still computationally demanding. It is becoming more widely accepted to solve industrial problems and its usage is increasing, as computers also become more powerful, but the most popular approach in the industry to solve turbulent flows is based on solving the Reynolds-Averaged Navier-Stokes (RANS) equations.

RANS' key approach is to decompose the flow variables, represented by ϕ, in a given position, $\mathbf{r} = (x, y, z)$, and instant, t, into a mean value component, $\bar{\phi}$, and a fluctuating one, ϕ', substituting it into the original equations, and then time-averaging said equations, as shown below. To proceed with averaging the equations, two routes can be taken, depending on the nature of the flow. For steady flows, time-averaging is used, as shown is (2.5), whereas for transient, time-dependant, flows, ensemble-averaging must be used [16].

$$\phi(\mathbf{r}, t) = \bar{\phi}(\mathbf{r}, t) + \phi'(\mathbf{r}, t) \tag{2.5}$$

After applying the aforementioned procedure, the Reynolds averaged form of equations (2.1) and (2.2), for incompressible, Newtonian flow are given by

[1] $Re = \frac{\rho U D}{\mu}$, where ρ is the fluid density, μ its dynamic viscosity, and U and D are the flow's characteristic velocity and length, respectively.

$$\nabla \cdot \left(\rho \bar{\mathbf{U}}\right) = 0 \tag{2.6}$$

and

$$\frac{\partial}{\partial t}\left(\rho \bar{\mathbf{U}}\right) + \nabla \cdot \left(\rho \overline{\mathbf{U}\mathbf{U}}\right) = -\nabla \bar{p} + \left[\nabla \cdot \left(\bar{\bar{\boldsymbol{\tau}}} - \rho \overline{\mathbf{U}'\mathbf{U}'}\right)\right] + \rho \bar{\mathbf{g}} + \bar{\mathbf{F}}. \tag{2.7}$$

All the variables represent the mean values of the previously described quantities, with the exception of a new appearing term, $-\rho\overline{\mathbf{U}'\mathbf{U}'}$, known as the Reynolds stress tensor, $\boldsymbol{\tau}^R$, shown as

$$\boldsymbol{\tau}^R = -\rho \begin{pmatrix} \overline{u'u'} & \overline{u'v'} & \overline{u'w'} \\ \overline{u'v'} & \overline{v'v'} & \overline{v'w'} \\ \overline{u'w'} & \overline{v'w'} & \overline{w'w'} \end{pmatrix}. \tag{2.8}$$

This term brings with itself six new unknowns, meaning that new equations are required to solve for the Reynolds stress components and to close the set of equations. These are called turbulence models and two widely used models in aerospace industry are to be described next.

2.2.1 Turbulence Models

$k-\omega$ Shear Stress Transport (SST) Turbulence Model

The $k-\omega$ model, developed by Wilcox in [18], closes the RANS system of equations resorting to two transport equations, one solving for the turbulent kinetic energy, k, and other for the turbulence frequency, ω. It shows a good modelling of the turbulence effects but its results present a dependency on the assumed values for k and ω at the free stream, which is a problem in external aerodynamics where free stream boundary conditions are generally used.

On the other hand, in [19], Menter noted that results of the $k-\varepsilon$[20] model, a two-equation model, also solving for k, and the rate of dissipation of turbulent kinetic energy, ε, are less sensitive to the user-assumed values in the free stream, while yielding poor near-wall performance in boundary layers with adverse pressure gradients.

Menter thus suggested a two-equation model, defined by equations (2.9a) and (2.9b), where the $k-\varepsilon$ model is used in the fully turbulent region far from the walls and is then transformed into the $k-\omega$ model in the near-wall regions. The Reynolds stress computation and the k-equation are the same as in Wilcox's original model, but the ε-equation is changed into ω by substituting $\varepsilon = k\omega$.

$$\frac{D\rho k}{Dt} = \tau_{ij}\frac{\partial u_i}{\partial x_j} - \beta^*\rho\omega k + \frac{\partial}{\partial x_j}\left[\left(\mu + \sigma_k \mu_t\right)\frac{\partial k}{\partial x_j}\right] \tag{2.9a}$$

$$\frac{D\rho\omega}{Dt} = \frac{\gamma}{\nu_t}\tau_{ij}\frac{\partial u_i}{\partial x_j} - \beta\rho\omega^2 + \frac{\partial}{\partial x_j}\left[\left(\mu + \sigma_\omega \mu_t\right)\frac{\partial \omega}{\partial x_j}\right] + 2\left(1 - F_1\right)\rho\sigma_{\omega 2}\frac{1}{\omega}\frac{\partial k}{\partial x_j}\frac{\partial \omega}{\partial x_j} \tag{2.9b}$$

Here, μ_t and ν_t are the dynamic and kinematic turbulent viscosities, respectively, β, β^*, γ, ν, σ_k, σ_ω and $\sigma_{\omega 2}$ are model constants calculated from (2.10), and F_1 is a blending function that ranges from zero

away from the walls, where the $k-\varepsilon$ equations dominate, to one, in the viscous sub-layer, where the $k-\omega$ equations dominate.

$$\eta = F_1\eta_1 + (1-F_1)\eta_2 \tag{2.10}$$

The generic constant, η, is calculated from two sets of constants, where the first set, η_1 corresponds to the SST inner constants, and the second set, η_2 corresponds to the standard $k-\varepsilon$ constants [19].

Overall, the model has a wide range of applicability in external aerodynamics studies, has been widely tested and verified, either in aerospace or other industrial applications. It has shown accurate results at modelling the flow in null and adverse pressure gradients, highly important while studying airfoils, and has proven to be a very stable model in complex applications [21].

Spalart-Allmaras Turbulence Model

The Spalart-Allmaras [22] model introduces one transport equation to model the kinematic eddy viscosity, $\tilde{\nu}$, as shown on (2.11).

$$\frac{\partial}{\partial t}(\rho\tilde{\nu}) + \nabla\cdot(\rho\tilde{\nu}\mathbf{U}) = \frac{1}{\sigma_\nu}\left[\nabla\cdot\left((\mu+\rho\tilde{\nu})\nabla\tilde{\nu}\right) + C_{b2}\rho(\nabla\tilde{\nu})^2\right] + C_{b1}\rho\tilde{\nu}\tilde{\Omega} - C_{w1}\rho\left(\frac{\tilde{\nu}}{\kappa y}\right)^2 f_w \tag{2.11}$$

The turbulent viscosity, μ_t, is then computed from equation (2.12), where $f_{\nu 1}$ is the viscous damping function, given by equation (2.13).

$$\mu_t = \rho\tilde{\nu}f_{\nu 1} \tag{2.12}$$

$$f_{\nu 1} = \frac{\chi^3}{\chi^3 + C_{\nu 1}^3} \tag{2.13}$$

$$\chi = \frac{\tilde{\nu}}{\nu} \tag{2.14}$$

In equation (2.11) the rate of production of $\tilde{\nu}$ is related to the local mean vorticity as

$$\tilde{\Omega} = \Omega + \frac{\tilde{\nu}}{(\kappa y)^2} f_{\nu 2}, \tag{2.15}$$

where Ω represents the mean vorticity. From equations (2.11) to (2.15), $f_{\nu 2}$ and f_w are further wall functions, χ is an intermediate variable, σ_ν is the turbulent Prandtl number, κ is the von Kárman constant, y is the distance to the wall, and C_{b1}, C_{b2}, $C_{\nu 1}$, and C_{w1} are model constants. These values were tuned for external aerodynamic flows and can be consulted in reference [22], by P. R. Spalart and S. R. Allmaras.

This turbulence model was specifically developed for aerospace applications, namely wall-bounded flows, as is the case of flow around airfoils. The model was shown to give good performance when evaluating boundary layers with adverse pressure gradients, an important characteristic while predicting aerodynamic stall. Although its advantages at modelling near-wall flow behaviour, it lacks calibration for general industrial applications and produces relatively larger errors for free shear flows, as is the case of a massive separation occurrence, free wakes with pressure gradients or free vortices [14][21][22].

2.2.2 Moving Parts Inside the Domain

In order to simulate moving parts within the fluid domain, such as the case of rotating blades, further adaptations need to be made to the governing equations previously described in this chapter. Different routes are possible:

- Instead of actually simulating the rotating blades, their influence in the rest of the domain can be modelled by introducing sources in the volume that would be occupied by the rotors, by utilizing BEMT to calculate the velocity that is induced in the flow while it goes through the rotor disk. This is called the Actuator Disk method and, numerically, is the least computationally demanding to calculate, but has a major disadvantage that to use BEMT, one should know the flow velocity that is entering the actuator disk. This velocity is part of the whole domain solution, which is dependent on the induced velocity obtained from BEM theory. This results in a highly iterative process and if not enough care is taken during this process, one might arrive to a solution which is of no physical meaning;

- Other possible path is to divide the domain into different zones, and model the zones around the moving parts with a moving reference frame. Following this technique, the flow around the moving part can be modelled as a steady-state problem with respect to the reference frame, by modifying the equations of motion to incorporate the additional acceleration terms that occur due to the transformation from stationary to a moving reference frame. This technique would be equivalent to stopping the moving body at an instant in time and visualize the flow field around it;

- Another, is to also divide the domain into different zones, but to move the boundaries of a cell zone relative to other boundaries of the same zone, and to adjust the mesh accordingly. With this technique, the nodes that define the cells in the domain must be updated as a function of time, hence solutions using this method are inherently unsteady;

- Lastly, and probably the most resource intensive route, is to utilize dynamic meshes. With this approach, the geometry near the moving walls is re-meshed in each time step to account for the body movement.

Three methods were considered in this thesis, the Multiple Reference Frame (MRF), belonging to the second group, and the Overset Mesh and Sliding Mesh methods, belonging to the third group.

Multiple Reference Frame

This method requires that the domain be divided into multiple cell zones, with well defined interfaces between them. The interface separating a moving region from neighbour regions must be defined such that no frame velocity component exists normal to the boundary. This means that, for rotating zones, the interfaces must be surfaces of revolution about the frame's axis of rotation. For the case of a frame which is translating, its boundaries must be parallel to the translational velocity vector.

As briefly explained before, some modifications are made to the governing flow equations to account for the moving reference frame [14].

First, a coordinate system is considered with a translating linear velocity $\mathbf{V}_t$, and a angular velocity $\boldsymbol{\omega} = (\omega_x, \omega_y, \omega_z)$ relative to a stationary reference frame, as shown in figure 2.3

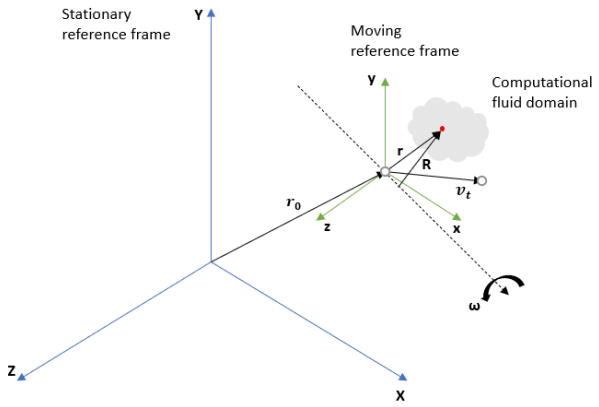

Figure 2.3: Stationary and Moving Reference Frames [14].

The origin of the moving coordinate system is located by the position vector $\mathbf{r}_0$ and an arbitrary point in the computational fluid domain is defined in the moving reference frame with the position vector $\mathbf{r} = (x, y, z)$ from the moving coordinate system.

Then, fluid velocities are transformed between reference frames through the following relations

$$\mathbf{U_r} = \mathbf{U} - \mathbf{V_r} \tag{2.16a}$$

$$\mathbf{V_r} = \mathbf{V_t} + \boldsymbol{\omega} \times \mathbf{r}, \tag{2.16b}$$

where $\mathbf{U_r}$ is the fluid velocity relative to the moving reference frame, $\mathbf{U}$ is the absolute velocity in the stationary reference frame, and $\mathbf{V_r}$ is the velocity of the moving frame relative to the stationary frame.

When the governing equations presented up to this point are solved in the moving reference frame, new acceleration terms appear in the momentum equations due to the reference frame movement. This equation can be formulated in two ways. Either solving for the relative velocities as the dependent variables, known as the relative velocity formulation, or solving for the absolute velocities as the dependent variables, known as the absolute velocity formulation.

The common practice is to use the relative velocity formulation in cases where most of the domain in under rotation, as is the case of a large impeller in a mixing tank, whereas the absolute velocity formulation is used in cases where only a small part of the domain is under rotation, like the case of a small fan in a big room. In this thesis the goal is to study the aerodynamic behaviour of a VTOL UAV, where only the rotor blades are rotating, while the rest of the UAV and the surrounding fluid domain are stationary, hence the absolute velocity formulation is more appropriate.

The governing flow equations for a steadily rotating frame (the rotor blades are rotating at a constant speed), in the absolute velocity formulation are:

$$\frac{\partial \rho}{\partial t} + \nabla \cdot \rho \mathbf{U_r} = 0 \tag{2.17}$$

as the conservation of mass,

$$\frac{\partial}{\partial t}(\rho \mathbf{U}) + \nabla \cdot (\rho \mathbf{U_r} \mathbf{U}) + \rho \left[\boldsymbol{\omega} \times (\mathbf{U} - \mathbf{V_t})\right] = -\nabla p + \nabla \cdot \bar{\tau} + \mathbf{F} \tag{2.18}$$

as the conservation of momentum equation. In this formulation the Coriolis and centripetal accelerations are simplified into a single term $([\boldsymbol{\omega} \times (\mathbf{U} - \mathbf{V_t})])$ [14].

These are the equations solved in the moving parts of the domain, while the classic conservation equations are solved in the stationary zones. At the interface between zones, continuity of the absolute velocity is required to provide the correct neighbour values of velocity for the subdomain under consideration. When using the absolute velocity formulation, the governing equations in each zone are written corresponding to the zone's reference frame but all velocities are stored in the absolute frame, thus, no local reference frame transformation is required. Scalar quantities like pressure and turbulence are simply determined from adjacent cells since their values don't depend on the reference frame they are being measured from.

This model, however, does not capture the unsteady interaction between stationary and moving parts. Despite this, it can provide a reasonable approximation of the flow in applications where the interaction between moving and rotating parts is relatively weak and the flow is relatively uncomplicated at the interfaces between different zones.

Sliding Mesh

In this formulation, the integral form of the conservation equation for a general variable, ϕ, on a given control volume, V, whose boundary is moving is written as:

$$\frac{d}{dt}\int_V \rho \phi dV + \int_{\partial V} \rho \phi \left(\mathbf{U} - \mathbf{U}_g\right) \cdot d\mathbf{A} = \int_{\partial V} \Gamma \nabla \phi \cdot d\mathbf{A} + \int_V S_\phi dV, \tag{2.19}$$

where $\mathbf{U}_g$ is the velocity of the moving mesh, $\mathbf{A}$ is the area vector normal to the control volume surface, Γ is the diffusion coefficient, S_ϕ is the source term of ϕ, if there's any, and ∂V represents the boundary of the control volume, V. This equation applies to all model equations, such as momentum, energy, turbulence, etc.

As formerly mentioned, this equation is applied to the control volumes inside the moving zone within the domain and flow information is transmitted freely between the moving and static zones through the mesh interface. It is important to note that zones must be defined such that the prescribed motion allows them to keep contact with each other along the non-conformal interface, that is, both zones "slide" along the interface boundary. For rotating parts, the moving zone must be a body of revolution, usually a cylinder, aligned with the axis of rotation, and the static zone must engulf it completely [14].

Overset Mesh

Unlike with the Sliding Mesh approach, where cell zones are connected along matching face zones, overset interfaces connect cell zones by interpolating cell data in overlapping regions. For this to be successful, the cell zones must overlap sufficiently. The model needs to be constituted of at least two cell zones, a background mesh which represents the broader domain, and a component mesh around the body of interest. This body can either be stationary or moving [23].

When the simulation is initialized, the necessary connectivity between the different meshes is established. Figure 2.4 shows an example of the initial meshes and the resulting cells which will be used in the simulation once the connectivity is established. In this process, cells that fall outside the computational domain are classified as dead cells. The cells where the flow equations are solved are referred to as solve cells, receptor cells receive data in a mesh interpolated from another mesh and donor cells are the cells where the receptors get their data from.

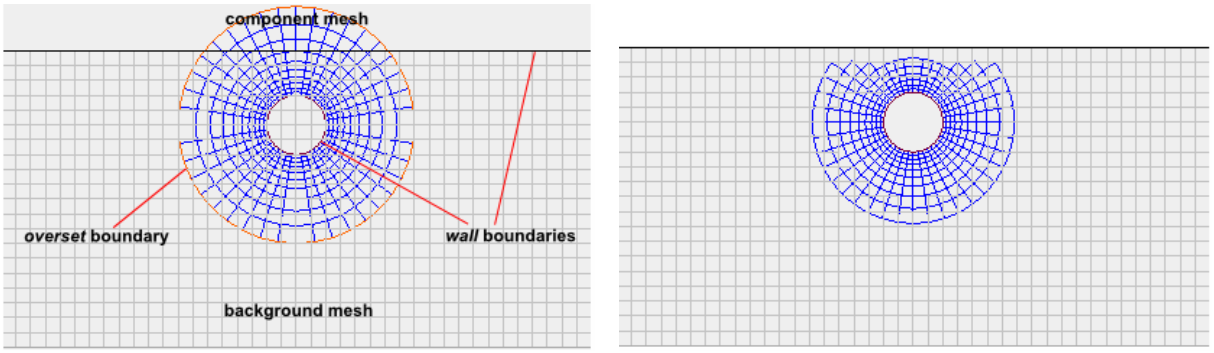

(a) Overset Component and Background Mesh.

(b) Solve Cells after Initialization.

Figure 2.4: Overset Mesh Interface[23].

Using this approach, the governing equations are the same as the ones employed with the Sliding Mesh model, the main difference being how the interface between different cell zones is treated, as explained above. One important aspect of overset meshes is that, when mesh motion is present, the interface connectivity must be re-calculated in each time step. This introduces an increase in computational time required.

As previously stated, the usage of a moving mesh means that the solution is inherently transient. In this regard, the selection of the time step size is of utmost importance for better accuracy and stability. The ideal time step should be chosen such that the relative mesh motion does not exceed the length of the smallest cell in the overset overlap region, in a given time step. This means that, for a fine spatial discretization, an even finer temporal discretization is required, resulting in more time steps needed to simulate a given time interval.

Chapter 3

Application, Verification and Validation of the Chosen Methods

3.1 Pre-Processing

3.1.1 Geometry Setup

In order to have a suitable geometry to be used in a simulation different steps are necessary, starting with modelling the UAV geometry. The initial geometry, shown on figure 3.1 was provided by Beyond Vision and was created using the Computer Aided Design (CAD) software, SolidWorks. Some tweaking was done to the original geometry as will be explained further down in this section.

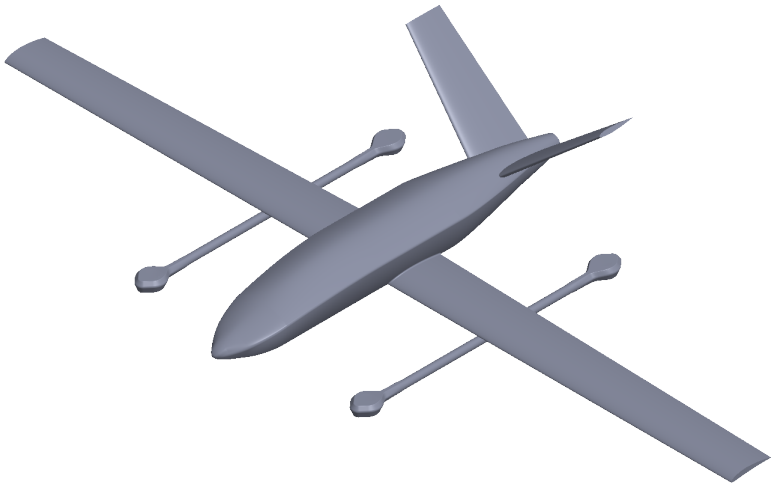

Figure 3.1: UAV geometry provided by Beyond Vision.

Beside the base beVTOne geometry, also the rotor blades had to be modelled. The UAV was dimensioned to use 18 inch rotors. Based on the requirements, a rotor with a pitch of 8 inches was selected from APC Propellers, who made available a file with the geometric definitions of said propeller, for the

purpose of this work. Base on the provided file the blade geometry on figure 3.2 was modelled using SolidWorks.

(a) Isometric view. (b) Side view.

Figure 3.2: Rotor blade geometry.

Note that both clockwise and counter-clockwise models were made as to keep the torques balanced.

Since the goal is to simulate the vehicle's aerodynamics, only the exterior surface is important to be modelled and the interior is simply considered a solid body.

Geometry Clean-up

During the geometry clean-up phase, some small details are simplified and imperfections in the CAD file are corrected.

Usually, geometries to be studied include small details such as hinges, screw holes, crevices or protrusions which have a negligible influence in the overall flow but, due to their fine dimensions, require a high mesh resolution around them. This results in a drastic increase in the number of mesh elements, translating in a higher computational cost without bringing tangible returns. For this reason, it is common practice to remove these geometries.

The model had already gone through that geometry simplification process, however two zones still required attention. Both the wing and v-tail geometries are generated by importing a file with airfoil coordinate points, which SolidWorks uses to create a continuous line through the usage of splines. This method can introduce odd behaviours close to the trailing edge, which not only creates misrepresentations of the real geometry, but also introduces highly skewed elements when meshing the wing surface, which can later lead to solver instability or poor quality results.

To decrease that influence, the trailing edge is truncated and replaced by a half circumference. This change eases the meshing procedure while the impact on the results might be neglected since the cut zone size is very small when compared to the full wing chord. It also better represents the physical wing, since manufacturing processes don't allow for the wing trailing edge to be a sharp edge, but to have some thickness. The changes to the airfoil profile are shown in figure 3.3

Another goal in this phase is to repair ill-defined geometry features. Even though the geometry may appear correct at a broader scale, some small scale irregularities such as self-intersecting surfaces, some volumes intersecting others, gaps may be present and very small faces can exist which complicate

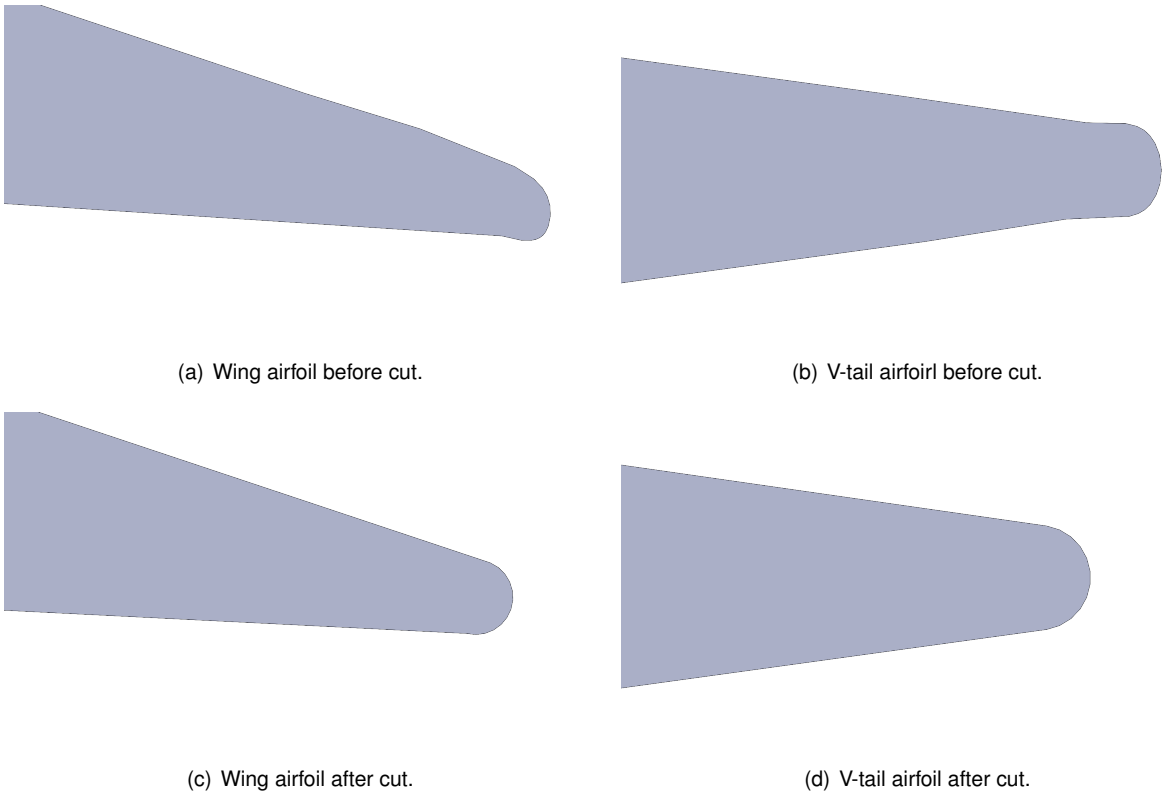

(a) Wing airfoil before cut.

(b) V-tail airfoirl before cut.

(c) Wing airfoil after cut.

(d) V-tail airfoil after cut.

Figure 3.3: Wing and V-tail trailing edge modifications.

the mesh generation. In order for the utilized meshing software, ANSYS Meshing [24], to produce a mesh, the provided geometry must consist of an entirely closed surface or else the process fails.

This step was done using the ANSYS Spaceclaim CAD software [25]. This software provides a series of geometry repair tools targeted at Computer Aided Engineering (CAE) applications like CFD or Finite Element Analysis (FEA). The tools allow the user to:

- Detect and fix gaps and missing faces in a surface body;
- Remove extra edges and duplicate faces;
- Fix curves by removing gaps, duplicates and small curves below a specified threshold;
- Detect and remove small faces below a give threshold;
- Fix edges that don't lie precisely at the interface of two faces;
- Identify and fix interfering bodies.

Some of these bad geometries identified by Spaceclaim are shown in figure 3.4.

Geometry Preparation

Lastly, before exporting the geometries to the meshing software, some last operations were made to them in order to generate the fluid domains. Also, volumes around areas of interest were created to later be used as bodies on influence in ANSYS Meshing to locally refine those areas. Due to the symmetry

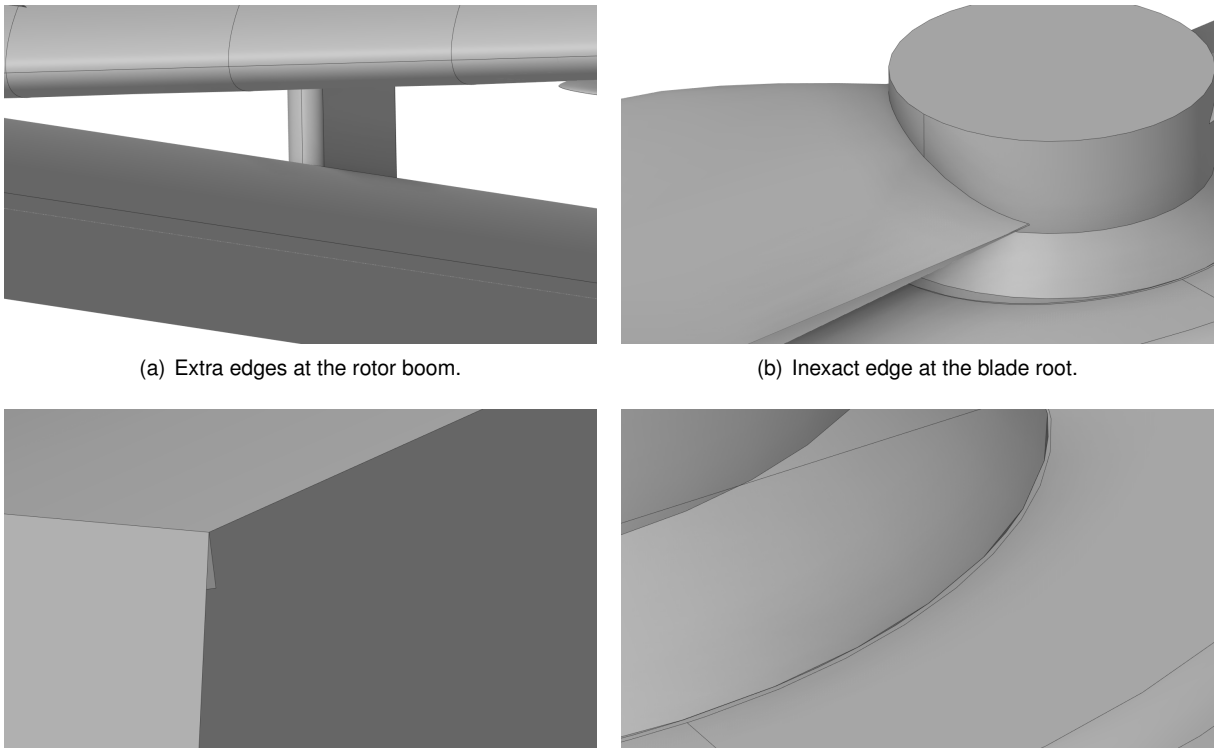

(a) Extra edges at the rotor boom.

(b) Inexact edge at the blade root.

(c) Sharp edge in the fuselage.

(d) Small faces in the rotor fairing.

Figure 3.4: Geometry clean-up in Spaceclaim.

characteristics of the study in cause, the domain was cut in half through the symmetry plane to reduce the total computational size.

The domain sizes and refinement volumes were modelled depending on the flight phase intended to be simulated. For horizontal flight, refinement volumes were created around the wings, fuselage and tail, their respective wakes, and all the rotor assembly structures. For vertical flight, refinement volumes were created around the wings, fuselage and tail, as well, around the rotor disks and their vertical wake, and on the tail's vertical wake near the rear rotor. Finally, for the transition flight phase, both refinement volumes were combined since the flow will present mixed behaviours from vertical and horizontal flight. The chosen refinement volumes are shown in figure 3.5.

As above mentioned, the meshing software requires that the fluid domain be fully enclosed. Due to convenience of use, ANSYS Design Modeler [26] was used in this task, where a boolean operation was employed to subtract the UAV geometry from control volume correspondent to the fluid domain. The resulting body is a solid which occupies the entire fluid domain.

In the cases where rotor blade motion is present, the domain had to be divided, as explained in section 2.2.2, into near-body domains for the front and rear rotors, and a background fluid domain, for the remainder volume. Together they form a multi-body part that can be exported to ANSYS Meshing.

Before exporting the geometry to the mesher, individual surfaces of interest were named so that local sizing can be assigned to them in the meshing phase and boundary conditions individually specified during the simulation setup.

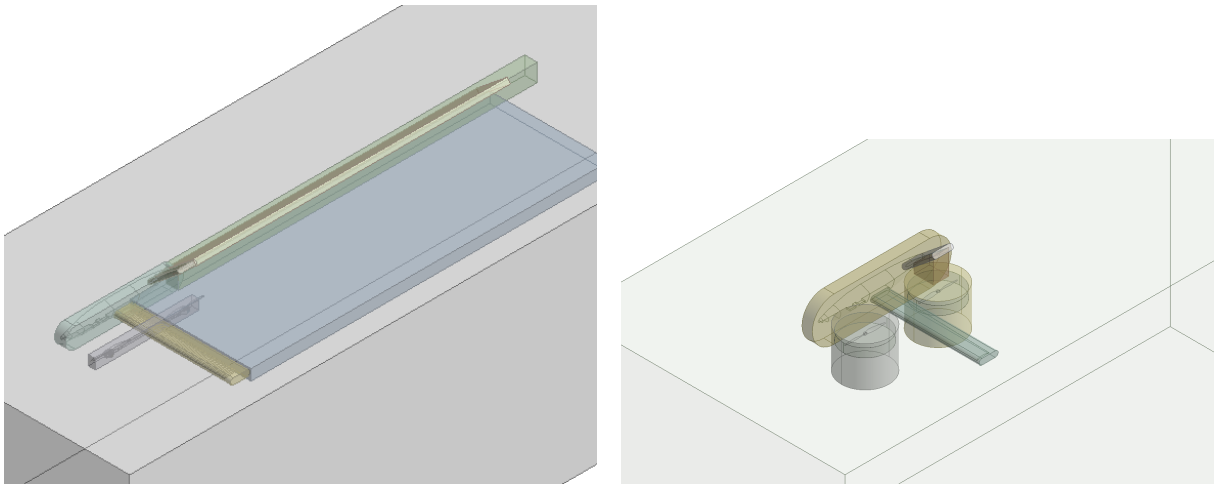

(a) Horizontal flight. (b) Vertical flight.

Figure 3.5: Refinement Volumes.

3.1.2 Mesh Generation

Once the geometry is ready, it must be discretized in order to solve the RANS equations in each individual cell. Figuring out the right spatial discretization for a given problem is one of the most important and time consuming parts of the CFD process. Too coarse of a mesh will fail to accurately capture the flow's intricate behaviour, while an extremely fine mesh results in a steep increase in the computational time required.

The first step is to decide the mesh generation method to be employed. ANSYS Fluent can solve for either type of mesh that is chosen, structured or unstructured.

Structured meshes, composed by hexahedra, usually offer higher quality elements, better alignment of the elements with the flow, which translates to better convergence, and require less memory to store the element connectivity data since it is implicitly defined within the elements. This kind of mesh has the least amount of numerical diffusion [27]. Despite these advantages, they suffer from a limited geometry flexibility as they lack the capability to model complex geometries. Beside this, an extra effort needs to be put into setting up this types of meshes as they require more manual user intervention[16].

On the other hand, unstructured meshes have become the most widely accepted type used due to their versatility, ease of implementation and highly automated use. For these reasons, despite structured meshes presenting slightly better performance advantages, an unstructured mesh was chosen since the geometry to be meshed presents complex features which would require a longer time to achieve the desired quality.

Within unstructured meshes there are two main types of building elements, tetrahedra and polyhedra. Tetrahedral meshes are the easiest to implement and have the highest flexibility to mesh complex geometries but, if stretched excessively, they become highly skewed, degrading the quality of the solution. This type of mesh has the highest numerical diffusion [27]. Sosnowski in [27] argues that polyhedral meshes have a level of numerical diffusion comparable to that of hexahedral meshes and can be easily applied even to very complex geometries.

The higher number of cell neighbours, when compared to hexahedral and tetrahedral meshes, allows

for an improved calculation of gradients. As a consequence of this, numerical diffusion is reduced in cases where the flow is not aligned with any of the cell faces, as is to be expected with the high complexity flow around the rotor blades and other UAV components. The three mentioned mesh types are shown in figure 3.6.

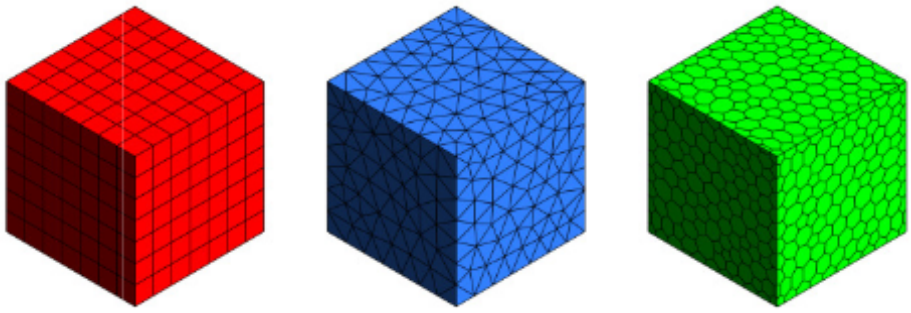

Figure 3.6: Examples of mesh types: Hexahedral, tetrahedral and polyhedral [27].

Sosnowski concludes that polyhedral meshes contribute to a higher stability, fewer iterations to achieve a converged solution, and that fewer elements are needed to reach mesh convergence. For the aforementioned reasons, polyhedral meshes were used in this thesis.

A polyhedral mesh is built from a tetrahedral mesh by decomposing the tetrahedral cells into multiple sub-volumes and then by rebuilding them into polyhedra. This functionality is implemented into ANSYS Fluent. To do it, a tetrahedral mesh was created in ANSYS Meshing, exported to ANSYS Fluent, and there converted into a polyhedral mesh.

With the base meshing method decided, a mesh convergence study was performed to identify the adequate dimensions the elements should have to achieve a solution that minimizes the influence of the mesh itself, and is governed by the physics of the problem. The sizing of the UAV components was based on guidelines provided by Beyond Vision based on previous studies, while mesh studies were performed to the rotors.

In said studies, an initial simulation was performed with a coarse mesh followed by successive finer meshes. In each simulation variables of interest were monitored like the propeller's thrust and torque. Once these values became constant, within a defined threshold, after successive refinement, the solution was deemed independent of the mesh and the smallest independent mesh was used in further simulations.

Surface Mesh Sizing

ANSYS Meshing [24] offers different control options to specify the surface mesh size. For a given surface, a target edge size is specified. Moreover, the software allows the use of advanced size functions, specifically the curvature size function, where a curvature normal angle is specified, as well as a minimum cell size. With this tool enabled, the mesher refines each element, up to the minimum cell size, to achieve a specified normal angle between adjacent elements, allowing for a better resolution in zones with high curvatures. This not only yields a more accurate representation of the geometry that is being

discretized, as well as allows for a better solution in zones with high curvatures since in those zones, like the wing leading edge, high gradients are developed and a fine mesh is required to accurately capture them.

Figure 3.7 shows the difference between not using and using curvature size function, while meshing the wing surface. It can be seen that by using curvature size function both the leading edge and trailing edge become significantly better refined.

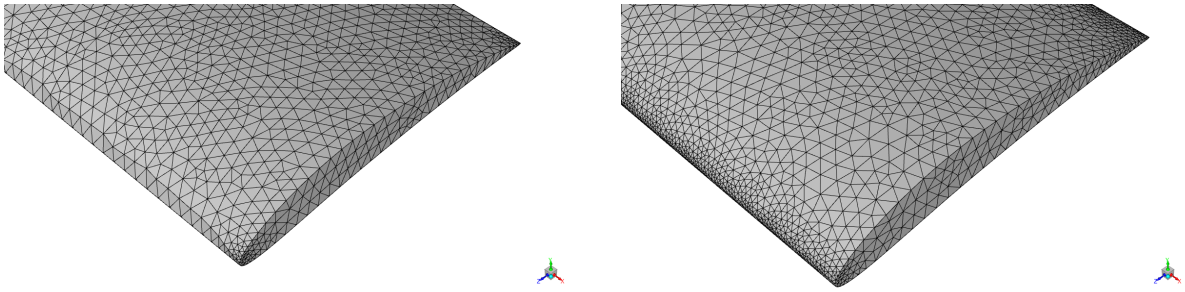

(a) No curvature size function.

(b) With curvature size function.

Figure 3.7: Wing surface meshing.

The target cell sizes, curvature normal angles and minimum cell sizes were specified for every surface and these values are presented in tables 3.1.

Table 3.1: Surface target size.

Surface	Cell size (mm)			Curvature Normal Angle (°)			Cell min. size (mm)		
	Horizontal Flight	Vertical Flight	Transition Flight	Horizontal Flight	Vertical Flight	Transition Flight	Horizontal Flight	Vertical Flight	Transition Flight
Fuselage	4.0	5.0	4.0	14	18	14	2.0	2.0	2.0
Rotor Blades	1.0	1.0	1.0	15	15	15	0.5	0.5	0.5
Rotor Hub	2.0	2.0	2.0	15	15	15	1.0	1.0	1.0
Rotor Boom	4.0	-	-	14	-	-	0.8	-	-
Tail	4.0	3.0	3.0	14	15	14	2.0	1.0	1.0
Wing	4.0	4.0	4.0	14	15	14	2.0	1.0	1.0

Inflation Layer Definition

Inflation layers, also known as prism layers, are of extreme importance at capturing the development of boundary layers near walls since boundary layers can have a high impact in the global aerodynamics in study, specially when adverse pressure gradients and flow separation might be present.

Boundary layers are characterized by having accentuated velocity gradients in the normal direction to the wall, thus a fine resolution mesh is required in that direction to capture the steep gradients. Furthermore, the closest region to the wall, called the viscous sub-layer, is of utmost importance and so, ANSYS Fluent utilizes wall functions to accurately model the flow velocity between the wall and the first element. In order for the wall treatment to be accurate the dimensionless wall distance, y^+, must be near or less than one [14]. The dimensionless wall distance is defined by equation (3.1) a) and through algebraic manipulation one can arrive at the desired first layer height[16].

$$y^+ = \frac{u_t y}{\nu}, \quad (3.1a) \qquad u_t = \sqrt{\frac{|\tau_w|}{\rho}}. \quad (3.1b)$$

In this equation y is the distance to the wall, u_t is the friction velocity, which is dependent of the wall shear stress, τ_w. The wall shear stress is itself part of the solution, meaning that this value can't be known beforehand. Despite this, it can be estimated using Prandtl's expression for the friction coefficient in flat plates in turbulent regime as follows:

$$\tau_w = \frac{1}{2}\rho U_\infty^2 C_f, \quad (3.2a) \qquad C_f = 0.074 Re_L^{-0.2}, \quad (3.2b)$$

where U_∞ is the free stream velocity and Re_L is the characteristic length Reynolds number.

Using these expressions, an initial estimation of the first layer height is obtained, which is then tweaked based on the results from the mesh independence studies, guaranteeing a wall y^+ below one.

To further define the inflation layers, the total number of layers and their growth rate must be specified. A geometric growth rate is employed where a particular layer is defined by $h_0 * r_g^{n-1}$, where h_0 is the first layer thickness, r is the growth rate and n is the layer number.

For an accurate coverage of the boundary layer, ANSYS Fluent recommends using between ten and twenty layers, and it should be designed so that around fifteen elements are actually covering the boundary layer [14]. Following these guidelines, as well as the results from the mesh independence study, the meshes that balance an accurate solution while reducing the computational requirements are presented in tables 3.2.

A detail that should be accounted for when generating inflation layers is that the total number of layers in contiguous surfaces should be kept constant, or else, ANSYS Meshing uses stair stepping to transition between the prismatic elements and tetrahedral elements, generating pyramidal elements on those locations. These elements are usually undesirable as they generally have poor quality.

Table 3.2: Inflation layer definition.

Surface	First Layer Thickness (mm)			Growth Factor			Number of Layers		
	Horizontal Flight	Vertical Flight	Transition Flight	Horizontal Flight	Vertical Flight	Transition Flight	Horizontal Flight	Vertical Flight	Transition Flight
Fuselage	0.01	0.05	0.01	1.4	1.2	1.4	18	15	18
Rotor Blades	0.005	0.001	0.001	1.3	1.3	1.3	18	15	15
Rotor Hub	0.005	0.001	0.001	1.3	1.3	1.3	18	15	15
Rotor Boom	0.01	-	-	1.2	-	-	18	-	-
Tail	0.01	0.05	0.01	1.35	1.2	1.35	18	15	18
Wing	0.01	0.05	0.01	1.35	1.2	1.35	18	15	18

Volume Mesh Sizing

The remaining step to obtain a mesh suitable for simulation is to define the volume mesh parameters. A global mesh size of $100mm$ was defined for all the case studies. From the global mesh size, further local refinements were made using the bodies of influence described in 3.1.1 and shown in figure 3.5. These sizes are presented in table 3.3.

Table 3.3: Volume target size of the volumetric refinement.

Volumetric Refinement	Target Size (mm)		
	Horizontal Flight	Vertical Flight	Transition Flight
Fuselage	10.0	10.0	10.0
Fuselage Wake	20.0	-	20.0
Rotor and Rotor Boom (Horizontal)	10.0	-	-
Rotor Domain	-	10.0	10.0
Rotor Wakes (Vertical)	-	20.0	20.0
Tail	10.0	10.0	10.0
Tail Wake (Horizontal)	20.0	-	20.0
Tail Wake (Vertical)	-	10.0	10.0
Wing	10.0	10.0	10.0
Wing Wake	20.0	20.0	20.0

Final Mesh Remarks

Before proceeding further it should be noted that the rotor booms were not modelled neither in the vertical flight study nor in the transition study. As it had been explained in subsection 2.2.2 for both the MRF approach and the Sliding Mesh approach, the fluid domain needs to be divided into the moving zones and the background stationary zone.

As stated, the moving zones interface must be defined by a body of revolution around the zone's axis of rotation and every body inside the zone is assumed to be in solid rotation with the zone itself. For this reason, only the rotor blades themselves should be inside the rotating zone and the boom should be inside the background domain. Due to geometry constraints, no rotating zone can be created that allows for a good quality mesh between the rotor blades and the rotor casing/boom.

Moreover, as further explained in section 3.2, it is observed that the interface between fluid zones introduces slight discontinuities in the fluid velocity which can hinder the rotor wake development. For this reason, to obtain a more accurate depiction of the rotor wake, it is better not to define the interface immediately below the rotor blades, but to leave some clearance. Due to the previously stated lack of clearance, this is not possible.

Following the above information, it was decided not to model the boom in those cases, even though it influences the propellers performance, since the overall interaction between the propellers and other UAV components won't be majorly modified, meaning that the scope of this thesis isn't lost with this change.

The final mesh sizes, before and after conversion between tetrahedral and polyhedral, are presented in table 3.4. The meshes are then presented in figures 3.8, 3.9, and 3.10.

Table 3.4: Approximate mesh size utilized in each study.

	Tetrahedral Mesh ($\times 10^6$)	Polyhedral Mesh ($\times 10^6$)
Horizontal Flight	27.2	13.7
Vertical Flight	13.0	4.6
Transition Flight	19.6	8.7

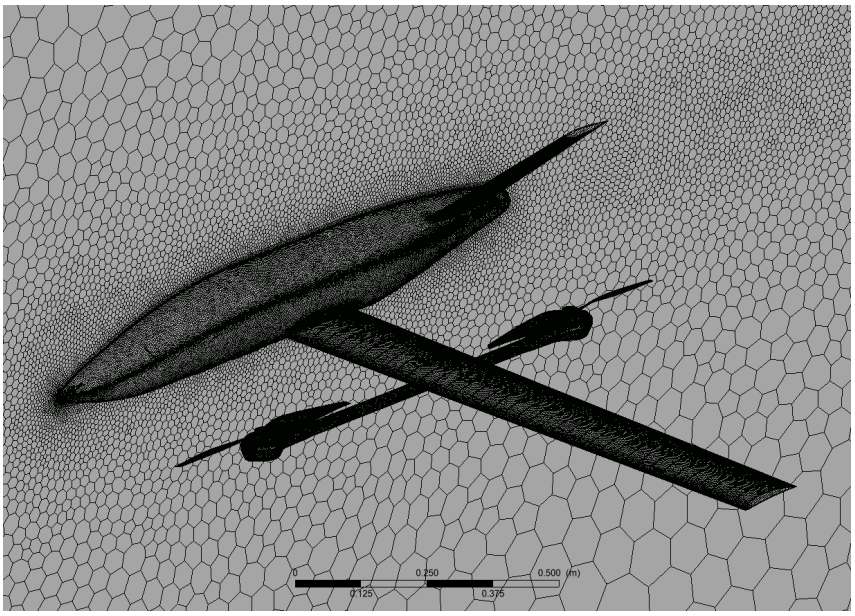

Figure 3.8: Polyhedral mesh utilized in horizontal flight.

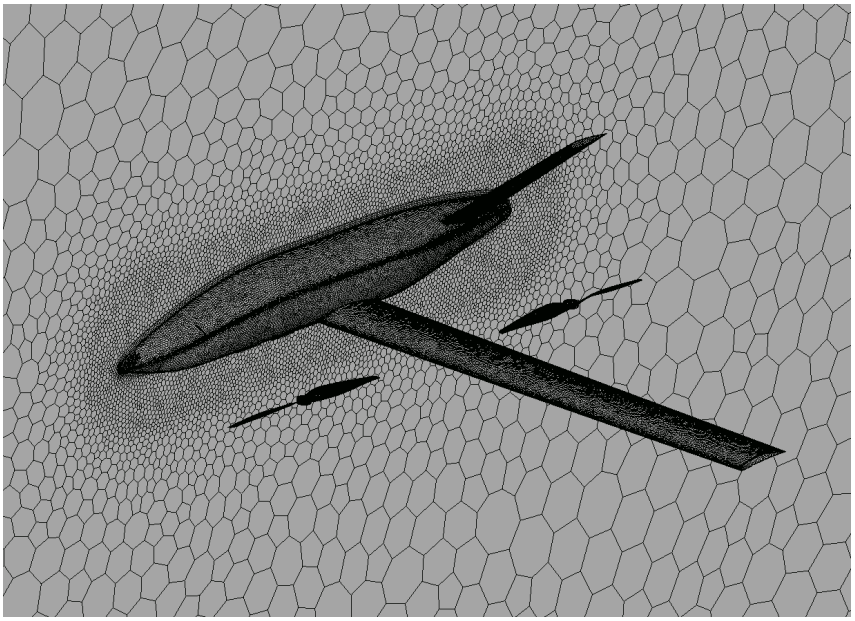

Figure 3.9: Polyhedral mesh utilized in vertical flight.

Contrary to what would be expected, there is a decrease in the total number of elements from the horizontal flight mesh to the others, even though in these flight phases there is an increased refinement near both rotors and their wakes. Despite their contribute to drag, the rotor booms do not influence the flow significantly in regards to its interaction with other components, but their relatively high geometric complexity, specially around the rotor fairings, requires a high number of elements. The fact that they are no longer modelled in vertical and transition flight can justify the reduction in mesh size.

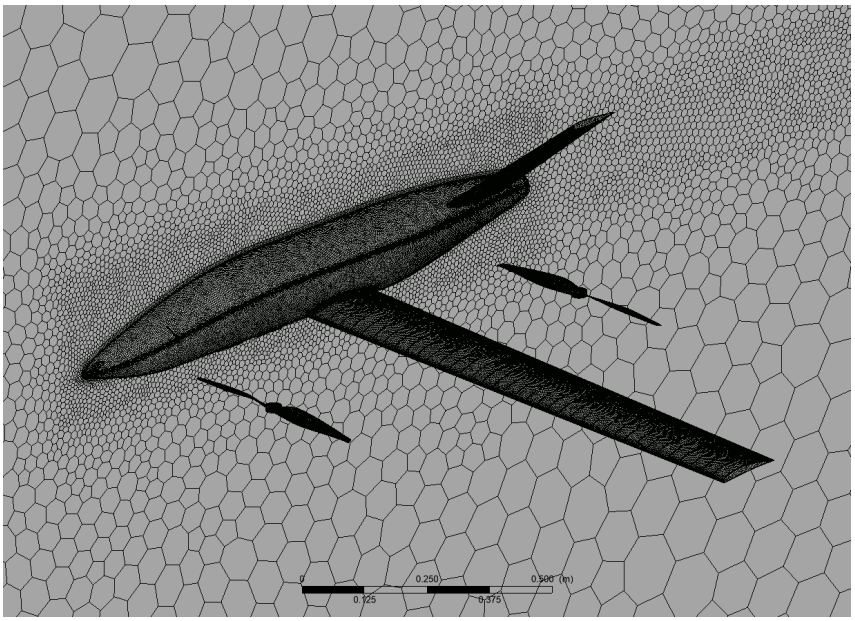

Figure 3.10: Polyhedral mesh utilized in transition flight.

3.1.3 Simulation Setup

Numerical Models

At a cruise velocity of $30m/s$ and flight altitude of $120m$, the Mach number and Reynolds number can be calculated through

$$M = \frac{U_\infty}{a} \qquad (3.3) \qquad \text{and} \qquad Re = \frac{U_\infty \bar{c}}{\nu}, \qquad (3.4)$$

where a is the free stream speed of sound. The flow is then characterized by a cruise Mach number of $M = 0.088$ and a Reynolds number of $Re = 3.04 \times 10^5$. This means that it can be treated as incompressible, however, the propellers have a tip Mach number of $M_{tip} = 0.32$ while rotating at the maximum studied speed. This value surpasses the typical guideline of $M = 0.3$ for incompressible flow, however, according to Anderson in [15], for $M < 0.32$ the variation in ρ due to compressibility effects is of less than five percent. Given that the high Mach numbers are located at such a small area of the overall region of interest and that the expected error induced from it is still at an acceptable range, it was decided to use an incompressible solver due to the lower computational requirements.

Furthermore, the Reynolds number indicates that the flow isn't likely to remain laminar but to transition to turbulent[16]. This factor, allied with the vorticity generated by the rotating blades, indicates that the flow is likely to have a strong turbulent behaviour, justifying the usage of models of turbulence, instead of using a laminar approach.

The RANS equations were, therefore, solved for incompressible flow, together with Menter's $k - \omega$ SST turbulence model. As mentioned in chapter 2, this model has been widely tested and verified in aeronautical applications. This factor, coupled with a better stability when compared with the Spalart-Allmaras turbulence model during the mesh independence study justified this decision. Coupled with the aforementioned equations, a low y^+ wall treatment was used to accurately describe the boundary

layers, as mentioned in subsection 3.1.2.

When modelling rotating zones using the MRF model, the steady-state solver was utilized, whereas with Sliding Mesh and Overset Mesh models the transient solver was utilized and a temporal discretization had to be specified. In both cases the time step was chosen with the goal of respecting the CFL condition, stated by

$$C = \frac{u\Delta t}{\Delta x} < 1, \tag{3.5}$$

where C is the Courant number, u is the velocity magnitude in a given element, Δt is the time step and Δx is the spatial discretization. Respecting this condition guarantees that during a time step the flow travels a distance shorter than an element's size. This condition is essential for convergence with explicit time discretizations, whereas implicit discretizations are unconditionally stable [21]. Despite this, while using an implicit time discretization, it is still important to respect the CFL condition as that yields a better description of transient phenomena.

Using an initial estimate based on the smallest target mesh size described in subsection 3.1.2 and the rotor tip speed, with a target of $C = 1$, a time step of $\Delta t \approx 9.2 \times 10^{-6} s$ was obtained. When running the simulation it was observed that an even smaller time step of $\Delta t \approx 2 \times 10^{-6} s$ was required. With such a small temporal discretization, at the angular velocity of the rotors, a total of 6550 time steps are required to simulate a full rotation. Since multiple rotations are required to obtain an accurate solution, this number proves to be prohibitively high in this type of engineering application. Furthermore, as later shown in 3.2, the results yielded using the MRF model prove to be accurate enough, thus this model ended up being used throughout the simulations.

Finally, the pressure-based coupled solver was chosen to solve the RANS equations. Even though this solver requires more memory than the segregated solver, its rate of convergence is significantly higher. This happens because with the coupled solver the momentum equations and the pressure based continuity equation are solved in a closely coupled manner, whereas with the segregated solver each equation is solved separately and must converge individually[14].

Boundary Conditions

As mentioned in section 3.1.1 a domain had to be created around the geometry in study. The domain boundaries must be located far away enough from the body of interest so that the user-specified boundary conditions do not affect the flow around the body in any non-physical way.

To do so, it is common practice, in horizontal flight, to locate the inlet boundary at a distance of 50 chords in front of the aircraft and the outlet was located at 75 chords away from the aircraft. The width of the domain was set up with 2.5 times the UAV half-span and the total height was set to 40 wing chords.

For vertical and transition flight the domain had to be defined based on testing to verify if the domain size was having an influence on the flow behaviour. Based on this study, the vertical flight domain was set with a total length of 17 rotor diameters, a width of 8 rotor diameters and a height of 9 rotor diameters. On the other hand, the transition flight domain had the upwind and downwind domains defined the same

way as in the horizontal flight domain, its width was set to 10 rotor diameters and its height with 10 rotor diameters above and below the rotor plane.

In transition flight, the domain below the UAV was sized such that the rotor wakes could fully develop vertically and then be carried away horizontally by the free stream, without impinging in the bottom boundary.

In all the cases being studied, the UAV and rotor surfaces were set to the No-slip Wall boundary condition, with the extra detail that in vertical and transition flight the rotor surfaces had to be defined as fixed in the stationary reference frame. The symmetry plane was also set to the equally named boundary condition in all the simulations.

In horizontal flight, the upwind, side, top and bottom faces of the domain were all set together as a velocity inlet. There, the flow velocity was specified based on its cruise magnitude of $30m/s$ and aligned with the Z-axis. The free stream turbulent kinetic energy and the turbulence frequency were also defined in this boundary based on Menter's guidelines[19] as:

$$\omega = \frac{U}{L}, \qquad \text{(3.6a)} \qquad k = \nu_t \omega \qquad \text{(3.6b)} \qquad \nu_t = 10^{-5}\nu, \qquad \text{(3.6c)}$$

where L is the approximate length of the computational domain.

Lastly, the downwind face was defined as a pressure outlet.

In vertical flight the top and all the side faces were treated as one Inlet and the bottom face as a pressure outlet. In hover, the inlet was assigned a pressure inlet as to allow the air velocity to be fully induced by the rotors, whereas in vertical climb a velocity inlet was assigned, based on the climb velocity with its direction aligned with the Y-axis. The turbulent parameters were defined as previously explained.

In transition flight the boundary conditions were defined as described in horizontal flight.

The final condition to be defined regards the rotor's motion in vertical and transition flight. In this cases both rotor fluid zones were assigned frame motion, with the axis of rotation defined for the front and rear rotors, with their respective directions of rotation, aligned with the Y-axis, and magnitudes. The front rotor is set to rotate counter clock-wise and the rear rotor is set to rotate clockwise.

Final Setup Remarks

Before running the simulation, monitors for the residuals and other variables of interest were created, like the wing lift and drag, the UAV drag, and the rotors thrust and torque. These monitors allow for a better assessment of the simulation's rate of convergence.

3.2 Verification and Validation

3.2.1 Verification and Validation of the Isolated Rotor

Before simulating the whole UAV at different flight stages, smaller simulations are conducted to assess the quality and accuracy of the solutions obtained from the chosen models.

First, simulations were run for an isolated rotor. After some mesh and domain studies, a cylindrical domain was created around it, with a height of 25 rotor diameters, centred on it, and a total diameter of 7.5 rotor diameters. The resulting mesh has approximately 1.3 million elements, with volumetric refinements around the rotor domain and wake, as seen in figure 3.11.

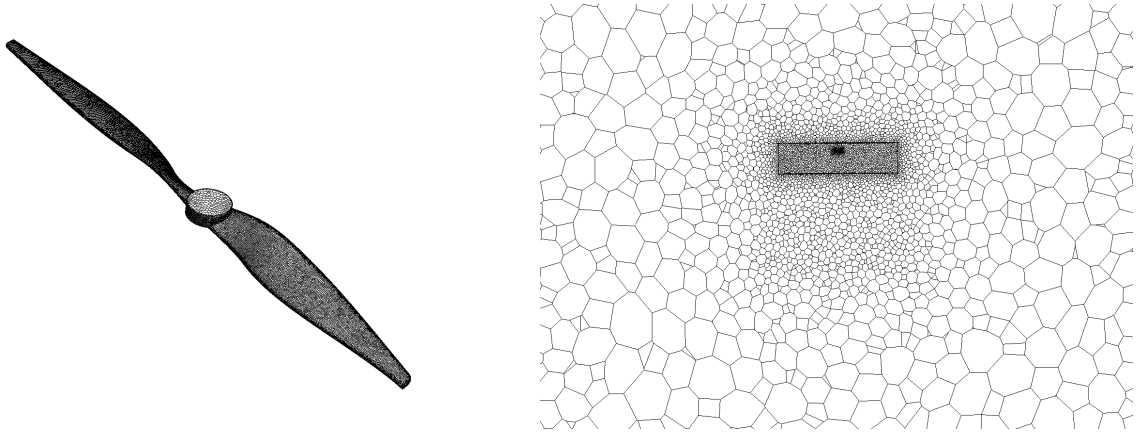

(a) Rotor blades. (b) Wake refinement.

Figure 3.11: Rotor Mesh.

A qualitative assessment on the flow of the chosen rotor at a velocity of 3000 and 4000RPM was performed, to verify whether the utilized models capture typical flow structures present in flows around rotors. The relative behaviour and shape of the flow structures at the aforementioned speeds was shown to be similar, with differences occurring in absolute values of the flow quantities. To avoid redundancy, in this subsection, only figures of the flow at 3000RPM are displayed, when making qualitative examinations of the flow, whereas when absolute metrics are evaluated, data from both simulations is presented.

Figure 3.12 shows velocity contours at the rotor's mid plane, with velocity vectors overlapped to it. A typical rotor wake is visible below the rotor plane, including its contraction, which is a known phenomenon identified in helicopter theory [28]. Moreover, the velocity profile on the wake presents the expected behaviour. Near the wake's centre, the induced velocities are low since blade velocities close to the hub are very small. Moving away from the wake's centre, the increase in blade velocity and the blade's high angles of attack, as shown in figure 3.2, induce much higher velocity magnitudes on the flow, represented by the red colour. Finally, as one gets closer to the blade's tip, it is visible that, even though this zone has the highest rotating velocity, the small chord and low angle of attack used to reduce the effect of tip vortices end up inducing lower vertical velocities on the flow. Furthermore, the external parts of the wake are characterized by high momentum diffusion with the non-perturbed air outside the wake.

A recirculation zone is found below the hub, identified by the low velocities in blue and the recirculating velocity vectors. The rotor induces a downward velocity on the air above it and when it interacts with the blunt hub it can't keep in contact with the hub and separation occurs.

Finally, even though it is subtle, discontinuities are visible on the velocity field at the interface between the internal and background domains. This justifies the earlier statement made when choosing the rotor domain size that it is a good practice to have some space between the rotor and the lower interface

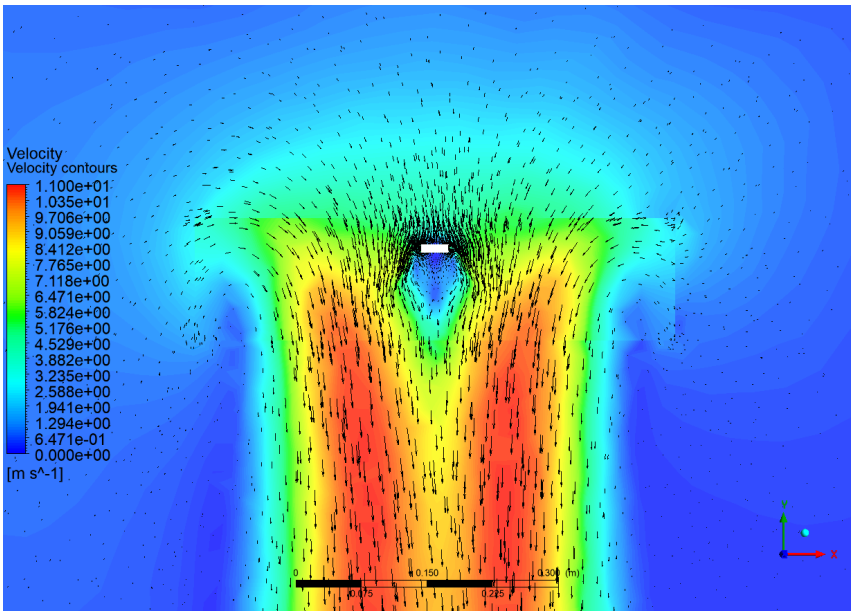

Figure 3.12: Velocity field and vectors on the rotor's mid section at 3000 RPM.

so that the initial part of the wake, marked by important velocity and pressure gradients, can develop correctly and that those gradients are not lost at the interface.

Vertical velocity, and pressure fields are displayed in figures 3.13 and 3.14, respectively, on disks located immediately above and below the rotor.

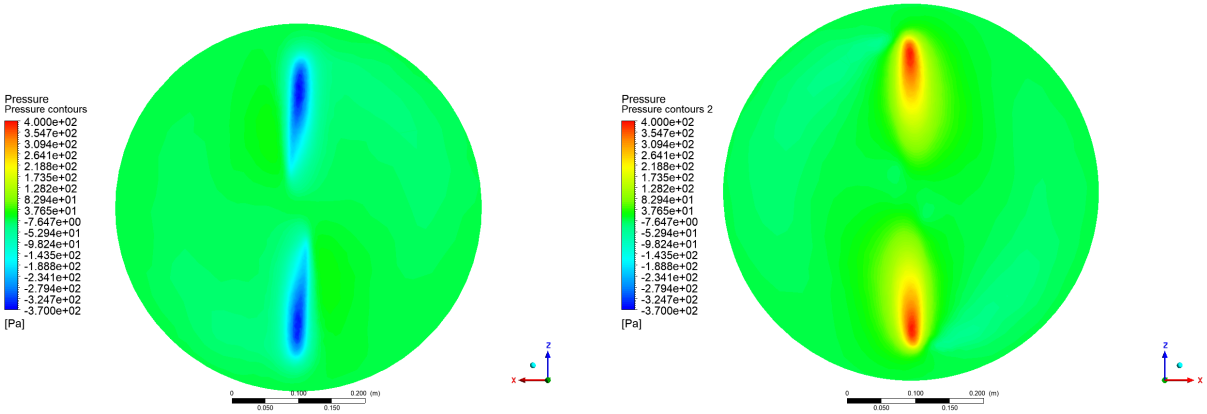

(a) Top disk.

(b) Bottom disk.

Figure 3.13: Pressure field visualization above and below the rotor at 3000RPM.

If the reader recalls correctly, the MRF method can be interpreted as taking a picture of the flow in a given instant and visualizing its characteristics. On figure 3.13 both the suction and pressure zones over and under the blades, respectively, can be identified. It is also noticeable that the magnitudes of pressure are stronger towards the blade tips, where they rotate faster. A dim blue trail left behind the blade tips can also be identified. This zone of lower pressure corresponds to the tip vortices, since pressure decreases in the vortex nucleus.

On figure 3.14 it can once again be verified that induced velocities are stronger in the middle of the rotor blades. At the outermost section of both disks a positive velocity is identified. This too is visualized

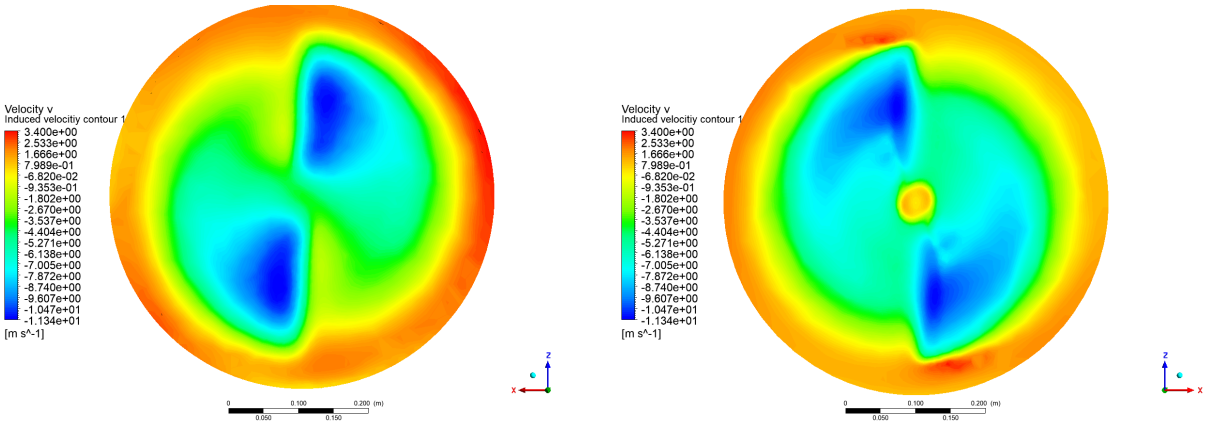

(a) Top disk.

(b) Bottom disk.

Figure 3.14: Vertical velocity field visualization above and below the rotor at 3000RPM.

in figure 3.12 and it is a common characteristic in rotor flow. Below the rotor disk pressure is higher than atmospheric pressure, and above it is lower. This pressure differential generates an upward flow velocity around the edge of the rotor disk, where the induced velocities by the rotor are smaller.

The last step to verify the quality of the solution is to calculate the mass fluxes across the domain's outer boundaries. If this value were to be different from zero, then mass would be accumulating or disappearing from inside the domain, depending on whether the total flux is positive or negative, which in this situation has no physical meaning. This verification was performed in every simulation and values in the order of magnitude of 10^{-6} and below were obtained, which can be considered negligible.

Finally, in order to validate the results, the aerodynamic coefficients of interest were analysed, namely the thrust coefficient, C_T, and the power coefficient, C_{PW}, and compared with the manufacturer's performance sheets [29] for the rotating velocities of 3000RPM and 4000RPM. Both aerodynamic coefficients are defined in equations (3.7) and (3.8), and the results are shown in table 3.5.

$$C_T = \frac{T}{\rho A \Omega^2 R^2} \tag{3.7}$$

$$C_{PW} = \frac{P}{\rho A \Omega^3 R^3} \tag{3.8}$$

The rotor radius is represented by the letter R, the area of the rotor disk by A, and thrust and power by T and P, respectively. The value for power is obtained by multiplying the torque applied by the blades on the rotor axis, retrieved from ANSYS Fluent, by their angular velocity.

Table 3.5: Comparison between numerical and test aerodynamic coefficients.

Rotation Velocity (RPM)	C_T		Error (%)	C_{PW}		Error (%)
	Exact Value	Numerical Value		Exact Value	Numerical Value	
3000	0.01094	0.01034	-5.524	0.001171	0.001126	-3.876
4000	0.01105	0.01045	-5.415	0.001167	0.001254	-6.969

From these results, one concludes that the chosen models can accurately be used to evaluate the performance of rotors, capturing important flow structures, while yielding results with an acceptable error relative to the actual rotor performance coefficients.

3.2.2 Verification and Validation of Rotor Interaction With Static Elements

In order to validate the capability of the chosen method to simulate the interaction of rotors with static elements, some procedures described by [30] were replicated numerically. In this article the authors performed Particle Image Velocity (PIV) measurements to document the wake generated by a rotor operating in ground effect above inclined surfaces and recorded its performance using a six-axis load cell.

The experimental setup consisted on a two blade rotor operating at one rotor radius distance above a ground plane which was inclined between $0°$ and $30°$. These conditions were replicated using the same rotor used throughout this thesis, as opposed to the one used by the authors of the article, at three different ground inclinations, namely horizontal ($0°$), $10°$, and $20°$.

To validate the chosen methods, the ratios of thrust produced In Ground Effect (IGE) over thrust produced Out of Ground Effect (OGE) are compared between the numerical and experimental data and the induced velocity fields on the wake are compared.

Figure 3.15 shows a comparison between the experimental data obtained by [30] and the current results. The results show a consistent underestimation of the ratios, however the results are very close, with the highest error being of 1.3%. With these results, one feels comfortable using the MRF model to simulate the interaction between a rotor and other static components.

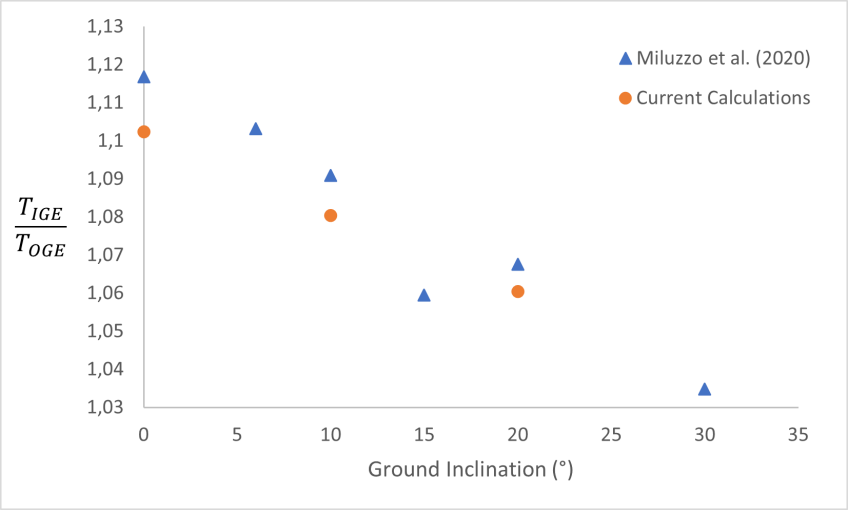

Figure 3.15: Validation of the numerical results with experimental data from Miluzzo et al. (2020)[30].

Furthermore, the resulting velocity magnitude fields obtained from the simulations are displayed in figure 3.16. When comparing the velocity contours from the numerical results with those from the experiments, one sees that the results are not the same. This does not mean, however, that the numerical results are incorrect. The blade used in the experiments in a non-tapered, untwisted wing, and, as such, stronger forces and induced velocities are present near the wing tip and then they decline almost linearly. This explains why the maximum velocities occur over such a narrow strip near the blade tip. On the other hand, the blade that was simulated has variable twist and taper that make it produce more thrust and induced higher velocities over a wider zone, hence the bigger zones in red present in figure 3.16.

Despite this, it is visible that the flow follows similar paths. Regarding the results with the ground at an horizontal position, one can see a division of the wake occurring in the mid plane, followed by low velocity zones where recirculating flow is present and then, away from the rotor axis, one sees fast flow being convected horizontally in a wake near the ground.

The results from when the ground is inclined also show a qualitatively similar behaviour. Just like in the experimental results, it is seen that the stagnation point that was previously located at the centre of the wake has now moved uphill and it now it doesn't divide the wake in half any more. It is seen that now the division occurs in the left side of the rotor disk and air that is located to the left of that division flows uphill, whereas air located to the right of the division flows downhill. Below the rotor hub a recirculation zone still occurs but this time it doesn't go all the way to the floor. The flow that comes from the right side of the disk moves with high induced velocities just like happened with horizontal ground and then flows downhill. The flow located at left side of the disk, but to the right of the dividing zone, moves downwards, with medium flow velocities, below the recirculating zone under the rotor hub and flows downstream, meeting the high velocity flow coming from the right side of the disk. As the inclination increases, the stagnation point and dividing zone move further uphill, the recirculation zone decreases size and moves closer to the hub, and the overall flow field remains qualitatively the same.

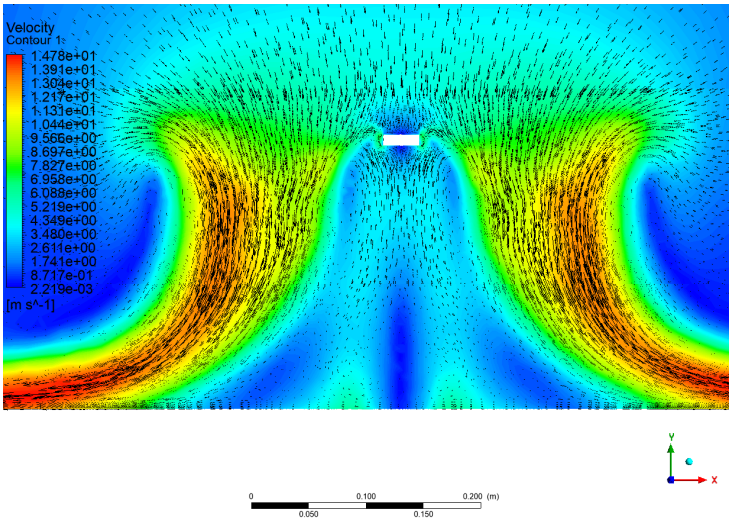

(a) 0° .

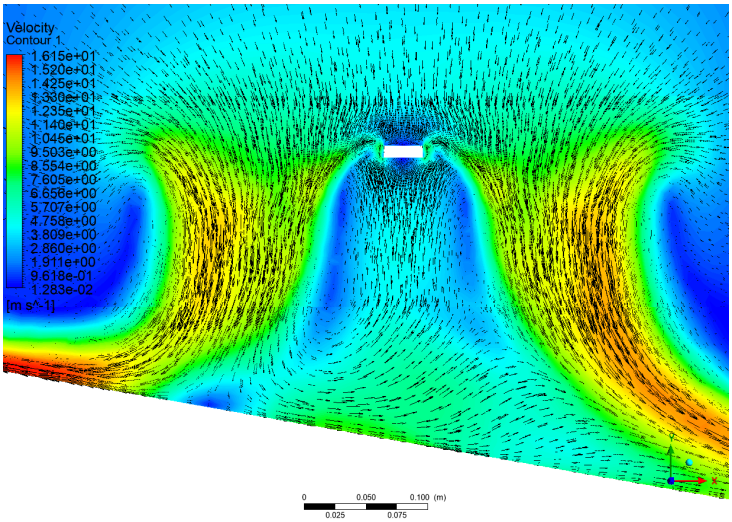

(b) 10 ° .

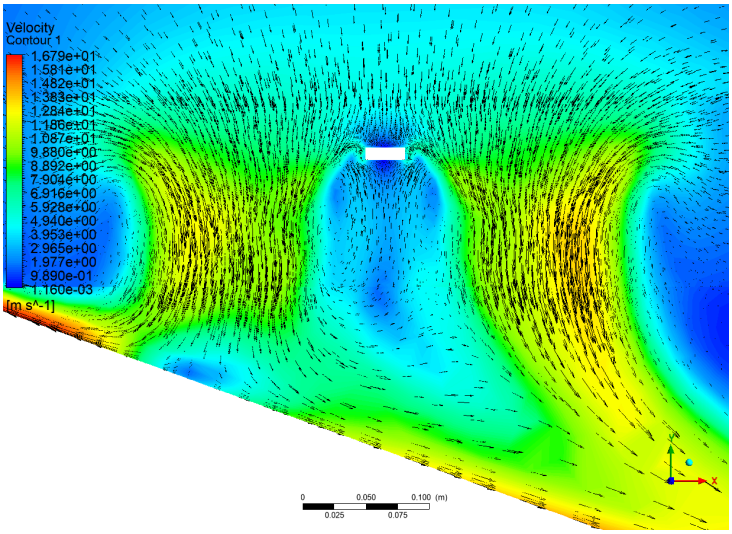

(c) 20° .

Figure 3.16: Contour of velocity magnitude of rotor operating IGE at 0° , 10° and 20° .

Chapter 4

Aerodynamic Analyses

4.1 Procedures

4.1.1 Horizontal Flight

In order to evaluate the aerodynamic interaction between the different UAV components, a baseline must be defined as a mean of comparison. For this purpose, the well studied conventional configuration[31] consisting of the wing, fuselage and tail was chosen. The expected flow structures are well known and documented, hence this geometry is well suited for the comparison with full configuration comprised of the conventional configuration plus the rotors and rotor booms.

After the first simulation, run at the cruise velocity of $U_c = 30m/s$, it was immediately evident that flow separation was occurring at the wing root due to the sharp angle formed between the wing and fuselage, and the developing boundary layers. This is a common effect and wing root fairings have been used for a long time as a way to reduce this type of interference drag. For this reason, a fillet was created between the wing root and the fuselage so that the transition is smoother. This new geometry was used from this point forward throughout the different flight phases. The root geometry before and after the change is presented in figure 4.1.

(a) Wing root without fillet.

(b) Wing root with fillet.

Figure 4.1: Wing root geometry.

To assess how the rotors and rotor boom influence the remaining configuration in cruise flight, an

equivalent simulation with the full geometry was run and the aerodynamic coefficients and flow structures were compared with the previously mentioned conventional geometry.

Furthermore, to evaluate how the rotor positions relative to the wingspan influence the lift and drag distribution, more simulations were performed while changing the rotor positions. Beside the original configuration with the rotors located at $0.2969\frac{b}{2}$, five more positions were tested at $0.2578\frac{b}{2}$, $0.4141\frac{b}{2}$, $0.5312\frac{b}{2}$, $0.7656\frac{b}{2}$ and $0.8828\frac{b}{2}$. It should be noted that it is not possible to move the rotors much closer to the wing root as that results in them colliding with the fuselage.

The last parameter modified to infer on the aerodynamic interaction between the wings and rotors in horizontal flight was the rotor's orientation relative to the flow. All the simulations up to this point were performed with the rotor blades parallel to the flow, but, without any mechanism that fixes them in that position, they are free to move based on whichever aerodynamic loads are applied to them, specifically the torque around their axis of rotation. For this reason, an extra simulation was performed with the rotor blades perpendicular to the main flow direction. This way the torques on the rotors both aligned and perpendicular to the flow can be determined to assess if motion will occur, and, if such, what changes in the flow with them in that position.

4.1.2 Vertical Flight

The first step to comprehend vertical flow characteristics is to study the isolated rotors in hover and at different axial climb velocities. These values are later compared with those obtained from the full VTOL configuration in the corresponding flight phase. Hence, besides hover, the isolated rotor was simulated at climb speeds of $0.5m/s$, $1m/s$, $1.5m/s$, $2m/s$, $3m/s$ and $4m/s$ and its performance metrics were assessed.

Similarly to what was done in the previous subsection, the conventional configuration was simulated at the aforementioned axial climb speeds and the aerodynamic loads on the structure were obtained. By evaluating the performance parameters and flow behaviour of the isolated rotor and the isolated conventional UAV structure, one can set the baseline for future comparison with the full VTOL configuration. This way, the influence of the fuselage, tail and wings on the rotor performance can be determined, and conversely, the impact of the induced velocity by the rotors on the aerodynamic loads in the UAV structure can be evaluated.

With the baselines defined, the full VTOL configuration was simulated in hover and climbing at the prescribed climb velocities, and a full assessment of its performance carried out.

Finally, just like in horizontal flight, simulations were solved with the rotors placed at different positions to determine how it affects the UAV performance and check if there are more advantageous locations for the rotors. Besides the original position at $0.297\frac{b}{2}$, the chosen alternative locations were at $0,375\frac{b}{2}$, $0,453\frac{b}{2}$ and $0,531\frac{b}{2}$.

To keep the thrust constant as the UAV climbs at different velocities, specific angular velocities must be defined at the rotors. To determine the approximate angular velocities, data provided by the propeller manufacturer[29] was interpolated with the goal of maintaining an approximate thrust of $25N$ in each

rotor, at every climb speed. By producing this thrust, all the rotors add up to the UAV's MTOW. According to this, the rotor's angular velocity at a given climb speed is given in table 4.1.

Table 4.1: Rotor angular velocities at specified climb speeds.

Climb Velocity (m/s)	Hover	0.5	1.0	1.5	2.0	3.0	4.0
Angular Velocity (rad/s)	4580	4590	4600	4610	4620	4650	4680

4.1.3 Transition Flight

Transition flight represents the most complex phase in any VTOL aircraft's mission, since it is when the most aerodynamic mechanisms are at play and interact with each other. This means that the statements made at the end of subsection 2.2.2 need to be put into question, namely, the complexity of the interaction between stationary and moving zones.

One known mechanism in rotors with an horizontal velocity component is the occurrence of a reverse flow region at the root of the retracting blade relative to the flow direction. In that zone, due to the horizontal velocity, the flow travels from the trailing edge to the leading edge of the blade, resulting in a decrease in thrust. The reverse flow region is shown in figure 4.2.

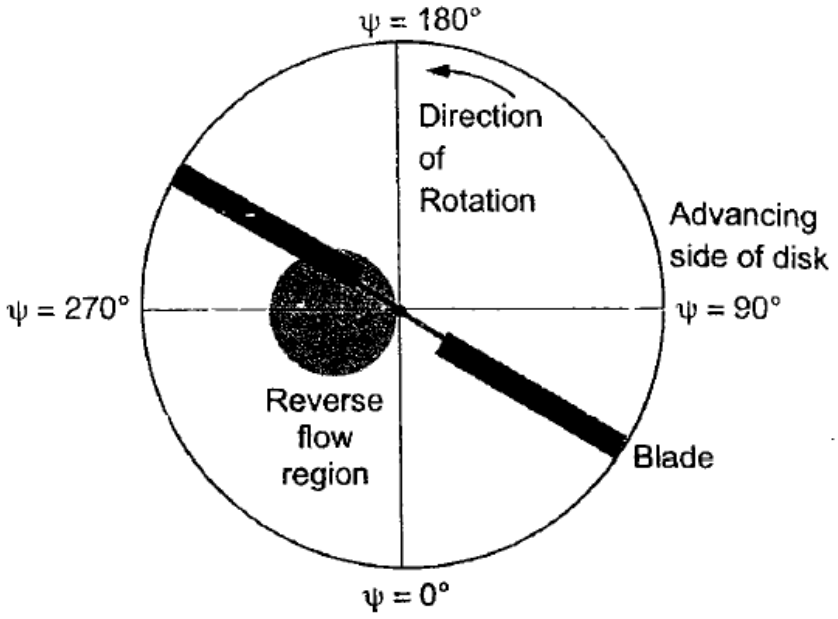

Figure 4.2: Rotor reverse flow region[28].

This once more confirms that the flow around rotating blades is fully unsteady and the induced velocities are highly dependent on the blade's azimuthal position. In order to still have some understanding of the main fluid structures, while keeping the simplicity and lower computational costs of the MRF method, the goal is to perform simulations at the two positions of interest described below, for each horizontal velocity.

By analysing figure 4.2 once again, it can be seen that when the rotor blades are parallel to the

flow, that is, one blade has the azimuthal angle of $\Psi = 0°$ and the other of $\Psi = 180°$, the horizontal velocity is perpendicular to the blade velocity, meaning that the advance velocity has no contribution to the velocity component perpendicular to the rotor blade, responsible for thrust. Thus, at these positions the flow velocity perpendicular to the blade at a given distance to the axis of rotation, r, is simply given by $U(r) = \Omega_R r$, where Ω_R is the rotor angular velocity.

Conversely, when the rotor blades are perpendicular to the flow, that is, for one blade $\Psi = 90°$ and for the other $\Psi = 270°$, the advance velocity is parallel to the blade velocity, resulting in them adding together. In the advancing blade, at $\Psi = 90°$, both velocities have the same direction meaning that they add up and the velocity perpendicular to the blade at a given distance to the axis of rotation is given by $U(r) = \Omega_R r + U_\infty$. On the other hand, the velocities in the retreating blade subtract, and the velocity is given by $U(r) = \Omega_R r - U_\infty$. This phenomenon results in an increase in thrust on the advancing blade and a decrease in the retreating blade.

All the other blade positions constitute ”in between” cases of the two described above, and so, in order to have an acceptable approximation of the aerodynamic coefficients and a qualitative description of the flow behaviour, simulations at both angles were performed fo the horizontal velocities of $10m/s$, $15m/s$, $20m/s$ and $30m/s$.

4.2 Results

All the simulations were run using a workstation equipped with an 8 Core Intel(R) Xeon(R) W-2245 CPU, clocked at 3.9GHz, with 256 GB of RAM. Simulations were run with 8 solver processes and without GPU acceleration, until convergence criteria were met, namely that the residuals lowered to, at least, 10^{-4}, despite that in some cases the turbulent kinetic energy only lowered below 10^{-2} and 10^{-3} in others. Moreover it was also verified that the variable monitors described at the end of subsection 3.1.3 converged to a value with negligible oscillations.

Horizontal flight simulations took between 300 and 400 iterations to converge, where the base configuration simulations took a number of iterations close to the lower boundary and the full geometry simulations took numbers closer to the upper boundaries. In terms of computational time, these simulations took between 3 hours and 5.5 hours, following the same trend as with the number of iterations.

Regarding vertical flight, the one composed of only the base geometry took approximately 200 iterations to converge, whereas simulations involving rotor motion took between 8000 and 10000 iterations to reach convergence. Due to the much higher number of iterations required to converge, these simulations took approximately 12 hours each. The initial test simulations utilized to assess the suitability of the Sliding Mesh and the Overset Mesh models took approximately 24h to simulate half a rotation using the described hardware setup. Given the fact that multiple rotations are required to guarantee that the rotor is working at constant conditions, the time it would take to obtain the results is too big to be used during the UAV design phase and the employment of these techniques should be left for the validation of a given design before proceeding with prototyping.

Finally, transition flight simulations required about the same number of iterations to converge as in

vertical flight, but due to the higher number of elements and more complex flow, each simulation took approximately 16 hours of computational time.

4.2.1 Horizontal Flight

Before inferring on the aerodynamic interaction between the different components, one should first evaluate the aerodynamic characteristics of the base geometry. To start off, the statements made in the previous section about the occurrence of flow separation near the wing root are justified.

In figure 4.3, a contour plot of the wall shear stress component in the direction aligned with the flow, along the wing top surface is displayed. With this metric, one can identify flow separation, since a sign change in wall shear stress in the flow direction is directly caused by a direction change in the velocity itself. Air flows in the negative Z direction, thus the Z component of wall shear stress should also be negative, with the occurrence of positive stresses representing flow reversals. The Leading Edge and the Trailing Edge are identified by LE and TE, respectively.

Hence, wall shear stress is plotted such that dark blue coloured surfaces correspond to zero or negative stresses, whereas differently coloured patches correspond to a positive stress. It can be seen in the wing without fillet that a positive stress zone occurs, therefore there is separation, whereas in the geometry with the fillet it no longer occurs.

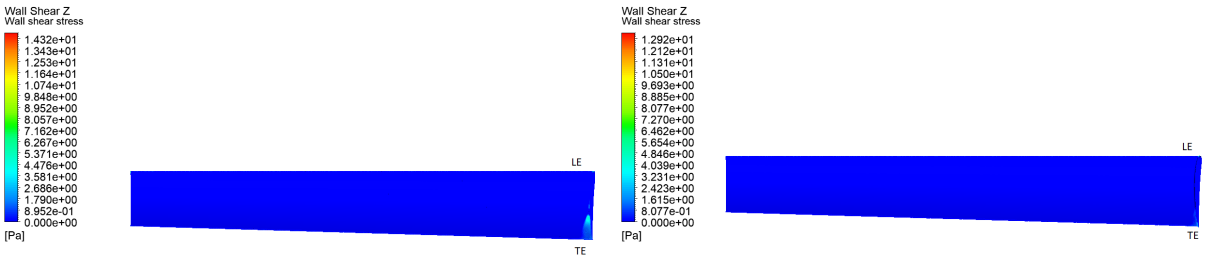

(a) Wing root without fillet.

(b) Wing root with fillet.

Figure 4.3: Wall Shear Stress magnitude in the Z direction along the wing's suction side.

With the aforementioned correction, the base configuration aerodynamic coefficients in horizontal flight are presented in table 4.2, namely the lift coefficient, C_L, drag coefficient, C_D, and the lift-to-drag ratio, $\frac{C_L}{C_D}$, which is commonly used as a metric to evaluate aircraft performance and its range.

Table 4.2: Base configuration aerodynamic coefficients.

C_L	C_D	$\frac{C_L}{C_D}$
0.164974	0.0157815	10.45

Figure 4.4 shows flow streamlines crossing the fuselage and wings. These streamlines present a typical behaviour, having a small deflection near the wings, whereas a big deflection is visible on the

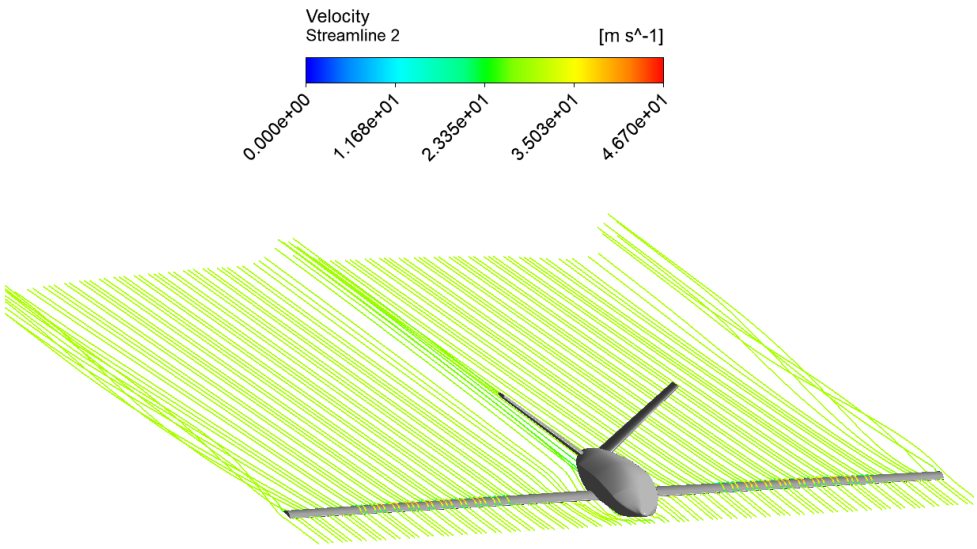

Figure 4.4: Streamlines flowing over base configuration's fuselage and wings.

fuselage wake. Also the formation of wing tip vortices can be identified, which in this case can be seen to have a strong magnitude due to the absence of wing tip devices like sharklets or winglets.

In order to obtain a better grasp on how the wakes develop along the UAV geometry, figure 4.5 displays streamwise vorticity contours in the wake of the aircraft. In this figure, vortices can be observed forming in the wing tip, fuselage and tail, which as they get carried in the wake get progressively bigger and more diffused, until they start disappearing, as would be expected.

As a last general metric describing flow behaviour, figure 4.6 shows the pressure coefficient, C_p, distribution over the full UAV surface.

As expected, higher pressures, in red, are visible in the aircraft's nose and the wing and tail's leading edges, where C_p reaches a value of 1 at stagnation points. Besides these areas, high pressure zones can also be identified in the upwind faces of the compartments for cameras and sensors, located underneath the fuselage, due to their blunt geometry.

Conversely, the darker shades of green and blue identify low pressure zones, the most notable one being the wing suction side, even though the lowest pressure is observed in the suction peak slightly below the wing's stagnation line. Further reasoning is provided for this later in this work.

A local inspection is presented in figure 4.7 where the wing pressure coefficient is plotted against the non-dimensionalized chord at two stations, located at 29.69% and 76.56% of the wing semi-span, respectively. By observing these plots, one concludes that the obtained distribution does not follow a typical behaviour, mainly due to the pressure distribution on the upper and lower sides of the wing, which intersect slightly aft 15% of the chord. To better understand the reasoning behind this, figures 4.8 and 4.9 containing pressure and velocity contours, respectively, at a section located at $76.56\frac{b}{2}$, are introduced.

As previously mentioned, it can be seen in figure 4.8 that a stagnation point, marked by $C_p \approx 1$, is

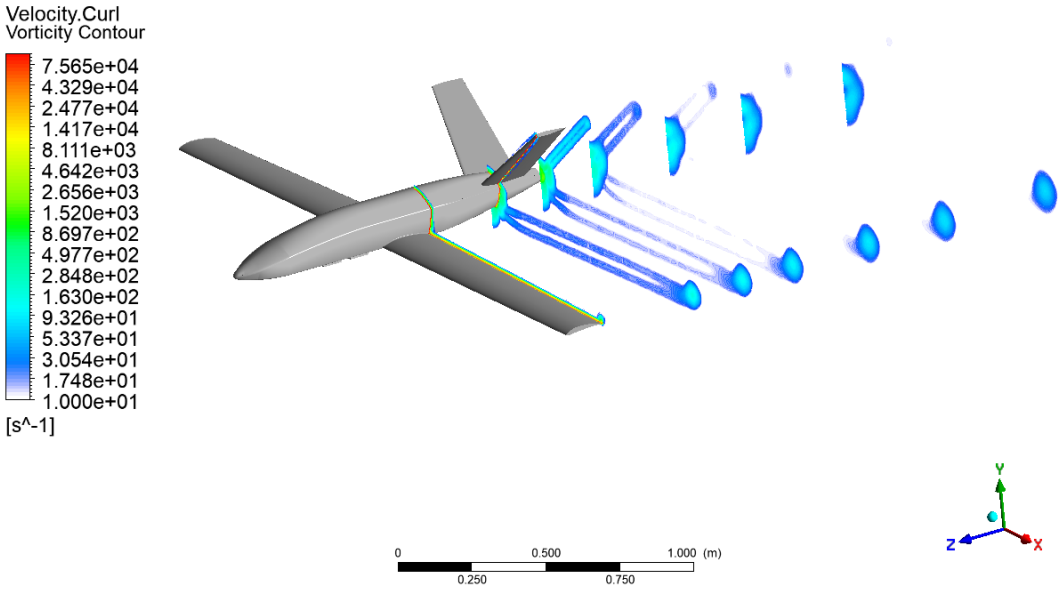

Figure 4.5: Visualization of the base configuration's streamwise vorticity contours.

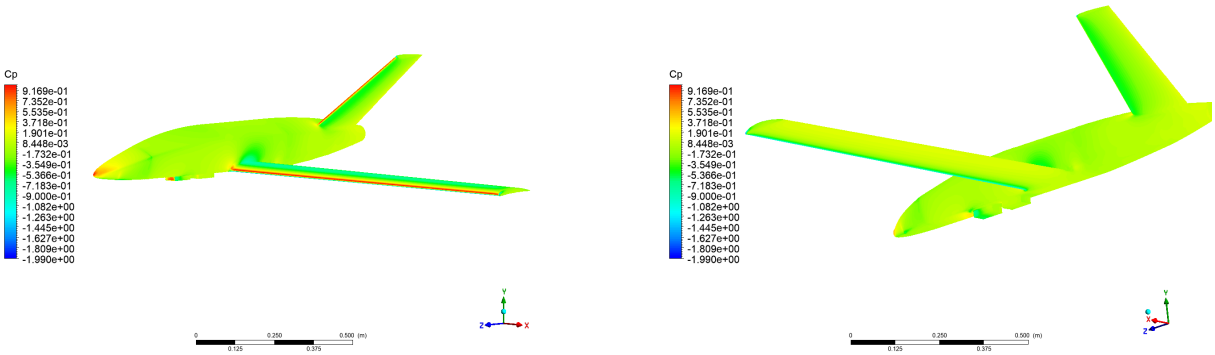

(a) View 1 (b) View 2

Figure 4.6: Visualization of pressure contours on the UAV surface from different views.

present, located slightly on the upper side of the wing, followed by a large zone of negative C_p identified by the light blue colour. In turn, below it, a suction peak is present, marked by a small zone of high negative values of C_p, which is followed by a zone of low positive pressures, denoted by the light green, close to yellow, colours.

To justify this, one can look at the velocity contours in figure 4.8 and conclude that, as expected, a stagnation point is present in the zone where $C_p = 1$ and $U \approx 0$. By following the flow moving above it, one sees the flow accelerating in a zone with relatively low curvature, resulting in a decrease in pressure, up to approximately half the chord, then the flow decelerates slowly once again, increasing pressure until the trailing edge is met. On the other hand, by following the flow below the stagnation point,

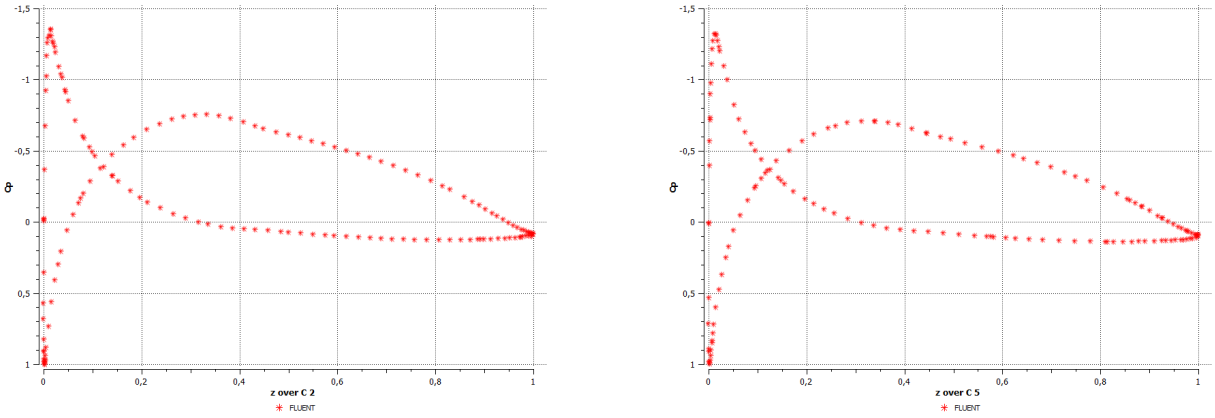

(a) 29.69% of the semi-span

(b) 76.56% of the semi-span

Figure 4.7: Pressure coefficient distribution at different span positions.

one sees a rapid acceleration along the highly curved surface near the leading edge, which results in an accentuated low pressure, followed by the flow decelerating to accompany the surface curvature. Initially this deceleration is stronger, and starts decreasing, up to the point near half the chord where velocity becomes almost constant. The resulting behaviour on pressure is that it steeply increases at the beginning and then starts to level out as velocity also does so.

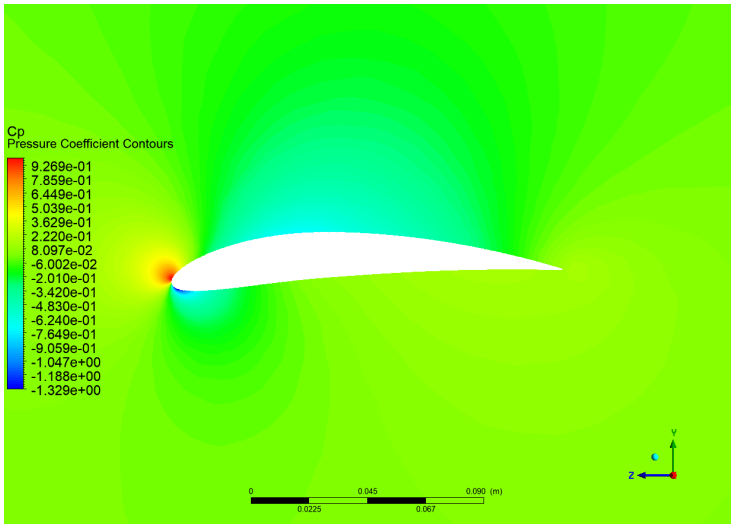

Figure 4.8: Visualization of pressure contours at 76.56% of the wing semi-span.

One can see that the description above same as what is happening in the C_p plots in figure 4.8 and that it strongly dependant on the wing curvature. When looking at the wing profile, it is visible that the chord line connecting the leading and trailing edge is at a negative angle respective to the flow, resulting in the flow going through a higher curvature in the lower side of the wing. Were the wing to be positioned on a higher angle of attack, the flow would have to experience a higher curvature in the upper side of the wing, moving the suction peak above the stagnation point. In fact, for the current UAV at an angle of attack of $10°$, the C_p plot is given by figure 4.10, which depicts a more typical behaviour.

Once the baseline for the aerodynamic coefficients and flow structures is set, one can proceed to evaluate the VTOL aerodynamics in conventional flight. Table 4.3 presents values of C_L and C_D in

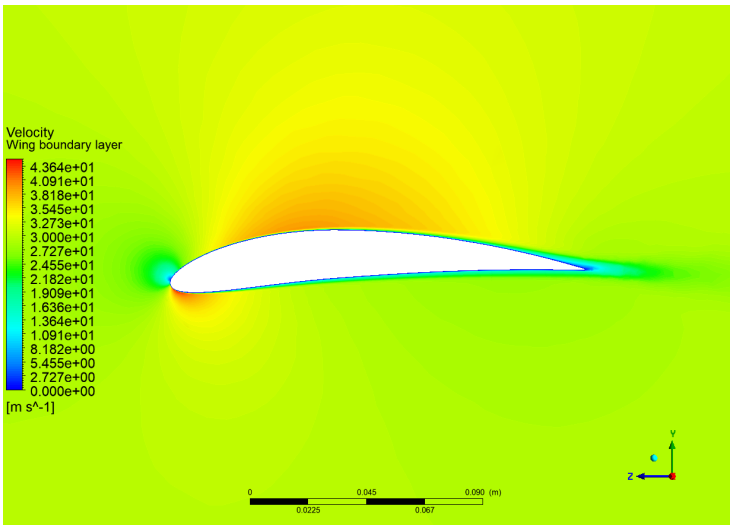

Figure 4.9: Visualization of velocity contours at 76.56% of the wing semi-span.

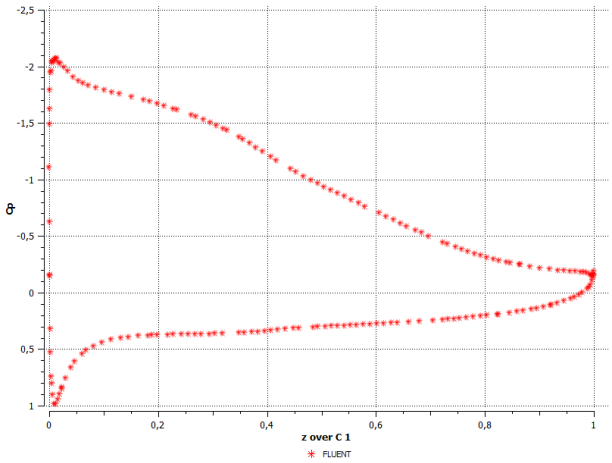

Figure 4.10: Pressure coefficient distribution at 76.56% of the semi-span, with an angle of attack of $\alpha = 10°$.

each component of the beVTOne UAV, and the respective values, if applicable, in the conventional configuration. The coefficients are non-dimensionalized with the wing area and free stream velocity.

Table 4.3: Comparison of aerodynamic coefficients between conventional and SLT configurations in cruise flight.

	Fuselage		Rotor (Front)		Rotor (Rear)		Rotor Boom		Tail		Wing	
	C_L	C_D	C_L	C_D	C_L	C_D	C_L	C_D	C_L	C_D	C_L	C_D
Base Configuration	0.009102	0.004873	-	-	-	-	-	-	-0.00375	0.001546	0.162483	0.009362
VTOL Configuration	0.009013	0.004869	0.003035	0.000895	0.00227	0.00067	-0.0045	0.005244	-0.00366	0.001549	0.159172	0.009457
Variation (%)	-0.9796	-0.08137							-0.5196	0.1514	-2.038	1.014

The total values of C_L and C_D of the SLT configuration in cruise flight are of 0.16525 and $0,022683$, respectively, which correspond to a negligible variation in total lift of 0.17% and a considerable increase of 43.73% in total drag. The bigger increase in drag is easily justifiable by the introduction of new structures that, due to their functions, are not aerodynamically optimized in horizontal flight, and as such generate wakes which contribute greatly to drag.

Despite the small variations of about -2% in C_L and 1% C_D, on the wing, it is the component which

is more affected by the VTOL structures, as would be expected, since the wing is directly located in the wake of the front rotor. Figure 4.11 shows streamlines flowing over the front rotors, wings and fuselage, as previously done with the base configuration.

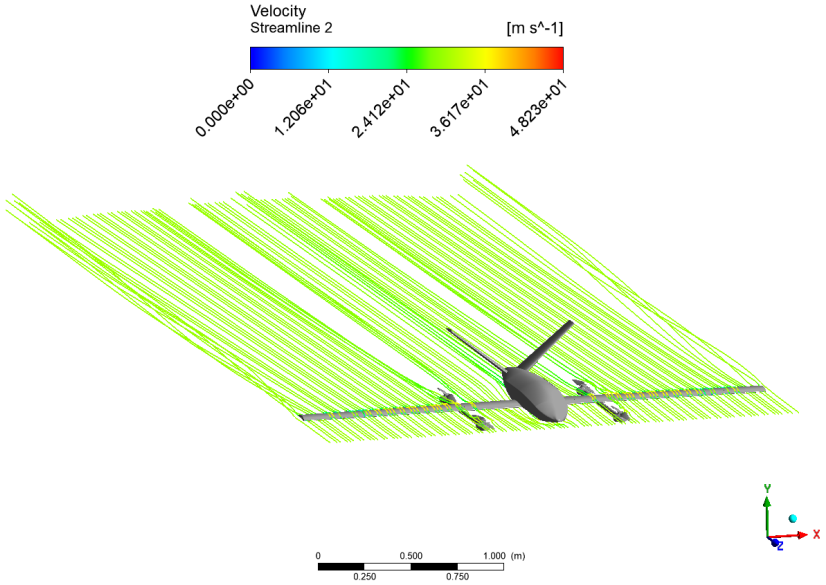

Figure 4.11: Streamlines flowing over rotors, wings and fuselage of the VTOL configuration.

Similar flow structures as those found in the base configurations are identified, and a new wake behind the rotors is present, which diverts streamlines away from it. A better visualization of this wake can be obtained resorting to figure 4.12, where, once more, the streamwise vorticity contours are displayed.

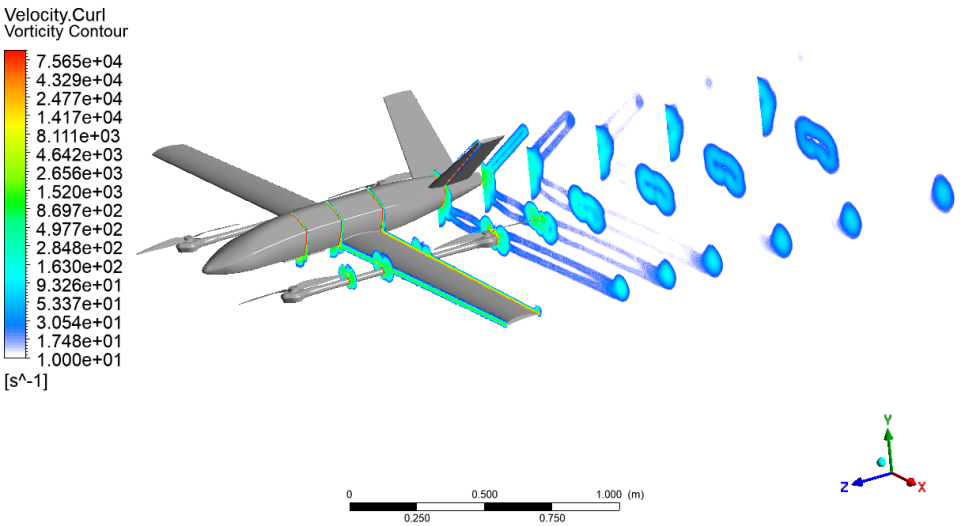

Figure 4.12: Visualization of the VTOL configuration's streamwise vorticity contours.

The vortices generated by the rotors are clearly identifiable, even displaying a higher intensity and

bigger size than the wing tip vortices. An important consequence of this is the front rotor wake vortex impinging on the wing behind it. This vortical, lower speed, flow interacts differently with the wings, resulting in the decrease in lift and increase in drag previously observed. The air located in this wake, after having lost momentum going through the front rotor and the wing, comes into contact with the rear rotor, but, due to its lower energy, the aerodynamic loads generated there are lower than those in the front rotor.

The resulting pressure distribution over the wings is shown in figure 4.13.

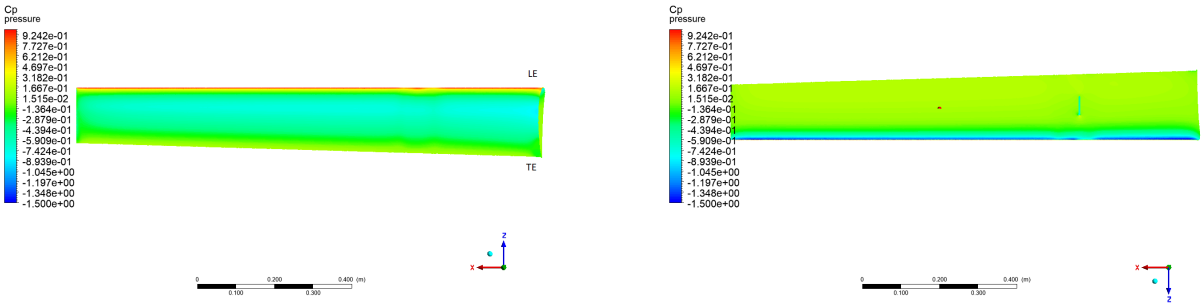

(a) Wing suction side

(b) Wing pressure side

Figure 4.13: Pressure coefficient contour plot over the wing of the VTOL configuration in cruise flight.

It is noticeable that the pressure and suction peaks are dimmer, resulting in lower forces being generated in that zone of the wing. It is also visible that the suction zone along the wing suction side is slightly narrower. This behaviour is clearly visible in the C_p plot, overlapping data from the VTOL, in blue and conventional, in red, configurations in figure 4.14 a), combined with the pressure contour plot shown in figure 4.14 b), located in the plane of the rotors.

Comparing the pressure distributions, it can be seen that the peaks only reach values of approximately 0.75 and -1 of maximum and minimum pressure coefficients, respectively, as opposed to the values of approximately 1 and -1.4 obtained in the conventional configuration. Also, the previously mentioned narrower suction zone in the wing's upper side is confirmed to be less intense. The gap present in the wing's pressure side is caused by the connection between the wing and the boom. The increase in pressure before said connection and the drop right after it occur due to the flow coming to a stop when coming in contact with it, and the small wake left behind it, respectively.

According to the procedures described in the previous section, this analysis process was repeated with the rotors located at $0.2969\frac{b}{2}$, $0.2578\frac{b}{2}$, $0.4141\frac{b}{2}$, $0.5312\frac{b}{2}$, $0.7656\frac{b}{2}$ and $0.8828\frac{b}{2}$, in order to assess if the rotor could be interacting in some way with the fuselage, and if changing its location would alter the aerodynamic loads on the wing. Across the six positions, the flow presented the same characteristics as described above.

Figure 4.15 shows the wing section's two-dimensional lift coefficient, C_l, distribution across the wing semi-span at each of the rotor positions. As expected, due to three-dimensional effects, lift is maximized near the wing root and decreases as it gets closer to the tip, where it reaches a value of zero. Moreover, these results show that the C_l curve corresponding to a given rotor position displays a dip in C_l at the

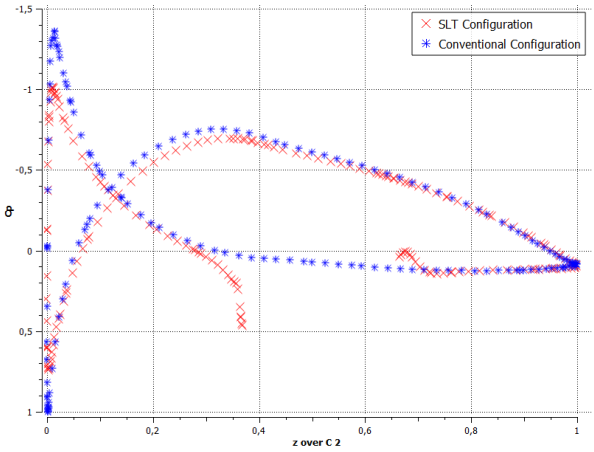

(a) Pressure coefficient comparison between the VTOL and conventional configurations.

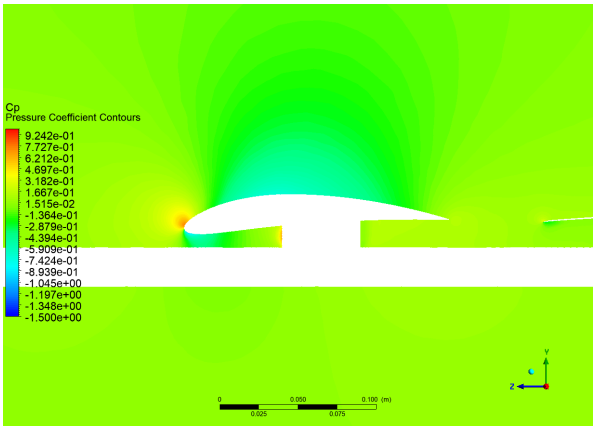

(b) Pressure coefficient contours at the rotor plane.

Figure 4.14: Pressure coefficient plot (left) and pressure coefficient contour plot (right).

rotor location with a width comparable to that of the impinging vortex identified in figure 4.12.

A common characteristic found across all the curves, including that of the conventional configuration, is that a considerable decrease in C_l is present near the wing root, due to the flow interaction between the fuselage and wing.

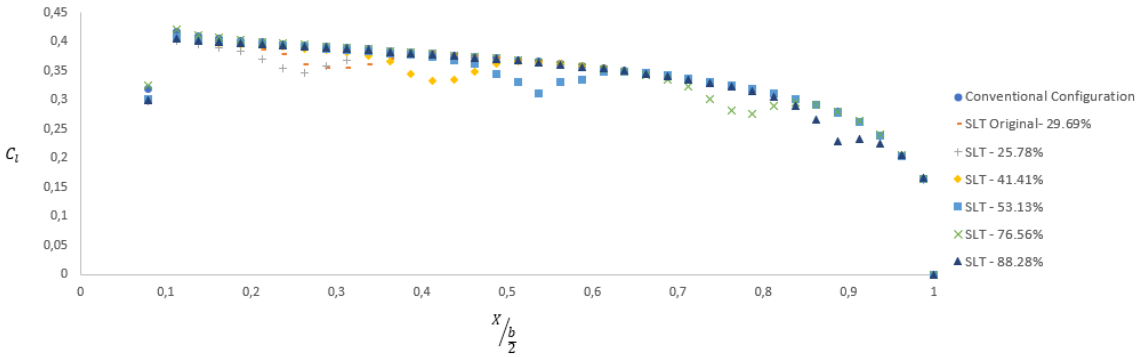

Figure 4.15: Two-dimensional lift coefficient distribution along wing semi-span.

A similar plot is created, representing the wing section's two-dimensional drag coefficient, C_d, along the wing semi-span, shown in figure 4.16. This time, the change in C_d along the wing is not as clear as with the C_l distribution where a simple dip could be identified, however, by closely examining the curve, one concludes that the relative variation in drag introduced by the rotor presence, when compared to the conventional configuration, is similar, no matter the rotor's position. That is, it can be seen that, while examining the curve moving from wing root to tip, the rotor wake induces an initial small spike in drag, followed by a small dip. Then, a big crest is visible, being succeeded by a big through. After that, the drag levels out to the values of the conventional configuration. The similar behaviour, independent of the rotor position, indicates that it is the same flow structure that is inducing these changes, namely the small variations in the vertical component of the flow velocity due to the rotor vortices, which are not symmetric, since the rotor blades have opposing incidences.

Outside the rotor's zone of influence, it is verified, once more, that the drag distribution is the same

as in the conventional configuration, being lowest away from the wing extremities, where drag increases due to contribution from interference drag caused by the presence of the fuselage, near the wing root, and the contribution of induced drag caused by wing tip vortices, near the wing tip.

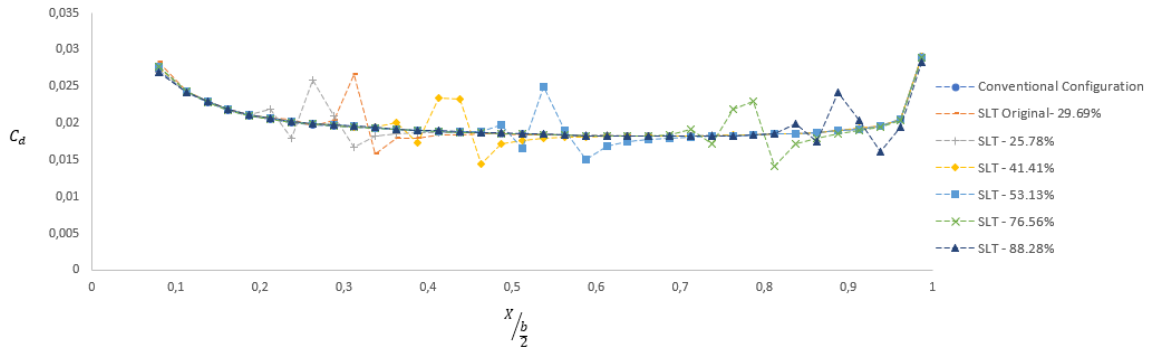

Figure 4.16: Two-dimensional drag coefficient distribution along wing semi-span.

The quantitative impact on the wing's lift and drag is available in table 4.4. From these results it could be assumed that, despite the marginal changes in C_L and C_D, it would be best to locate the rotors at approximately 75% of the wing semi-span, however, when evaluating this implementation with a multidisciplinary design approach, one notices that by moving from the original position at approximately 30% of the semi-span to the suggested position, the bending moment on the wing root, which is located at approximately 6% of the semi-span, would increase 2.875 times, which could require structural reinforcement at the wing root, increasing the UAV weight.

Table 4.4: Wing aerodynamic coefficient variation with multiple rotor positions.

Rotor Position: (% of $\frac{b}{2}$)	Wing C_L	Variation (%)	Wing C_D	Variation (%)
Conventional	0.162483	-	0.009362	-
25.78	0.158872	-2.22	0.009431	0.743
29.69	0.159171	-2.04	0.009457	1.014
41.41	0.158819	-2.25	0.009442	0.851
53.12	0.158815	-2.26	0.009415	0.566
76.56	0.160604	-1.16	0.009399	0.397
88.28	0.159384	-1.91	0.009417	0.587

From this study it is thus concluded that, despite the rotor position along the wing affecting the UAV aerodynamic coefficients in cruise flight, its actual impact is marginal, and so, should other performance parameters yield more benefits from having the rotors located at a different position, then that parameter should be prioritized. Examples of such parameters are the previously mentioned wing's structural requirements or eventual aerodynamic performance gains in other flight phases.

The last step to evaluate horizontal flight is examining the impact of rotor orientation in flight performance, as described by the procedures in subsection 4.1.1. Starting by examining the streamlines displayed in figure 4.17 it is noticeable that much bigger vortices are on the wake of the rotors when compared to those identified in figure 4.11. In fact, this is confirmed by observing figure 4.18, where it is visible that the biggest and more intense vortices are located on the wake of both rotors. Analysis of

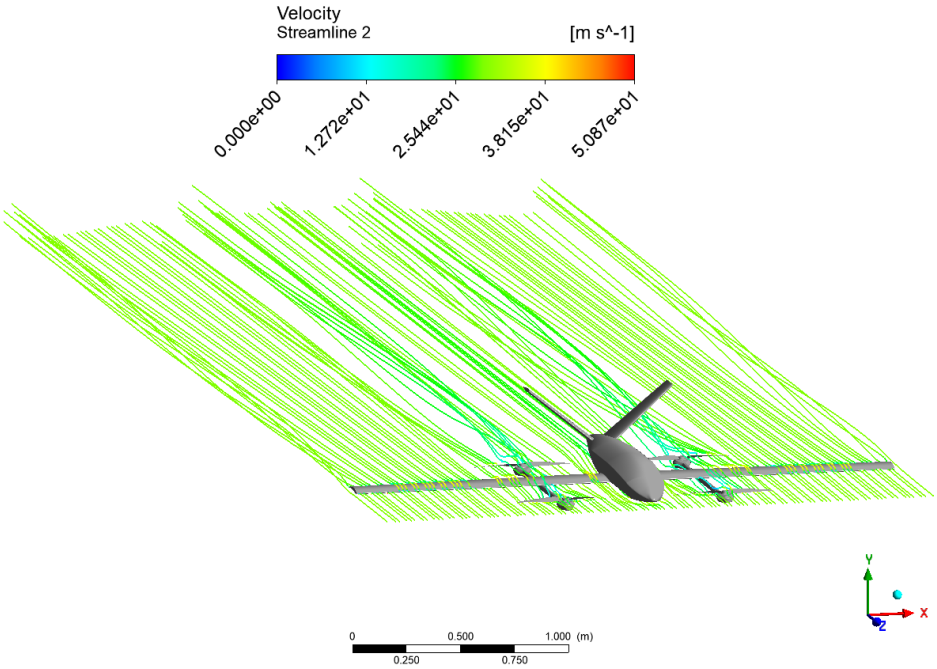

Figure 4.17: Streamlines flowing over rotors, wings and fuselage of the VTOL configuration with rotors perpendicular to the flow.

both figures alone hints that the rotors will be responsible for a high contribution to drag, and that the wake of the front rotor will have an impact on a fair length of the wing.

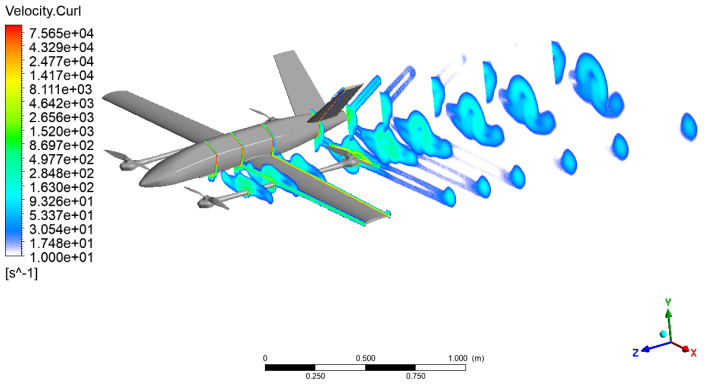

Figure 4.18: Visualization of the VTOL configuration's streamwise vorticity contours with the rotors perpendicular to the main flow.

To better understand how the wake generated by the front rotor impinges on the wing, figure 4.19 displays the velocity fields and some streamlines that pass through the front rotor, succeeded by the wing, located in two planes, one in the middle of the blade that is closest to the fuselage, and the other in the middle of the blade that is furthest to the fuselage.

Analysis of the streamlines shows that the flow meets the blade closer to the fuselage with a positive

angle of attack. This blade acts as a wing, deflecting the flow downwards and thus creating downwash. As a consequence of this, the flow reaches the wing at a lower angle of attack and thus the wing section behind said blade should produce less lift.

On the other hand, the air that flows through the blade located away from the fuselage reaches it at a high negative incidence and is, therefore, deflected upwards. This flow, with slight upward velocity, reaches the wing with an increased angle of attack, resulting in higher lift generation behind this blade.

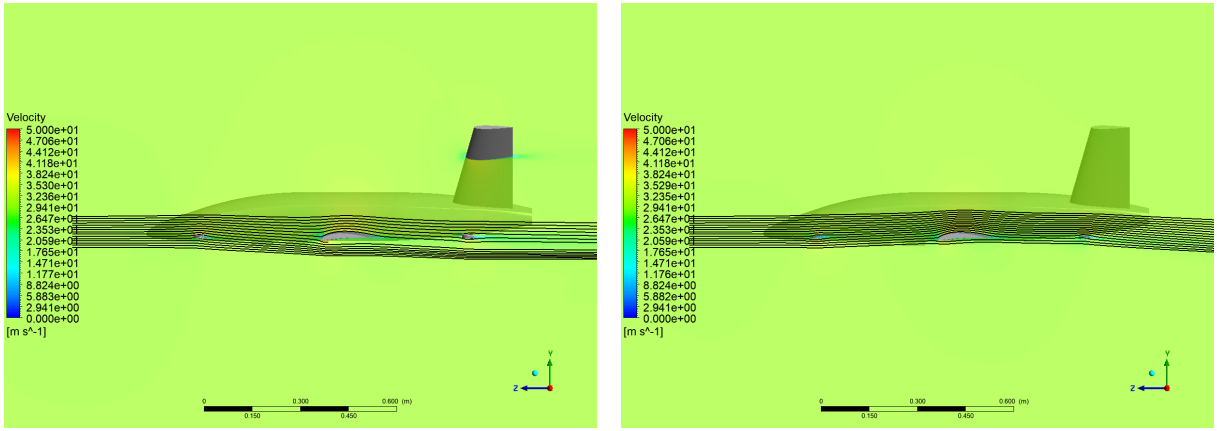

(a) 17.97% of the wing semi-span.

(b) 41.41% of the wing semi-span.

Figure 4.19: Velocity field visualization in two planes located in the middle of each rotor blade.

Such behaviour is corroborated by figure 4.20. In figure 4.20 a) one can identify the stronger suction peak present on the wing's lower side, followed by lower pressures on the same side, when compared to the C_p distribution in the conventional configuration. On the suction side it is also visible that throughout the whole top surface suction isn't as strong. These factors combined result in a lower lift force compared to the conventional configuration.

Conversely, in figure 4.20 b), the opposite is identified. Lower pressures are present on the upper side of the wing, while higher pressures are present at the lower side, resulting in a lift increase.

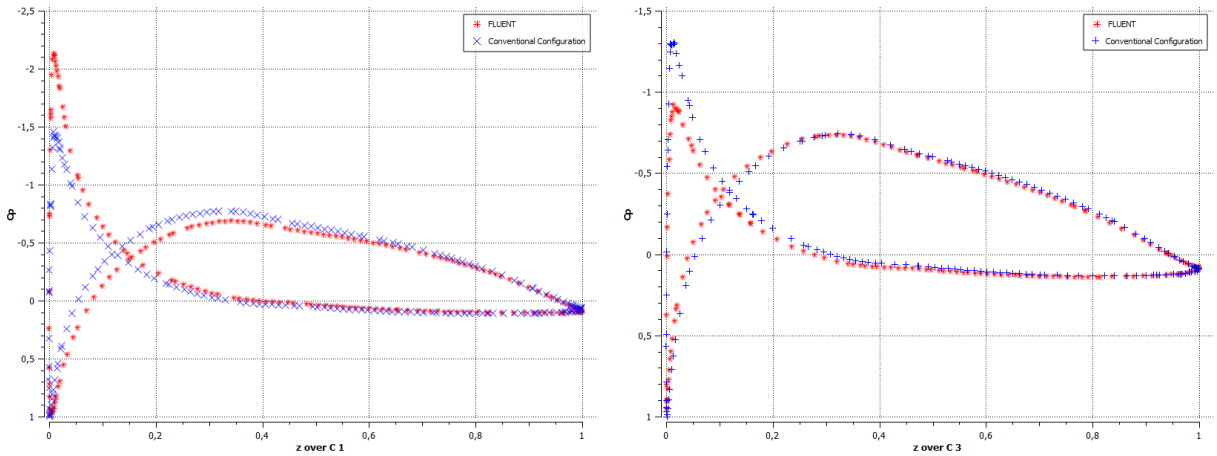

(a) Advancing blade plane.

(b) Retreating blade plane.

Figure 4.20: Pressure coefficient distribution in planes located in the middle of the advancing blade (left), and in the middle of the retreating blade (right).

The C_l distribution along the wing shown in figure 4.21 confirms the predictions made by analysing

the previous figures, specifically the zones with low and high C_l, however, with this data one can see that the through in C_l is much stronger than the peak, resulting in an overall decrease in lift. Just like before, away from the rotor wake, lift returns to the values yielded by the conventional configuration.

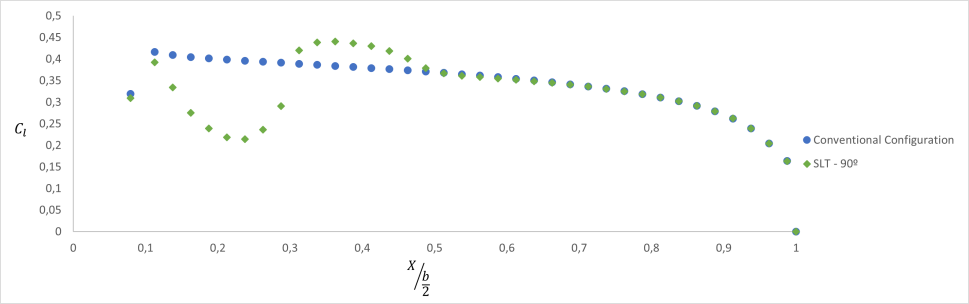

Figure 4.21: Two-dimensional lift coefficient distribution comparison between conventional configuration and VTOL configuration with rotors perpendicular to the flow.

A similar plot is presented for C_d, in figure 4.22, where it is shown that in the approximate region where lift has a big dip, drag has a slight peak, whereas in the approximate zone where lift has a small increase, drag has a considerable decrease.

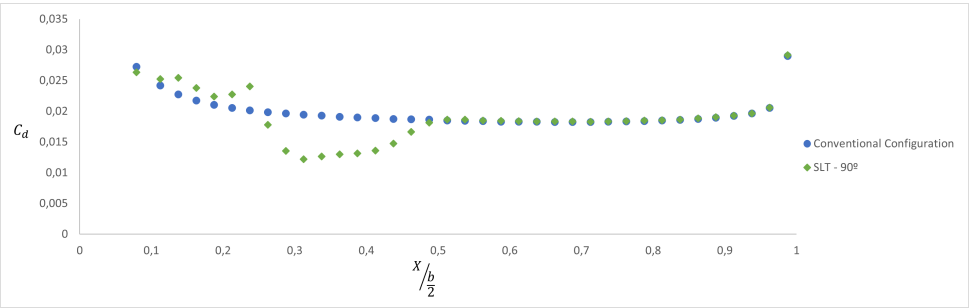

Figure 4.22: Two-dimensional drag coefficient distribution comparison between conventional configuration and VTOL configuration with rotors perpendicular to the flow.

From these graphics, it is thus expected that the wing produces less lift but also less drag. All the aerodynamic loads, separated by component are presented in table 4.5.

Table 4.5: Comparison of aerodynamic coefficients between conventional and SLT configurations with, with rotors at $90°$, in cruise flight.

	Fuselage		Rotor (Front)		Rotor (Rear)		Rotor Boom		Tail		Wing	
	C_L	C_D	C_L	C_D	C_L	C_D	C_L	C_D	C_L	C_D	C_L	C_D
Base Configuration	0.009102	0.004873	-	-	-	-	-	-	-0.003750	0.001546	0.1625	0.009362
VTOL Configuration	0.009050	0.004847	0.009933	0.008726	0.008232	-0.007670	-0.007170	0.008509	-0.0025374	0.001652	0.1534	0.008998
Variation (%)	-0.5757	-0.5394							-32.34	6.851	-5.554	-3.885

When analysing these results, the loads on two components come to attention, those on the tail and the wing. Regarding the tail, no apparent flow structure justifies such a change in C_L and C_D, since it is not located directly on the wake of the rotors, and their position was the only parameter that was changed. An hypothesis for this behaviour is presented as follows: On the conventional configuration the streamlines that feed the tail are first deflected by the fuselage, going slightly upwards during the first half, and then downwards during the second half, arriving at the tail with negative angle of attack, resulting

on the negative C_L that is observed. On the other hand, when the rotor blades are perpendicular to the flow, the wake, even though it does not impinge on the tail, it interacts with the streamlines going over the fuselage, and when they pass the middle part of the fuselage they cannot deflect as much due to the wake, arriving at the tail with a less negative angle of attack, resulting on a less negative C_L.

Regarding the wing, as predicted, both the lift and drag show a palpable reduction when compared to the conventional configuration. When comparing with the SLT configuration having the rotor blades aligned with the flow, one sees that, when the blades are aligned, the flow has a lesser influence on the wing forces, than when the blades are perpendicular, as expected, since the generated wake is smaller. The reduction in drag on the wing is immediately compensated by the high values of drag produced by the VTOL structures.

In fact, this configuration shows a total C_L of 0.17097 and total C_D of 0.025059, which compared to the conventional configuration values represents a 1.87% higher C_L and 58.8% higher C_D. The increase in C_L comes from the rotor blades generating lift, however, the drag penalty is far too great for this to be a suitable rotor orientation. Furthermore, the lift-to-drag ratio, obtained from having the rotors aligned with the flow is 7.28, whereas with the rotors perpendicular to the flow it is 6.82, proving that this configuration is less efficient.

As briefly hinted at the end of subsection 4.1.1, if no mechanism is present to hold the blades in place, then they will rotate based on the aerodynamic loads acting on them. The torque applied on each rotor blade about its axis of revolution are presented in table 4.6, at both the studied simulations. No conclusions are taken based on the absolute values, but, by evaluating the signs, and consequently the sense of the torque being applied, one can infer on the direction of rotation of the rotors if left freely.

No absolute conclusions can be made regarding the rotating motion without further studies, with the blades at different orientations, since it is possible that, at some point, a direction inversion on the torque occurs, which can invert the rotation direction. However, one can predict that, due to the fact that the rotors are anti-symmetric, a blade located on one side of the vertical plane parallel to the flow should produce a different value of drag compared to the blade located at the opposite side of that plane, thus generating a moment around the axis of rotation. The generated torque should have constant direction since, in one side of the plane, the flow always interacts with the blade at a positive incidence angle, and in the other at a negative incidence angle. A common example of this behaviour occurs on the windmill-like structures placed on top of chimneys, which rotate with the wind in order to keep birds from nesting there.

It is thus expected that without locking mechanisms, the rotors will rotate with constant directions and the loads will oscillate approximately between those obtained with the rotor parallel to the flow and those with the rotor perpendicular to it, with eventual transient effects being present. Having the rotors parallel to the flow should constitute the best case scenario, since that is when the rotors have the lowest frontal area in regards to the flow, and having the blades perpendicular to the flow should be the worst case scenario since that is when the frontal area is maximized. From this, one concludes that for a better aerodynamic performance in horizontal flight, the rotor blades should be locked parallel to the flow.

Moreover, in order to decrease the performance penalty during cruise flight due to VTOL compo-

Table 4.6: Torque around rotors' axes of rotation at different orientations.

	Torque (Nm)	
	Parallel	Perpendicular
Front Rotor	-0.013033	-0.011994
Rear Rotor	0.0098582	0.0268020

nents, other strategies can be implemented other than changing the rotor position and/or orientation. Sawhee in [32] conducted wind tunnel tests on various vertically positioned rotors in horizontal flight and concluded, as expected, that smaller rotors, with lower pitches generate less drag. Furthermore, the authors concluded that, for a given rotor, there is a value of forward velocity in which an optimum drag is obtained. Given the fact that cruise velocity is usually a design requirement, attention should pe put into selecting a rotor whose optimum forward velocity is close to the UAV cruise velocity, between a set of pre-selected rotors that satisfy the primary vertical flight requirements, as that is the main purpose of those structures.

Another method would be the employment of folding mechanisms which reduce the rotors wetted area, but such systems increase the system's complexity and can have a big impact on weight.

4.2.2 Vertical Flight

As described in subsection 4.1.2, the rotor was simulated at hover and other prescribed axial velocities. The isolated rotor metrics, namely the thrust and power coefficients are displayed in table 4.7, together with the expected theoretical value and the relative error.

One important aspect to notice is that in conventional rotorcraft, like helicopters, the blade rotation speed is kept constant, and thrust is controlled by varying the blade pitch angle, through complex hub mechanisms. However, small, electric, multicopters commonly utilize fixed pitch rotor blades and thrust is controlled by varying the rotation speed. Therefore, the constants utilized in equations (3.7) and (3.8) to non-dimensionalize thrust and power are different in each axial and rotating speed, meaning that these coefficients cannot be directly compared with one another.

Table 4.7: Numerical results of rotor performance coefficients and comparison with the exact values.

Axial Velocity (m/s)	C_T			C_PW		
	Exact	Numerical	Error (%)	Exact	Numerical	Error (%)
Hover	0,010341	0,010052	-2,797	0,001426	0,001264	-11,36
0.5	0.010296	0.010181	-1.120	0.001414	0.001239	-12.36
1.0	0.010251	0.010130	-1.181	0.001401	0.001235	-11.81
1.5	0.010207	0.010074	-1.297	0.001389	0.001250	-10.00
2.0	0.010163	0.010024	-1.361	0.001376	0.001228	-10.76
3.0	0.010032	0.0098388	-1.925	0.001354	0.001216	-10.20
4.0	0.009904	0.0096679	-2.381	0.001330	0.001202	-9.638

Similarly to what was concluded in section 3.2, the numerical results for the thrust coefficient are very close to the estimated values interpolated form the manufacturer's performance sheets, justifying

once more the suitability of the MRF method to model rotor behaviour. However the model appears to underestimate the torque produced on the blades, which is indirectly represented by the values of C_{PW} on the table above. If one requires more accurate results regarding these parameters, then further studies should be performed to verify if more appropriate turbulence models are available for the specific application and if further mesh refinements can yield better results.

Regarding the flow structures, they too present a similar behaviour to that described in section 3.2, with differences occurring on the magnitudes of quantities like pressure and velocity. This is illustrated in figure 4.23 where the velocity field is shown in the rotor mid plane, through contours and vectors, and it can be seen that the main change in the flow is that the small zone near the rotor edge with ascending flow is no longer visible.

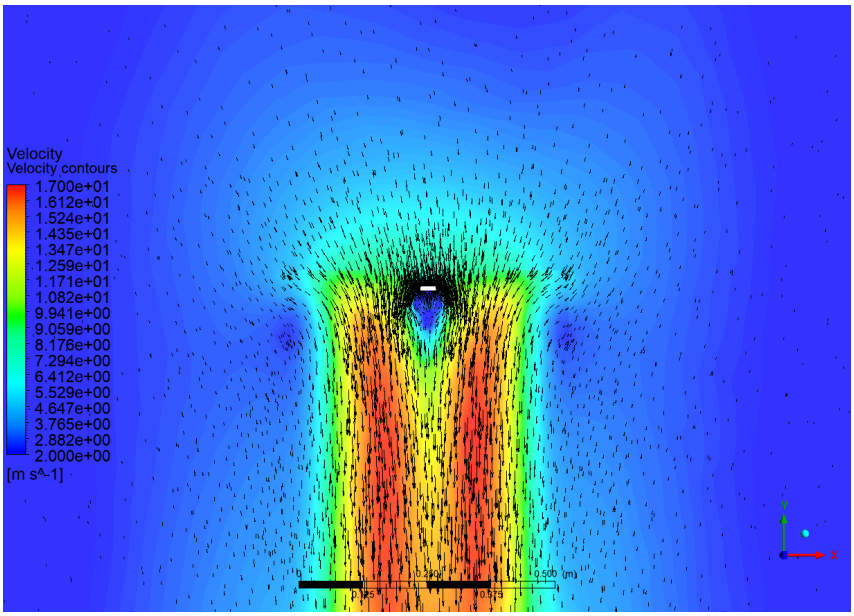

Figure 4.23: Visualization of the velocity field at the rotor mid plane in axial climb at 2m/s

Before proceeding to the study of the full VTOL configuration, the baseline loads on the fuselage, wings and tail were obtained. Figure 4.24 displays the pressure distribution over the UAV surface at a climb speeds of $0.5m/s$ and $4m/s$. Even though the magnitude of the change in pressure is small, it is evident that the whole top side of the UAV is under positive gauge pressure, whereas the bottom side is under negative gauge pressure. This differential generates a download on the UAV structure which must be balanced by the rotors. It is also noticeable that as the climb velocity increases, so does the pressure magnitude, as it is visible by the increase of maximum pressure in two orders of magnitude, resulting in higher downloads.

In figure 4.25 two-dimensional streamlines can be visualized across four different planes, at the minimum and maximum studied climb speeds, respectively. The streamlines show a straightforward behaviour, showing big deflections due to the presence of the fuselage, wing and tail. Below these structures, big gaps can be identified, which correspond to recirculation zones caused by the flow separating from the UAV surface. An interesting case is that of the wake located below the tail, since that structure is above a section of the rear rotor disk. There, it can be seen that the increase in axial velocity

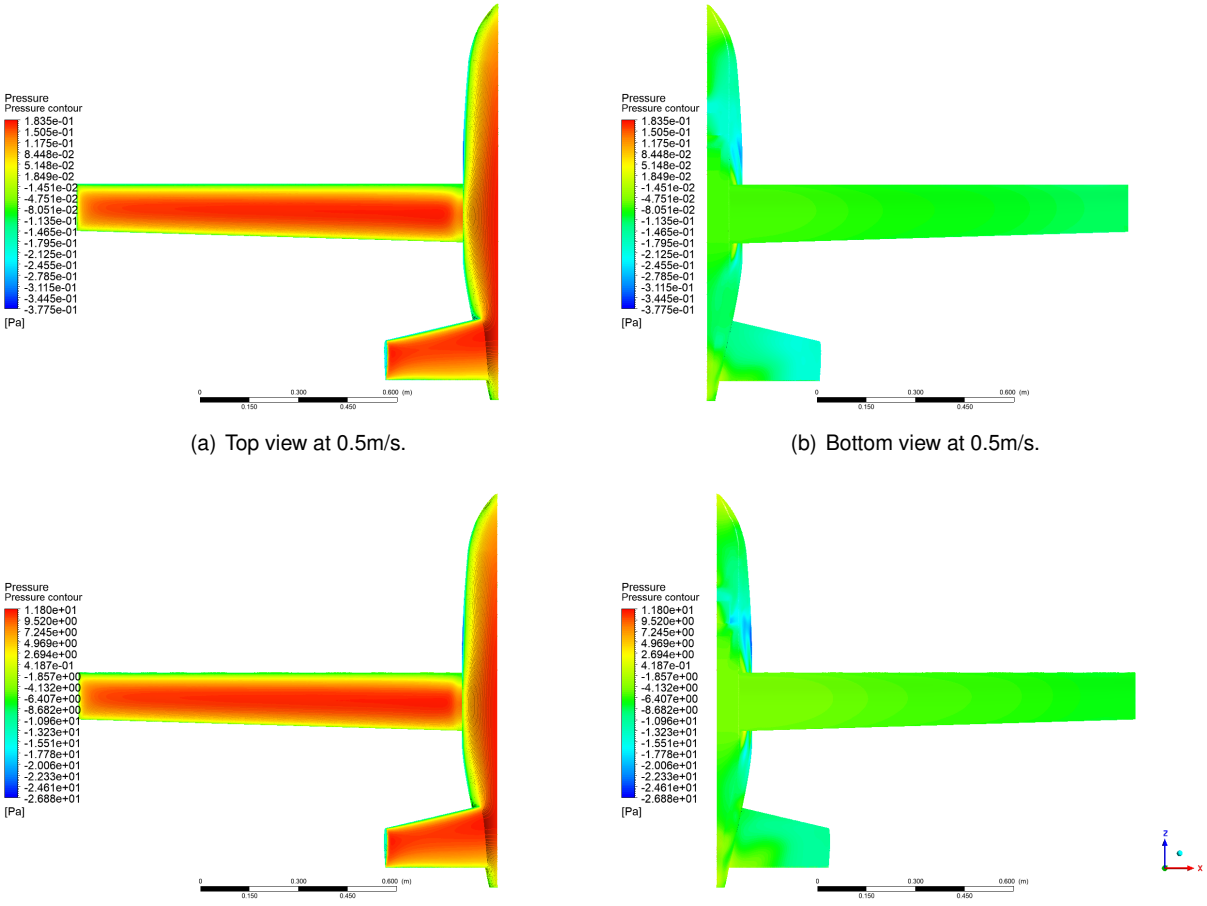

(a) Top view at 0.5m/s.

(b) Bottom view at 0.5m/s.

(c) Top view at 4m/s.

(d) Bottom view at 4m/s.

Figure 4.24: Pressure field visualization over the conventional UAV surface at axial climb velocities of 0.5m/s, in figures a) and b), and of 4m/s, in figures c) and d).

increases the length of the recirculation zone. This phenomenon can be visualized in better detail in figure 4.26.

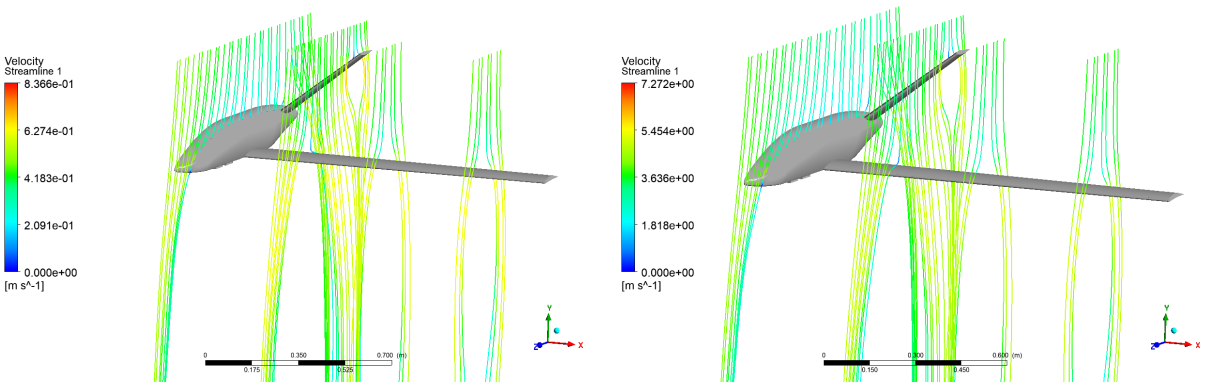

(a) Axial Climb at 0.5m/s.

(b) Axial Climb at 4m/s.

Figure 4.25: Visualization of two-dimensional streamlines located at 3.9%, 23.4%, 46.9% and 78.1% of the semi-span, during axial climb at 0.5m/s (left) and 4m/s (right).

In this figure, the recirculating zones are much clearer, and the tail growth with increasing velocity is

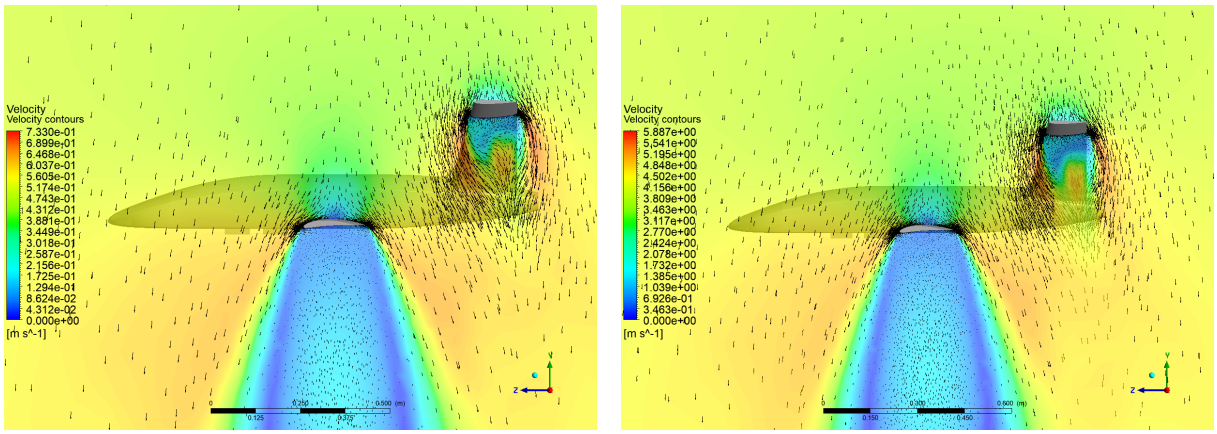

(a) Axial Climb at 0.5m/s.

(b) Axial Climb at 4m/s.

Figure 4.26: Visualization of the velocity field on a plane located at 23.4% of the semi-span, during axial climb at 0.5m/s (left) and 4m/s (right).

also more visible. Moreover, zones where flow is brought to stagnation are visible above the upper parts of the wing and tail. These zones of very low velocity flow are responsible for the increase in pressure previously identified in figure 4.24.

The aforementioned phenomena results in the loads presented in figure 4.27. The loads, represented F, are non-dimensionalized with the UAV weight, W, and the Y axis is inverted for ease of readability. From an intuitive examination of the results, the forces follow common trends found throughout aerodynamics, where the force on a given component appears to be increasing with the second power of velocity. Furthermore, the relative magnitude of the download on each component also makes sense since, in axial climb, the wing has the most frontal area relative to the flow, followed by the fuselage, and ending up with the tail.

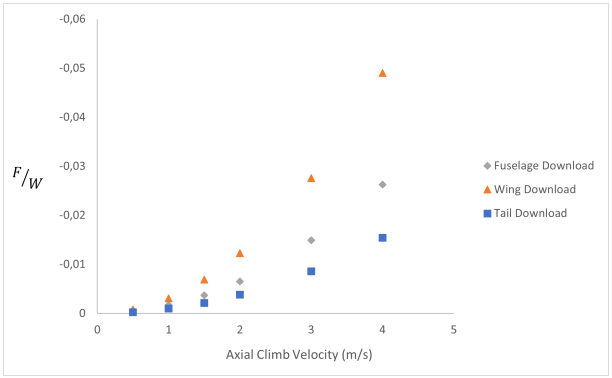

Figure 4.27: Component download comparison at different axial climb speeds.

With the above mentioned results, the aerodynamic behaviour of the full VTOL configuration can finally be evaluated. Figure 4.28 displays velocity fields at two different planes aligned with the flow, one located at 23.44% of the wing semi-span, and the other at 29.69%. Moreover, these fields are displayed both for hover conditions and axial climb conditions at a velocity of $4m/s$.

The rotor wakes display a similar behaviour to that observed in the isolated rotor. The asymmetry on the induced velocity fields of each rotor, present on plane $0.2344\frac{b}{2}$ is to be expected. Examining

specifically the front rotor, since the rear rotor has a symmetric behaviour, it is seen that induced velocity magnitudes are higher on the front blade and lower on the rear blade. This happens due to the fact that the plane has a slight offset from the plane of the blades, and, in the leftmost region the blade has just gone through it, inducing velocity on the flow, whereas on the rightmost zone the rear blade is about to go through it and then induce vertical velocity there. This behaviour is evident when compared with the induced velocity fields shown in figure 3.14.

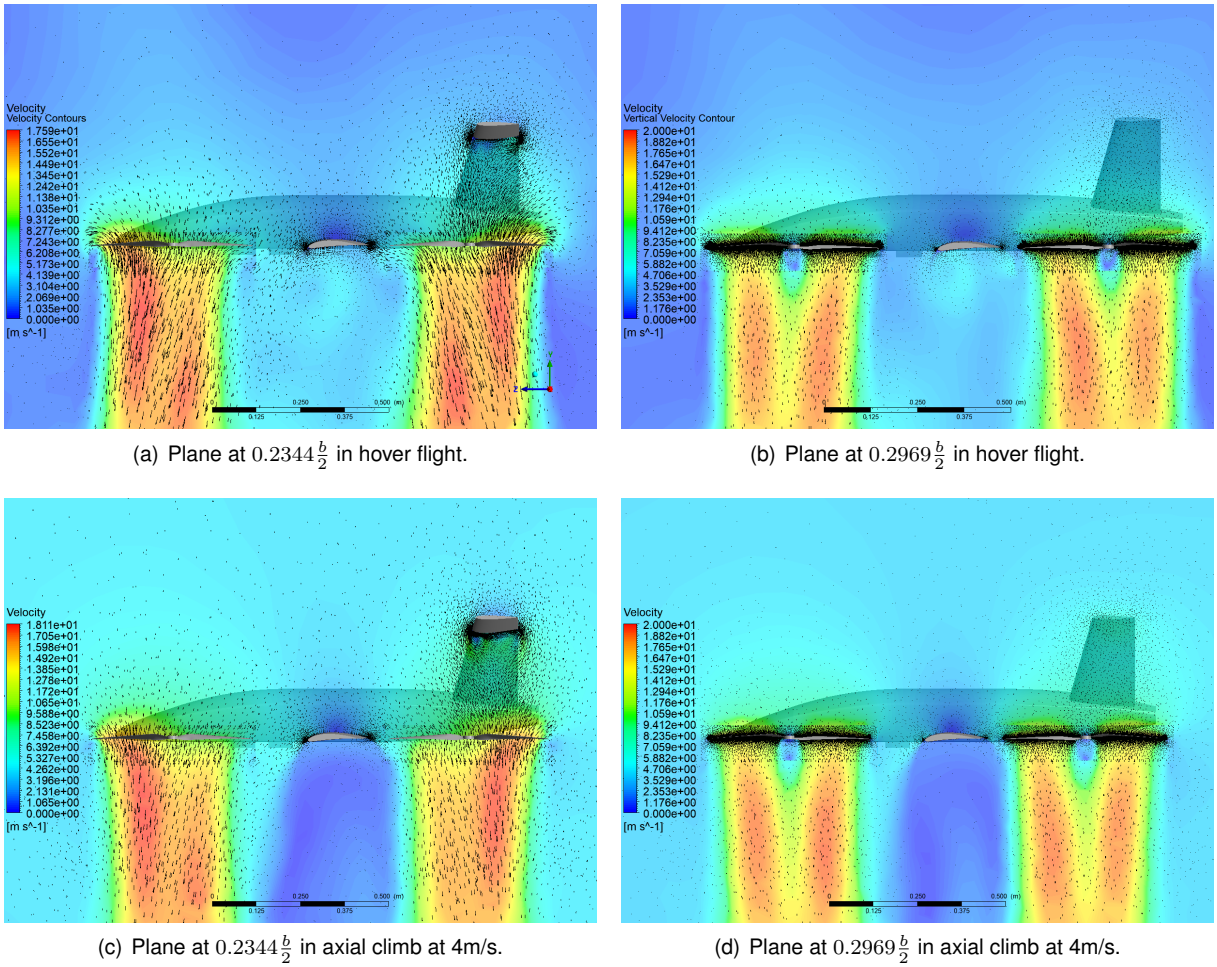

(a) Plane at $0.2344\frac{b}{2}$ in hover flight.

(b) Plane at $0.2969\frac{b}{2}$ in hover flight.

(c) Plane at $0.2344\frac{b}{2}$ in axial climb at 4m/s.

(d) Plane at $0.2969\frac{b}{2}$ in axial climb at 4m/s.

Figure 4.28: Visualization of the velocity fields on planes located at 23.44% (left) and 29.69% (right) of the wing semi-span, during hover (top) and axial climb at 4m/s (bottom).

In the aforementioned plane, the recirculating flow below the tail is also visible, both in hover and during climb. As observed previously in the conventional configuration, the recirculating zone increases in size as the axial velocity increases, and the same behaviour can be observed with the complete configuration. A more in depth understanding of the tail's influence on the velocity field of the flow feeding the rear rotor is possible by examination of figure 4.29, which displays the same data as in the previously mentioned figure, but on a plane located at the mid section of the rear rotor. There, a clear distinction can be made between the left side of the rotor where air is flowing freely to the rotor disk, and the right part where the tail, to a greater extent, and the fuselage, to a smaller one, act as a blockage that air must circumvent in order to reach the rotor. Such behaviour is both expected to decrease the rotor performance, and to generate loads on the tail and fuselage as the rotor forces the flow to go around

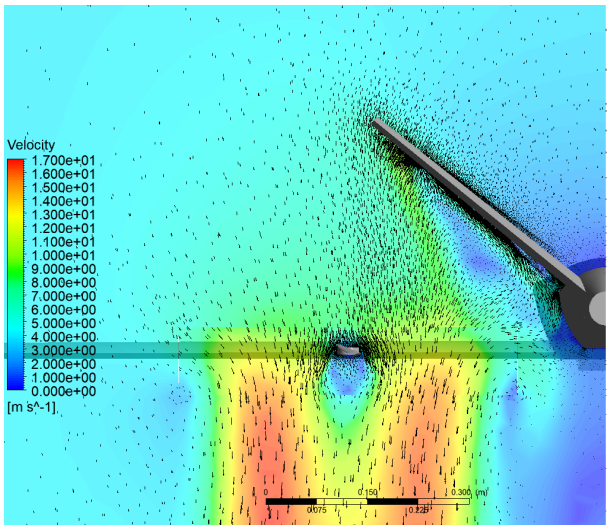

Figure 4.29: Visualization of the velocity field, during axial climb at 4m/s, in a plane located on the rear rotor axis, transversal to its blades.

them.

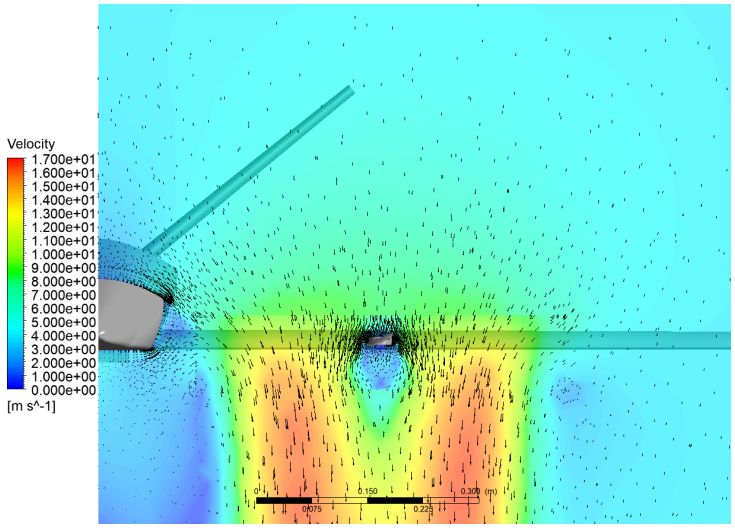

Figure 4.30: Visualization of the velocity field, during axial climb at 4m/s, in a plane located at the front rotor axis, transversal to its blades.

An equivalent analysis is performed to the velocity field in the front rotor's midsection and is visible in figure 4.30. In this figure, it is noticeable that air flows much more freely to the rotor, being only slightly influenced by the fuselage, on the left.

The described flow structures result in the pressure fields over the wing, fuselage and tail, shown in figure 4.31. It is visible how greatly affected by the rotors the pressure field is, especially on the tail. It can be seen that the rotors induce higher maximum pressures over the UAV top side than those obtained by the isolated UAV at a climb speed of $0.5m/s$, and the same happens at a climb speed of $4m/s$. Furthermore, the low pressure zones below the tail strongly increase in magnitude.

The resulting download on each component, represented by F_f, F_w and F_t, where the subscripts f, w, and t correspond to the fuselage, wing and tail, respectively, are provided in figures 4.32, 4.33,

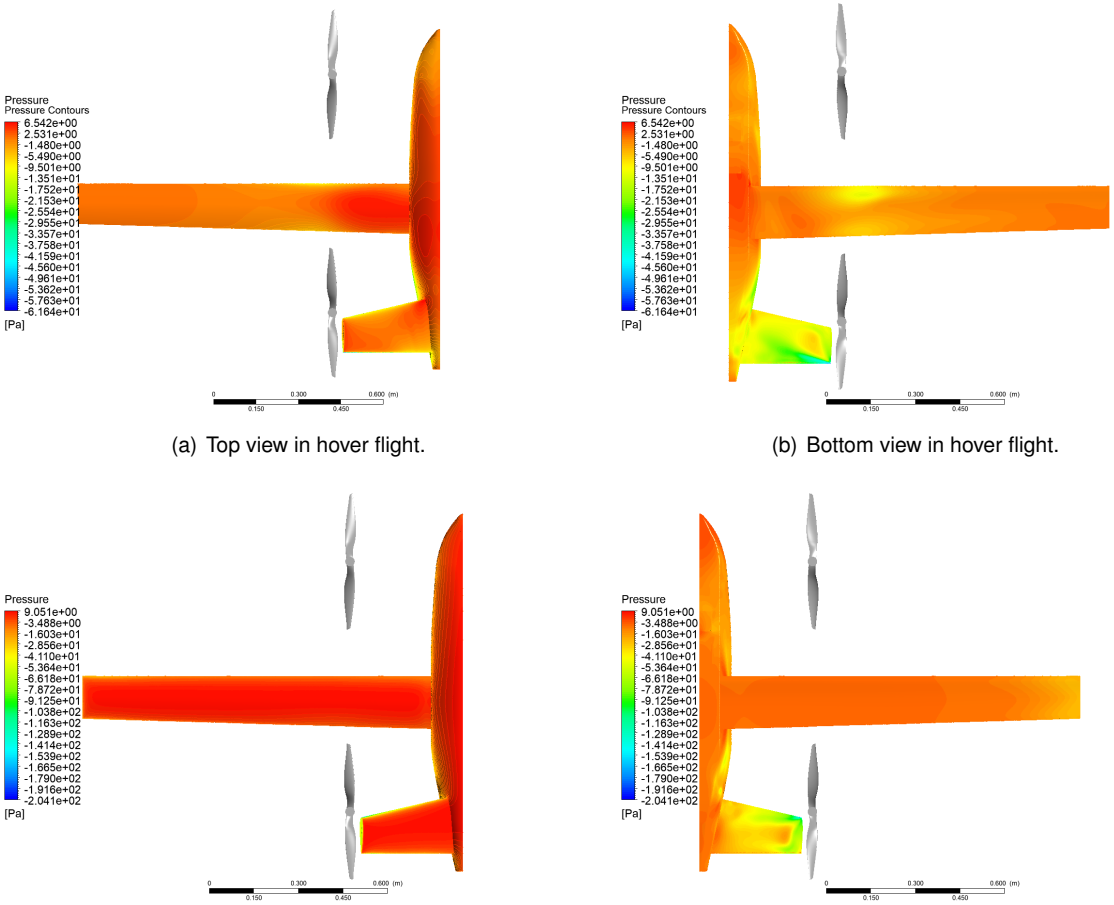

(a) Top view in hover flight.

(b) Bottom view in hover flight.

(c) Top view in axial climb at 4m/s.

(d) Bottom view in axial climb at 4m/s.

Figure 4.31: Pressure field visualization over the full UAV's surface in hover, in figures a) and b), and with axial climb velocity of 4m/s, in figures c) and d).

and 4.34. Aside from some outlier points, in general, the presence of the rotors increases the download on the components, as would be expected. Such increase happens to a lower extent in the fuselage and wing, but when it comes to the tail, it becomes very significant, making the download on the tail the highest of the three, until it is overcome by the wing at climb velocities above $2m/s$. This load on the tail is seen to increase almost 40 times while climbing at $0.5m/s$, with the effect rapidly diminishing with increasing axial velocity, but still more that duplicating the tail's download while climbing at $4m/s$, compared to the conventional configuration without rotors in axial climb.

Additionally, the changes in thrust generated by each rotor, relative to the previously calculated values for the isolated rotor are shown in figure 4.35.

In hover, a performance hit is verified in both the front and rear rotors when compared to their thrust when isolated, with the front rotor suffering a negligible decrease in thrust, whereas the rear rotor suffers a relatively big penalty. This can be justified by the previously identified blockage created by the tail and fuselage above the rear rotor, which obstructs the air being pulled by the rotor, reducing its performance. On the other hand, the front rotor has a much more unimpeded path above it, being able to pull more air.

Conversely, as the UAV starts moving axially, the behaviour identified above immediately changes and the rear rotor becomes the one producing the most thrust. This tendency holds true as vertical

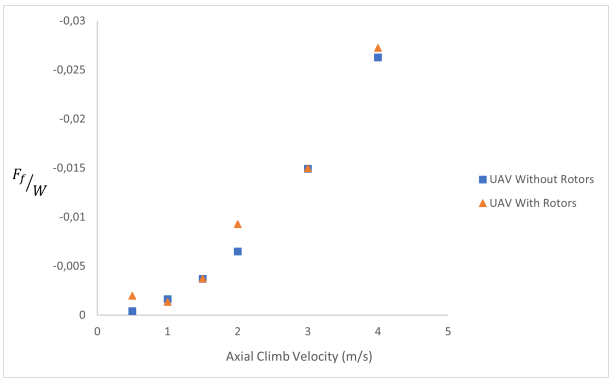

Figure 4.32: Comparison of fuselage download between the full VTOL configuration and conventional configuration during axial climb.

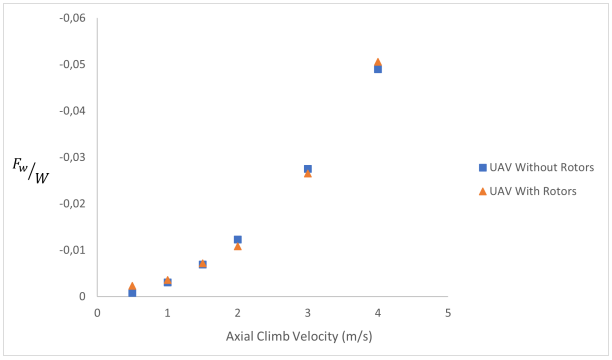

Figure 4.33: Comparison of wing download between the full VTOL configuration and conventional configuration during axial climb.

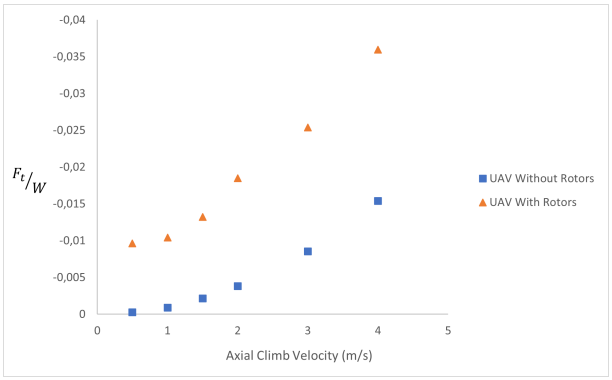

Figure 4.34: Comparison of tail download between the full VTOL configuration and conventional configuration during axial climb.

velocity continues to increase. While in hover the blockage produced by the tail resulted in an obstruction to the incoming flow and consequently reducing the rotor's performance, when the vertical velocity increases, that blockage starts working as a shield, protecting the rotor from high vertical velocity components.

To better understand how this affects the rotor's propulsion, one should first briefly explain how axial velocity relates with rotor thrust. If one decomposes the velocity vector relative to a given section on the blade, in hover, two components are identified. The horizontal component corresponds to the rotation speed of the chosen section, and the vertical corresponds to the induced velocity by the rotor. As the

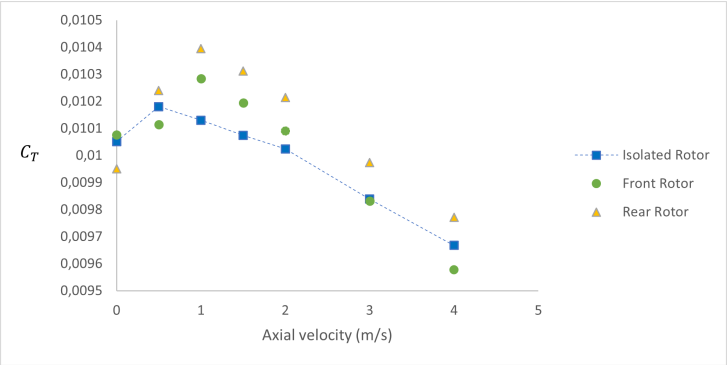

Figure 4.35: Thrust coefficient comparison between front, rear and isolated rotors with different axial velocities.

rotor starts moving axially, its axial velocity is added to the induced velocity, which results in a decrease in the angle of attack formed between the flow and the section, and the consequent decrease in thrust. Hence, why the rotation speed must be increased with axial velocity.

What happens in the situation regarding the rear rotor, is that the tail reduces the incoming flow's axial velocity. Since the rear rotor is rotating at a velocity that is determined based on the isolated rotor's performance, it is actually rotating slightly faster than would be required to match the desired thrust, hence the increase in performance.

With the front rotor air can flow relatively unimpeded, and thus it ends up generating less thrust than the rear rotor. It is not clear, however, why the front rotor performs better than the isolated one at the lowest and highest velocities, while performing worse at medium velocities.

Table 4.8 presents the area averaged vertical velocity in disks positioned immediately above the rotors, calculated at axial climb velocities of 0, 2 and $4m/s$. This data confirms that the rear rotor is, in fact, fed by lower velocity flow.

Table 4.8: Average vertical velocity above the rotors at different axial velocities.

Axial Velocity (m/s)	Vertical Velocity (m/s)	
	Front Rotor	Rear Rotor
0	-6.039	-5.901
2	-6.304	-6.091
4	-7.783	-7.32

It is important to notice, however, that this interaction between the rear rotor and the tail does not result in the UAV getting better performance. As an example, even though the thrust generated by the rear rotor increases in $0.47N$ compared to the isolated rotor, while climbing at a $2m/s$, that value is completely offset by the $0.72N$ increase in the tail's download due to the rotor being present.

In order to assess if the negative influence of the interaction between the rotors and the remaining components on VTOL performance could be decreased, a similar study to that present in subsection 4.2.1 was performed, by evaluating the download on the UAV structures and the rotors' thrust with them located at different positions, namely at 37.5%, 45.3% and 51.3% of the wing semi-span. No studies

were made by moving the rotors forward nor backwards, as positioning them closer to the wings could generated undesirable interference, and moving them away would increase the UAV's footprint which can make it less versatile for some use cases.

The result of changing the position was evaluated mainly on the tail download as that is the component which is most affected by the rotor. Figure 4.36 shows the tail download at different rotor positions, at an axial climb speed of $4m/s$.

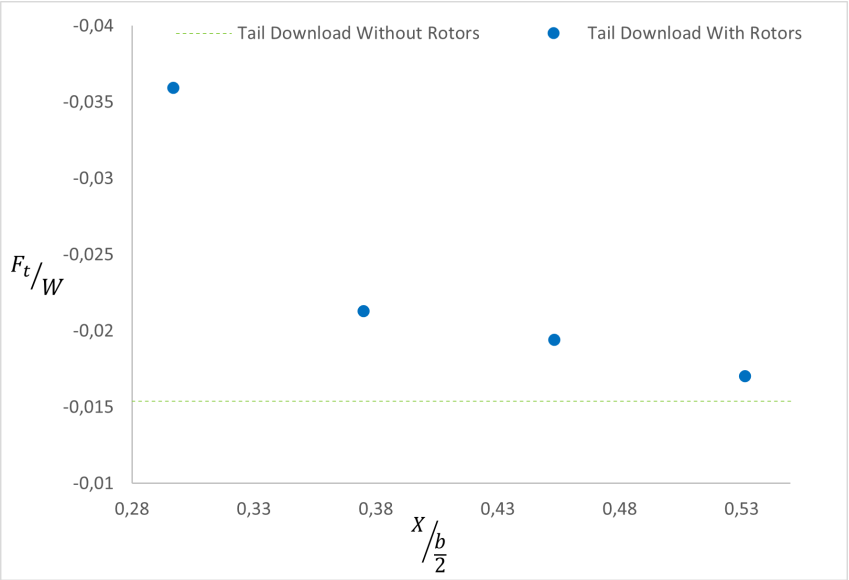

Figure 4.36: Comparison of tail download at different rotor positions along the wing semi-span.

It is evident that moving the rotors away from the tail decreases its download, and that it quickly tends to the value obtained without rotors. Once again the biggest constraint against moving the rotors further away from the wing root is the structural requirements at the root due to the increased bending moment. A simulation was performed using the conventional configuration in horizontal flight at an angle of attack such that the lift matched the UAV MTOW. With both the rotors and wing producing the same vertical force, the bending moments produced by each were calculated and are presented in table 4.9.

Table 4.9: Bending moment at the wing root caused by the wing and rotors at different positions.

	Wing	Rotors			
		$0.297\frac{b}{2}$	$0.375\frac{b}{2}$	$0.453\frac{b}{2}$	$0,531\frac{b}{2}$
Bending Moment (Nm)	25.794	14.896	19.719	24.469	28.919

From these results, and without delving further into structural calculations, one could safely locate the rotors at 45.3% of the wing semi-span, since the bending moment at the wing root would still be lower than that generated by the wing. In reality, in this category of aircraft, structures need to designed capable of withstanding typical load factors in the order of 3, meaning that the wing needs to support three times the UAV weight, so there is still margin to move the rotors further away. For the sake of convenience, the aforementioned position can safely be chosen and it still provides better performance than the originally considered.

Compared to the configuration without rotors, at a climb speed of $4m/s$, the increase in total download with the rotors located at 45.3% of the semi-span is of 4.19%, which is 17.0% lower that that of the original configuration with the rotors located at 29.7% of the wing semi-span. Consequently, in order to compensate the UAV weight and download on the structures, the rotors would require a thrust factor, a ration between thrust and UAV weight, of $\frac{T}{W} = 1.112$ with the rotors located in the original position, and $\frac{T}{W} = 1.092$ with the rotors located at 45.3% of $\frac{b}{2}$. These values present an underestimation of the total thrust required since the rotor booms were not taken into account during these simulations and they should contribute in a non negligible way to the downloads.

The velocity field near the rear and front rotors is shown in figure 4.37. There, it is possible to see that the velocity field shows less interaction between the rotors and the fuselage and tail, when compared to the velocity fields in figures 4.29 and 4.30.

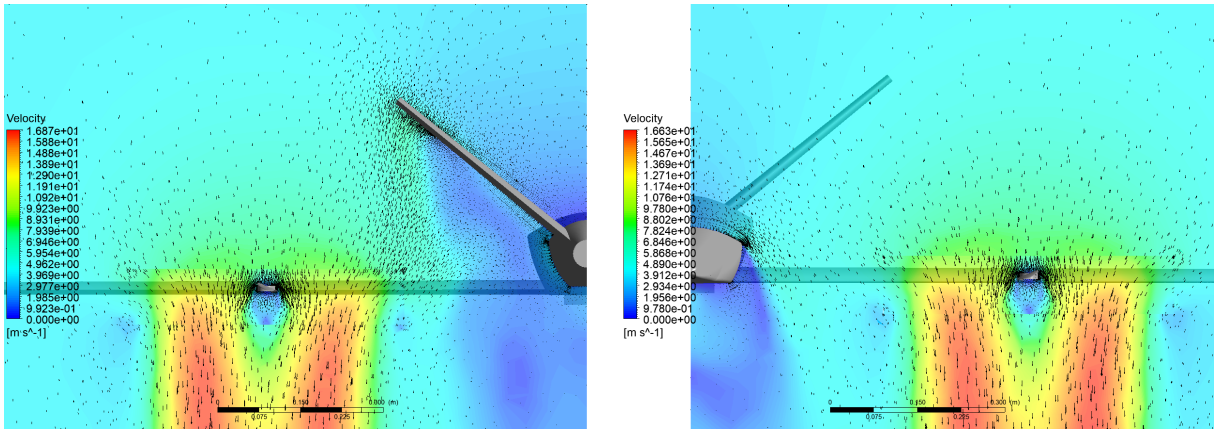

(a) Front rotor plane.

(b) Rear rotor plane.

Figure 4.37: Visualization of the velocity field on the rear and front rotors' planes, at an axial climb velocity of 4m/s, with the rotors located at 45.3% of the wing semi-span.

4.2.3 Transition Flight

As concluded in subsection 4.2.1, based on the results obtained in cruise flight, the orientation of the rotors relative to the incoming flow has a significant impact on the aerodynamic loads that act on the remaining structures. During transition flight, one can expect this effect to be amplified due to the added rotor motion.

For this reason, coupled with the statements made in subsection 4.1.3, the initial goal was to perform simulations with the rotors oriented in the same positions as in horizontal flight, however, the numerical models/spatial discretization appear to have shown their limitations as simulations became harder to converge, where those performed with the rotors aligned with the flow not converging. In fact, the applications in which the MRF method is usually employed either show a flow dominance in the axial direction or present some sort of axisymmetry, as are the cases in turbomachinery and in mixing tanks, whereas in this application the flow shows a strong velocity component in a transverse direction to the rotor disk plane. This method has been applied in [12] to study transition between vertical and horizontal flight, however it was performed on a tilt-rotor configuration, where the horizontal velocity is matched

with rotor tilt, which confers the axial aspect to the flow.

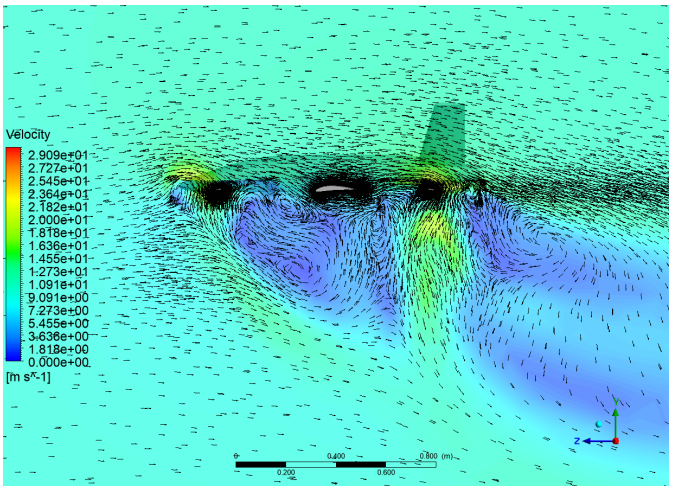

(a) 10 m/s.

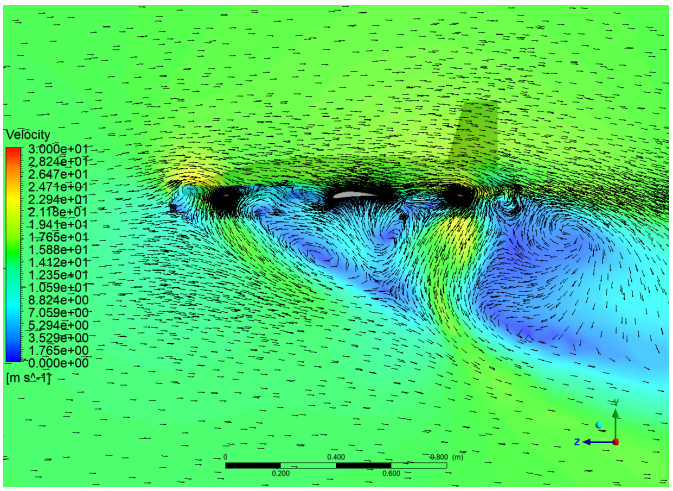

(b) 15 m/s.

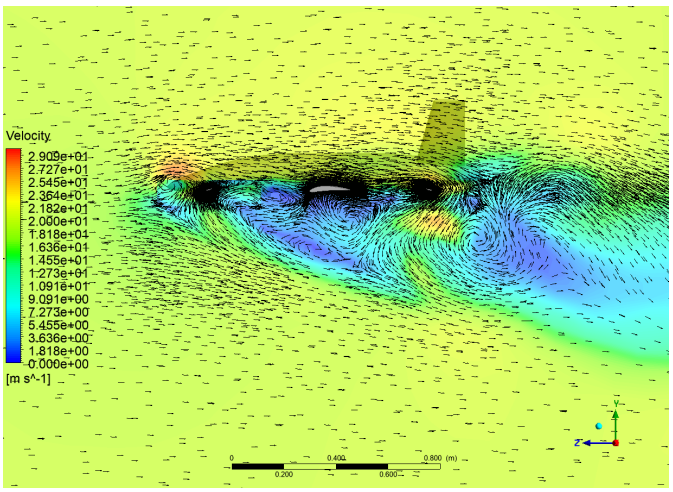

(c) 20 m/s.

Figure 4.38: Visualization of the flow velocity field in a plane located at 41.41% of the wing semi-span, at velocities of $10m/s$, $15m/s$ and $20m/s$.

Given this fact, the results presented from this point forward correspond only to having the rotor blades perpendicular to the incoming flow. Furthermore, the analysis done to the results will focus mainly on a qualitative evaluation of the flow and the absolute values must be taken with a grain of salt. Ignoring eventual transient effects, just like in subsection 4.2.1, it is expected that the results obtained from having the blades perpendicular to the incoming flow constitute a worst case scenario in terms of the aerodynamic interaction between the rotors and other UAV components.

Figure 4.38 shows the velocity fields on a vertical plane aligned with the flow at 41.41% of the wing semi-span, at the horizontal velocities of $10m/s$, $15m/s$ and $20m/s$. It is immediately clear that the flow is much more complex than in the horizontal and vertical flight stages. Despite this, it is possible to identify flow structures belonging to both.

Such structures are the front and rear rotor wakes which are seen forming below their respective rotor. One interesting characteristic of the wakes is that they form at different angles. The front wake is seen to flow at an angle relative to the vertical axis, whereas the rear wake develops almost vertically. Such behaviour can be explained based on the influence of the incoming horizontal flow. The front wake is impinged by the upcoming flow and is convected horizontally with it, forming the visible angle. However, the wake presents itself as an obstacle to the horizontal flow, compared with its normal trajectory, were the wake not to be present. The wake functions almost as if a wall was present in front of the horizontal flow, which ends up being deflected downward and around it. This is visible by the low velocity zone, in blue, with high recirculation flow, right after the front wake, which is similar to the recirculation zones left behind blunt objects. The resulting low velocity flow behind the front rotor wake has a much weaker interaction with the rear rotor wake, and consequently, that wake can develop vertically, similarly to what happened in hover flight. As the rear wake develops downward is impinges on the angled front rotor wake, starts being influenced by the horizontal velocity, and gets convected away, progressively becoming more horizontal. A similar recirculation zone to that formed behind the front rotor wake is observed behind the rear rotor wake, whereas this one appears to be less intense. This can be attributed to the fact that the recirculation zone behind the front rotor is being influenced by the velocities induced by the front rotor to the left, by the rear rotor to the right and by the presence of the wing on top.

It is also visible that the front rotor induces downwash on the air flowing over the front rotor, which comes in contact with the front wing at a negative angle of attack. The low pressure recirculating flow beneath the wing and the negative angle of attack are expected to result in a decrease in lift on the wing sections affected by the rotors.

A final characteristic taken from these velocity fields is that, as horizontal velocity increases, its impact on the wakes becomes stronger and, as such, the angle the front wake makes with the vertical axis becomes progressively higher. This results in the height of the recirculation zone behind it to decrease and, for this reason, the rear wake is less protected, and so it develops vertically through a smaller length and the gets convected with the front wake. A curious effects that occurs in the rear wake is that with the increasing horizontal velocity the wake starts developing slightly at a forward angle with the vertical axis. This might happen due to a decrease in pressure inside the recirculation zone behind the front wake, which pulls the rear wake slightly forward.

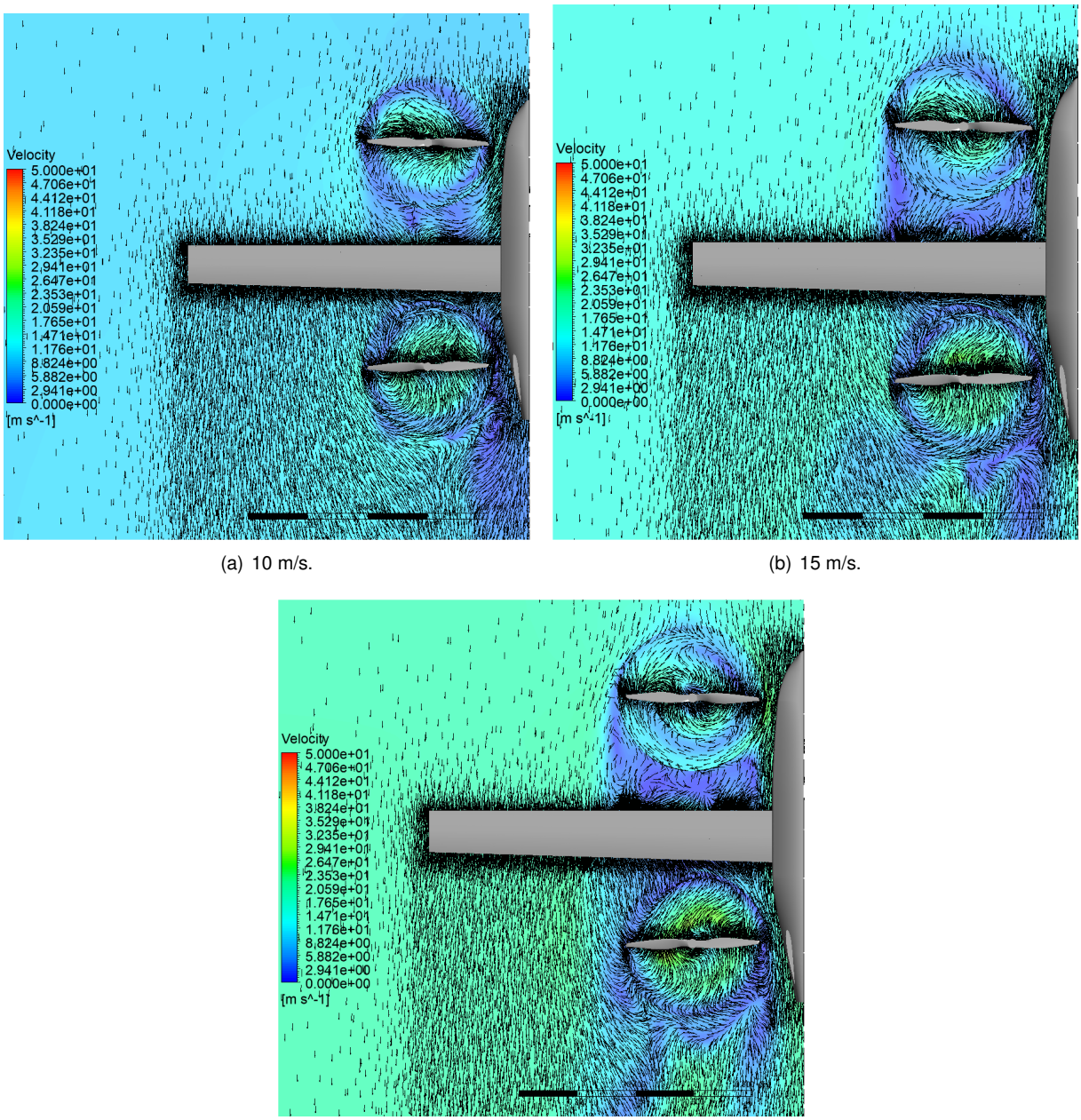

(a) 10 m/s.

(b) 15 m/s.

(c) 20 m/s.

Figure 4.39: Visualization of the flow velocity field on a horizontal plane located immediately below the rotors, at velocities of $10m/s$, $15m/s$ and $20m/s$.

Figure 4.39, displays the velocity fields in a horizontal plane below the rotor at the same velocities as the previous figure. Here, the recirculation zones previously identified are visible. The incoming horizontal flow needs to go around the rotor wake, as stated before, and that behaviour can also be seen in these velocity fields, where the incoming flow in front of the front rotor gets deflected away from it, either getting stuck between the rotor and the fuselage on the right side, or being deflected to zones farther away from the wing root. The faster the horizontal velocity, the bigger the horizontal deflection, which is also seen by the growing width of the recirculation zone as velocity increases. It should be noted in this figure that the ANSYS CFD-Post software used to post-process the simulation results represents velocity vectors relative to the corresponding reference frame, and, as such the vectors inside each rotor

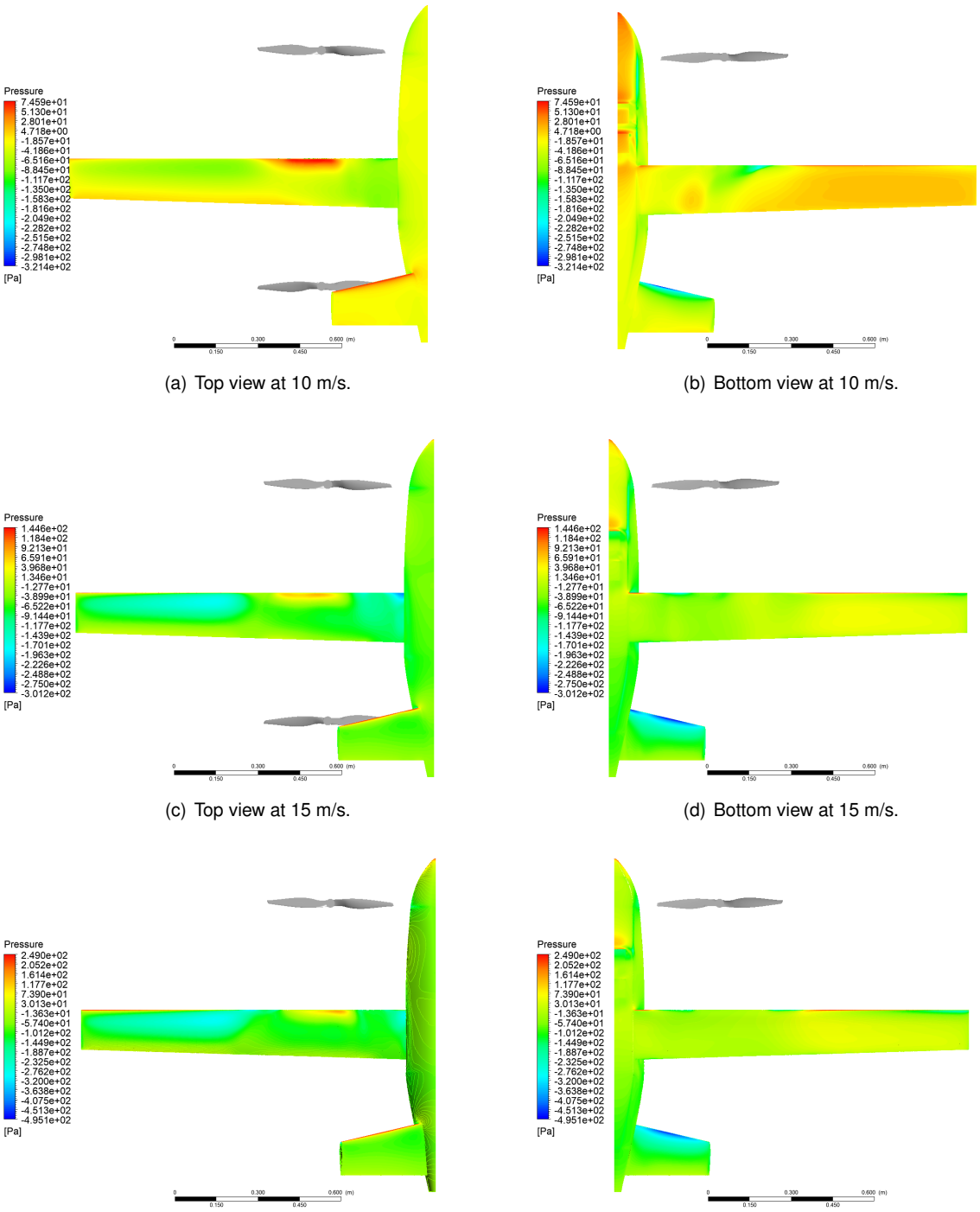

(a) Top view at 10 m/s.

(b) Bottom view at 10 m/s.

(c) Top view at 15 m/s.

(d) Bottom view at 15 m/s.

(e) Top view at 20 m/s.

(f) Bottom view at20 m/s.

Figure 4.40: Visualization of surface pressure field over the top (left) and bottom (right) of the UAV, at velocities of $10m/s$, a) and b), $15m/s$, c) and d), and $20m/s$, e) and f).

domain correspond to the velocity relative to the rotor movement and not the absolute velocity, Hence, no circular velocities are actually present in the rotor's outer disk.

These flow structures result in the pressure distributions identified in figure 4.40. From this figure, one can confirm some of the predictions made based on the velocity fields. A meaningful characteristic of these pressure distributions is the high pressure zone present in the wing's leading edge, in the sections

behind the front rotor, on the wing's upper side. Conversely, a lower pressure zone is identified on the same region of the wing but on the lower side. These pressures directly relate to the downwash induced by the rotor on the incoming flow which decreases the angle of attack. A similar phenomenon is visible on the tail, caused by the downward velocities induced by the rear rotor, resulting in higher pressures on the top surface and lower pressures on the lower surface. Similar loads were also observed in vertical flight.

An interesting result taken from these pressure fields is that away from the root, after about half of the wing semi-span and up to the tip, bigger and more intense suction and pressure zones are present on the wing's upper and lower sides, respectively. This leads one to expect higher lift generation in that zone of the wing.

Deeper conclusions on this behaviour are drawn through examination of the pressure coefficient plots present in figure 4.41, located in the region marked by the rotors influence and other away from it.

Starting by examining the pressure coefficient distribution far from the wing root, one sees some changes in behaviour when compared to what was observed in cruise flight, however the generic shape is kept. To begin with, The suction peak that was identified in cruise flight, on the wing lower side, is shown to have its intensity greatly reduced in transition flight, even though it is also seen that it increases with velocity. This should indicate that the incoming flow, that was deviated by the influence of the front rotor, arrives with a higher angle of attack, not needing to go through such an extreme curvature as that identified in subsection 4.2.1. Overall these plots show a stronger suction present on the upper side and a more constant pressure shown on the lower side, indicating that a higher C_l should be generated on these sections.

Examination of the C_p plots located on the rotors' region of influence shows a different pressure distribution from that which was shown in horizontal flight. It shows a strong dependency on UAV's horizontal velocity, where the suction and pressure peaks completely change based on the forward speed, whereas, typically, the pressure coefficient distribution shape is approximately constant in a given range of Reynolds numbers. Such behaviour can be attributed to the fact that the velocity induced by the rotors remains approximately constant when the forward velocity changes. This means that the relative proportions between both are not kept constant, specifically that at low forward velocities the downwash induced by the front rotor represents a more significant part of the flow velocity contacting the wing, meaning that the angle of attack is more negative, and, as forward velocity increases, the influence of the downwash decreases, meaning that a variation of the forward speed also constitutes a variation the the effective angle of attack on that region of the wings.

At $10m/s$ the high negative angle of attack results in very high suction near the leading edge, in the wing's lower side, followed by low pressures throughout the remaining length, whereas on the top side, a pressure peak is present near the leading edge, followed by weak suction. This most probably results in negative lift being generated in the corresponding section. The increase in forward velocity eliminates the high suction effect on the lower side, and the high pressure on the upper side decreases and at $20m/s$ disappears. Throughout the lower side, pressure remains approximately constant, which can be caused by the highly diffused flow present in the recirculation zone below the wing.

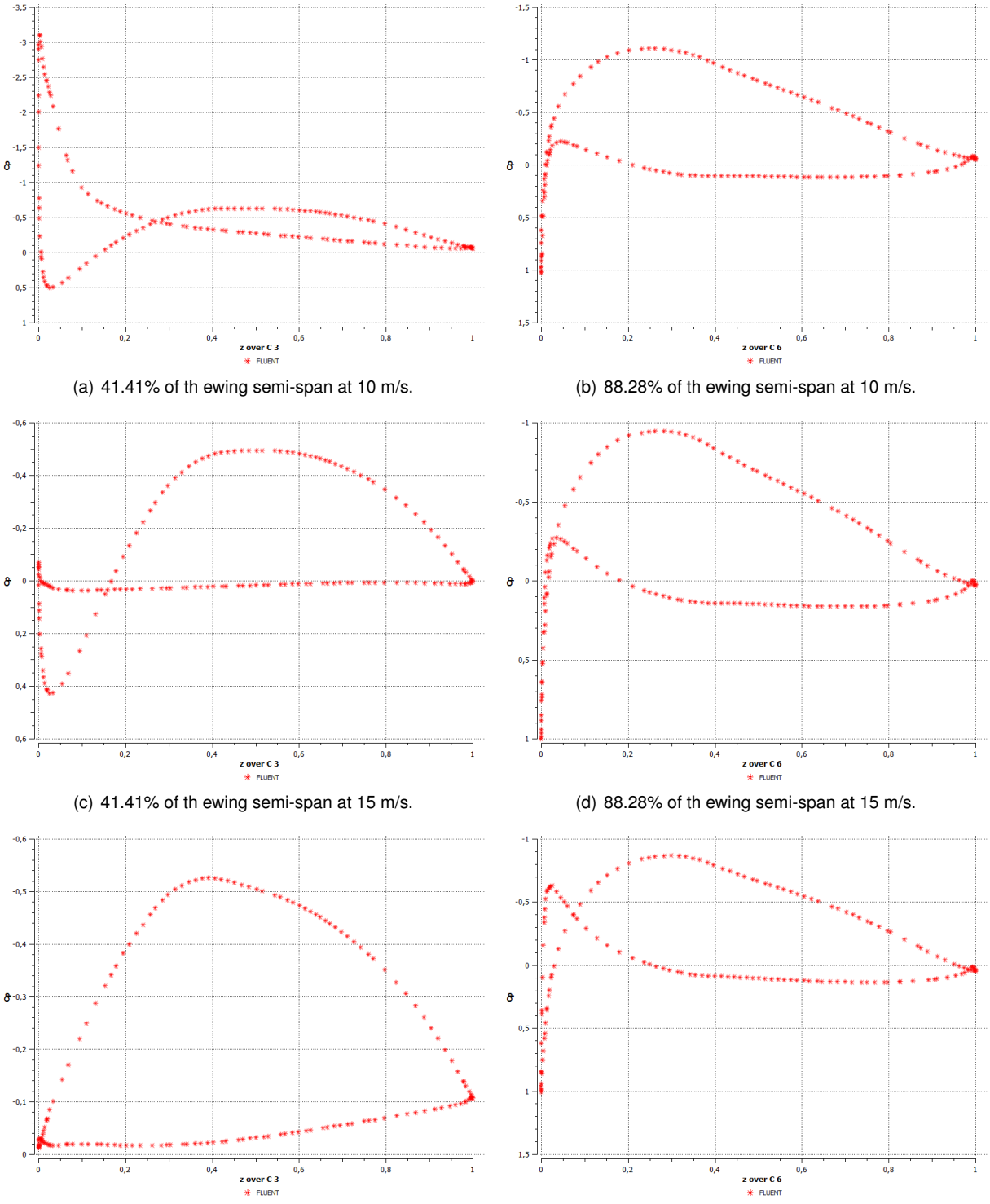

(a) 41.41% of th ewing semi-span at 10 m/s.

(b) 88.28% of th ewing semi-span at 10 m/s.

(c) 41.41% of th ewing semi-span at 15 m/s.

(d) 88.28% of th ewing semi-span at 15 m/s.

(e) 41.41% of th ewing semi-span at 20 m/s.

(f) 88.28% of th ewing semi-span at 20 m/s.

Figure 4.41: Wing pressure coefficient plots in planes located at 41.41% of the wing semi-span (left) and at 88.28% of the wing semi-span (right), at velocities of $10m/s$, a) and b), $15m/s$, c) and d), and $20m/s$, e) and f).

The resulting C_l distribution along the wing span is displayed in figure 4.42 at different forward velocities, with the conventional configuration present as a baseline for comparison. If only the forward velocity was playing a role in the wing aerodynamics, then the C_L distribution would be expected to remain constant as it is not dependent on velocity. However, it is the relative magnitudes of the rotors'

induced velocities and the forward flight velocity which affect the aerodynamic coefficients, resulting in the observed changes.

The predictions made based on the velocity fields and pressure distributions are now confirmed with these results, where a significant dip in C_l occurs in the wing sections immediately behind the front rotor, due to its downwash, and an increase in C_l occurs in the areas outside this zone due to the deflected streamlines going around the rotor wake. From this data, one can also conclude that these effects are stronger, the lower the forward speed is, as shown by comparing the $10m/s$ curve, where the biggest through in C_l is visible, even attaining negative values, while also presenting the highest lift coefficient in the outer section of the wing, to subsequent higher velocities, where it is visible that the valleys do not get as low and the peaks do not get as high. Finally it is seen that, as the forward velocity matches that of horizontal flight, the horizontal and transition curves have a good fit near the root and wing tip, with stronger variations in the distribution occurring in the zones where the interaction with the rotors is stronger.

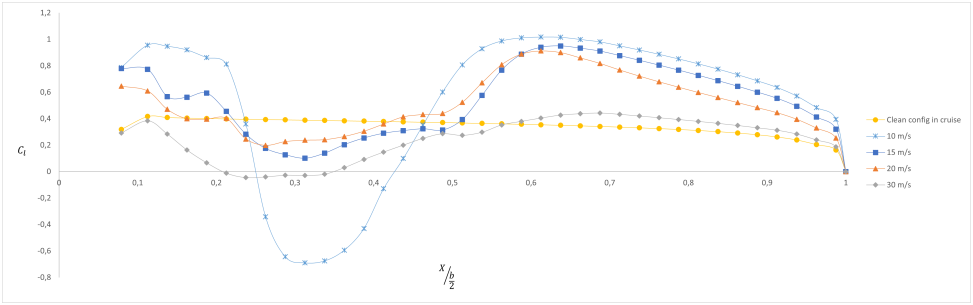

Figure 4.42: Two-dimensional lift coefficient distribution comparison between conventional configuration and VTOL configuration during transition flight at different forward velocities.

The resulting ratios of lift in transition flight over the lift in cruise flight generated by the wing are shown in table 4.10.

Table 4.10: Lift ratio between wing lift in transition flight and cruise flight at different forward velocities.

Forward Speed (m/s)	10	15	20	30
Lift Ratio	0.1725	0.4013	0.6669	0.7187

As expected, as the forward velocity increases, so does lift, but at $30m/s$ it still only corresponds to 71.87% of the value generated in cruise flight by the conventional configuration. Such decrease can be attributed to the wing interacting with the rotors.

In these tests the rotors' angular velocity was kept constant and equal to that used in hover flight, in order to keep the rotor variables constant and change only the forward velocity. However, by keeping the rotor velocity constant, what is kept approximately constant is the rotor power and not its thrust. According to momentum theory, for an advancing rotor, the power requirements decrease significantly with forward velocity up to a minimum and then increase again [28]. Given that the rotor velocity was kept constant, a surplus of power was being introduced into the flow, and thus resulting in an increase in thrust, which contributes to an even stronger interaction with the rest of the UAV. In fact, such an

increase was observed throughout the results and is shown in table 4.11, even though it does not follow any prediction made using Momentum Theory.

Table 4.11: Front and rear rotor thrust coefficients at different forward velocities

Forward Speed (m/s)	10	15	20	30
Front Rotor C_T	0,010557	0,01093	0,012084	0,014512
Rear Rotor C_T	0,010456	0,01046	0,010832	0,012571

The actual procedure in transition flight is to regulate the thrust being produced by the rotors with the lift being generated in the wing so that together they match the UAV weight, and as velocity increases, the rotors generate successively lest thrust, until it is completely assured by the wings. As stated above, the procedure should have been to keep the thrust constant on each rotor to evaluate the impact on forward velocity on the aerodynamic interaction, and then to perform the opposite, leave the forward velocity constant and vary the rotor thrust, however such procedure was not possible due to the convergence difficulties that arose during this study. In fact, in order for any qualitative evaluation of the results presented above, during transition, to be possible, a relaxation to the convergence criteria had to be allowed. Due to this, it was not possible to match the rotors' thrust with the UAV lift since there was not enough confidence on the accuracy on the exact values of thrust.

Chapter 5

Conclusions

5.1 Achievements

During the span of this thesis, multiple steps were taken to reach the final goal of evaluating the aerodynamic interaction between the beVTOne's rotors, wings, fuselage and control surfaces during the different flight stages of operation, and obtain tangible data on how said interaction affects the UAV performance parameters, namely C_L, C_D and $\frac{C_L}{C_D}$ in cruise flight, C_T, $C_P W$ and $\frac{T}{W}$ in vertical flight, and a mixture of the above metrics in transition flight.

To do so, an initial study of the methods required to simulate the intended flight stages was performed in chapter 2. To simulate cruise flight, the conventional RANS simulations coupled with a turbulence model were enough, however, for vertical and transition flight an additional model was required to take into consideration the movement of the rotors. Based on this, four different types of rotation modelling techniques were identified and, from those, three specific models of interest were selected, namely the MRF, the Sliding Mesh, and the Overset Mesh models. Moreover, two turbulence models widely used in aerospace applications were identified to be tested, the $k-\omega$ SST and the Spalart-Allmaras.

In chapter 3, the whole pre-processing of the simulations was performed, ranging from preparing the geometries and the simulation domains, generating appropriate meshes to obtain mesh independent solutions, implementing the chosen models and setting up the required boundary conditions so that the simulations can be performed. At this point, it was verified that the Sliding Mesh and Overset Mesh models are too computationally demanding to be employed during the iterative design phase of an UAV, however, at the end of the chapter, the results obtained with the MRF method were verified and validated based on performance data provided by the propeller manufacturer and showed accurate predictions. Moreover, results regarding the rotor performance IGE at different ground inclinations were compared with experimental data from [30], showing a good match.

Finally, in chapter 4, all the different results obtained from the simulations during the three flight stages of horizontal flight, vertical flight and transition flight, were presented and an in depth examination was performed. At each specific stage, the VTOL and cruise structures were examined independently, and then assembled, so that conclusions on the interaction between both structures could be made.

In cruise flight, the VTOL structures, with the rotor blades aligned with the incoming flow, resulted in a decrease in lift generated by the wing of approximately 1% and an increase in drag of approximately 2%. Moreover, the VTOL structures introduced extra drag due to the presence of new components. These resulted in a decrease in lift-to-drag ratio from 10.45, in the cruise configuration, to 7.28 in the assembled configuration with the rotor blades parallel with the flow. The position of the rotors along the wing semi-span did not show a significant impact on the UAV performance, however, the orientation of the blades relative to the incoming flow did, and having the blades perpendicular to the flow resulted in a higher influence in the wing lift and drag, and in a further decrease in lift-to-drag to 6.82.

In vertical flight the main interaction between the cruise and VTOL structures was observed in the tail and rear rotor, however, all the cruise structures showed an increase in download induced by the rotors. Similarly, the rotors showed an impact in the capacity to generate thrust, relative to an isolated rotor, due to the presence of the cruise components, which was different in each rotor. The front rotor produced more thrust than the rear in hover flight, whereas the inverse happened throughout all the evaluated climb velocities. Moving the rotors away from the fuselage resulted in lower downloads being applied to the cruise structures, mainly due to reducing the interaction of the rear rotor with the tail. Having the rotors located at 45.3% of the semi-span showed a thrust over weight ratio of 1.092 to climb axially at $4m/s$, whereas having the rotors at the original position at 29.7% of the semi-span required a thrust over weight ratio of 1.112.

During transition flight the limitations of the MRF model were brought to the surface and convergence difficulties were arisen due to the highly unsteady character of the flow. For this reason, the convergence criteria had to be relaxed and a simple qualitative evaluation of the flow was performed. A strong interaction between the VTOL and cruise components was observed, with the flow structures observed in horizontal and vertical flight being highly modified.

Even though it is of academic interest to have an accurate understanding of the flow behaviour during transition, unless the mission profile of the specific aircraft requires multiple conversions between axial and horizontal flight, that phase, corresponds only to a few seconds until the wing is capable of assuring the required lift, in missions that take at least an hour. Thus, it is not common practice to perform aerodynamic optimizations in transition flight.

5.2 Future Work

For future work there are some areas in which more in depth studies could be performed. During this thesis, the interaction between some of the UAV components was evaluated in the three main stages of the UAV flight, however more situations could be analysed which could yield important data, such as situations where crosswinds are present or when the UAV is flying at a different angle of attack. Moreover, the interaction of the VTOL structures with control surfaces was restricted to the tail, however, it would be interesting to assess on how the aileron and ruddervator deflections could influence the VTOL structures, and vice-versa, identify if said structures can affect the performance of the control surfaces and if that can create any safety concerns. Furthermore, trimmed simulations of the UAV could

be performed and the results compared with the conventional configuration to better understand how the VTOL structures influence the UAV's stability and control

As frequently mentioned throughout this thesis, multiple unsteady effects are present during the different flight phases, and, as such, further transient analyses of those effects can provide a more in-depth understanding of the flow. At the end of subsection 4.2.1 verified that the rotors, if left free during cruise flight, have a a net resulting torque around the axis of rotation which induces movement. The Six Degrees of Freedom Solver, available in ANSYS Fluent, could be used to model said rotation and obtain more accurate measures on drag during cruise flight, which can later be used to improve UAV efficiency. Similarly, during vertical flight phases, the Sliding Mesh or Overset Mesh can be implemented, using the results showed in this thesis as a baseline, to acquire a temporal load distribution throughout the UAV which could be used to identify possible unwanted aeroelastic effects due to the periodic loads.

Finally, a proper unsteady model such as the Sliding Mesh or the Overset Mesh can be applied to the transition flight stage to obtain an accurate reading on the flow behaviour and the loads during that phase, and identify if there are no major effects which can create safety concerns on the UAV.

Bibliography

[1] H. H. Heyson. Wind-tunnel testing of vtol and stol aircraft. *NASA Technical Memorandum 78750*, 50:1–79, 1978.

[2] F. F. Felker and J. S. Light. Aerodynamic interactions between a rotor and wing in hover. *Journal of the American Helicopter Society*, 33:53–61, 1988. ISSN 00028711. doi: 10.4050/jahs.33.53.

[3] M. A. McVeigh, W. K. Grauer, and D. J. Paisley. Rotor/airframe interactions on tiltrotor aircraft. *Journal of the American Helicopter Society*, 35:43–51, 1990. ISSN 00028711. doi: 10.4050/jahs.35.43.

[4] I. Fejtek and L. Roberts. Navier-stokes computation of wing/rotor interaction for a tilt rotor in hover. *AIAA Journal*, 30:2595–2603, 1992. ISSN 00011452. doi: 10.2514/3.11272.

[5] M. Smith, K. Ahuja, and A. Fleming. Computational and experimental simulations of tiltrotor configurations in hover. 1994. doi: 10.2514/6.1994-735.

[6] Y. S. Jung, J. Y. You, and O. J. Kwon. Numerical investigation of prop-rotor and tail-wing aerodynamic interference for a tilt-rotor uav configuration. *Journal of Mechanical Science and Technology*, 28:2609–2617, 2014. ISSN 1738494X. doi: 10.1007/s12206-014-0617-1.

[7] Y. Zhang, L. Ye, and S. Yang. Numerical study on flow fields and aerodynamics of tilt rotor aircraft in conversion mode based on embedded grid and actuator model. *Chinese Journal of Aeronautics*, 28:93–102, 2015. ISSN 10009361. doi: 10.1016/j.cja.2014.12.028. URL `http://dx.doi.org/10.1016/j.cja.2014.12.028`.

[8] G. Droandi, G. Gibertini, D. Grassi, G. Campanardi, and C. Liprino. Proprotor–wing aerodynamic interaction in the first stages of conversion from helicopter to aeroplane mode. *Aerospace Science and Technology*, 58:116–133, 2016. ISSN 12709638. doi: 10.1016/j.ast.2016.08.013. URL `http://dx.doi.org/10.1016/j.ast.2016.08.013`.

[9] L. Ye, Y. Zhang, S. Yang, X. Zhu, and J. Dong. Numerical simulation of aerodynamic interaction for a tilt rotor aircraft in helicopter mode. *Chinese Journal of Aeronautics*, 29:843–854, 2016. ISSN 10009361. doi: 10.1016/j.cja.2016.06.001. URL `http://dx.doi.org/10.1016/j.cja.2016.06.001`.

[10] D. Adair and M. Alimaganbetov. Propeller wing aerodynamic interference for small uavs during vstol 56th israel annual conference on aerospace sciences. pages 0–23, 2016.

[11] K. Chen, Z. Shi, S. Tong, Y. Dong, and J. Chen. Aerodynamic interference test of quad tilt rotor aircraft in wind tunnel. *Proceedings of the Institution of Mechanical Engineers, Part G: Journal of Aerospace Engineering*, 233:5553–5566, 2019. ISSN 20413025. doi: 10.1177/0954410019852827.

[12] H. Huang, G. He, L. Yu, and X. Wang. Numerical analysis on aerodynamic interference of a novel tilt-rotor uav in transition mode. pages 6043–6048, 2020. ISBN 9789881563903. doi: 10.23919/CCC50068.2020.9188992. URL http://search.ebscohost.com/login.aspx?direct=true&db=edseee&AN=edseee.9188992&site=eds-live.

[13] A. Bacchini and E. Cestino. Electric vtol configurations comparison. *Aerospace*, 6, 3 2019. ISSN 22264310. doi: 10.3390/aerospace6030026.

[14] *Ansys Fluent Theory Guide*, 2021. ANSYS Inc. Canonsburg, PA, USA.

[15] J. D. Anderson. *Fundamentals of Aerodynamics*. McGraw-Hill Education, 6th edition, 2017. ISBN 9781259129919.

[16] F. Moukalled, L. Mangani, and M. Darwish. *The Finite Volume Method in Computational Fluid Dynamics*, volume 113. Springer International Publishing, 2016. ISBN 978-3-319-16873-9. doi: 10.1007/978-3-319-16874-6. URL http://link.springer.com/10.1007/978-3-319-16874-6.

[17] H. L. R. Courant, K. Friedrichs. On the partial difference equations of mathematical physics. *IBM Journal of Research and Development*, 11:215–234, 4 (1967).

[18] D. C. Wilcox. Reassessment of the scale-determining equation for advanced turbulence models. *AIAA Journal*, 26(11):1299–1310, 1988. doi: 10.2514/3.10041.

[19] F. R. Menter. Two-equation eddy-viscosity turbulence models for engineering applications. *AIAA Journal*, 32:1598–1605, 1994. ISSN 00011452. doi: 10.2514/3.12149.

[20] B. Launder and D. Spalding. The numerical computation of turbulent flow computer methods. *Computer Methods in Applied Mechanics and Engineering*, 3:269–289, 03 1974. doi: 10.1016/0045-7825(74)90029-2.

[21] H. K. Versteeg and W. Malalasekera. *An Introduction to Computational Fluid Dynamics: The Finite Volume Method*. Pearson Education Limited, 2007. ISBN 9780131274983. doi: 10.1109/mcc.1998.736434.

[22] P. R. Spalart and S. R. Allmaras. One-equation turbulence model for aerodynamic flows. *Recherche aerospatiale*, pages 5–21, 1994. ISSN 00341223. doi: 10.2514/6.1992-439.

[23] *Ansys Fluent User's Guide*, 2021. ANSYS Inc. Canonsburg, PA, USA.

[24] *Ansys Meshing User's Guide*, 2021. ANSYS Inc. Canonsburg, PA, USA.

[25] *Discovery SpaceClaim*, 2021. ANSYS Inc. Canonsburg, PA, USA.

[26] *DesignModeler User's Guide*, 2021. ANSYS Inc. Canonsburg, PA, USA.

[27] M. Sosnowski. The influence of computational domain discretization on cfd results concerning aerodynamics of a vehicle. *Journal of Applied Mathematics and Computational Mechanics*, 17: 79–88, 2018. ISSN 22999965. doi: 10.17512/jamcm.2018.1.08.

[28] J. Leishman. *Principles of Helicopter Aerodynamics*. Cambridge Aerospace Series. Cambridge University Press, 2002. ISBN 9780521523967. URL https://books.google.pt/books?id=-PnV2JuLZi4C.

[29] Apc 18x8e performance data, 12 2014. URL https://www.apcprop.com/files/PER3_18x8E.dat. Available at https://www.apcprop.com/files/PER3_18x8E.dat.

[30] J. I. Milluzzo, A. Martinez, S. Drayton, and S. Davids. Experimental investigation of rotors hovering above inclined surfaces. *Journal of the American Helicopter Society*, 022005:1–12, 2020. ISSN 2161-6027. doi: 10.4050/jahs.66.022005.

[31] M. Sadraey. *Aircraft Design: A Systems Engineering Approach*. Aerospace Series. John Wiley and Sons, 2012. ISBN 9781118352809. URL https://books.google.pt/books?id=VT-Tc3Tx5aEC.

[32] Z. Sahwee, N. L. M. Kamal, S. A. Hamid, N. Norhashim, N. Lott, and M. H. M. Asri. Drag assessment of vertical lift propeller in forward flight for electric fixed-wing vtol unmanned aerial vehicle. volume 705, 2019. doi: 10.1088/1757-899X/705/1/012007.